AD NUMBER

AD816832

NEW LIMITATION CHANGE

TO

Approved for public release, distribution unlimited

FROM

Distribution authorized to U.S. Gov't. agencies and their contractors; Critical Technology; JUN 1967. Other requests shall be referred to Air Force Rocket Propulsion Lab., AFSC, Edwards AFB, CA.

AUTHORITY

AFRPL ltr, 27 Oct 1971

AFRPL-TR-67-129

HYPERGOLIC IGNITION AT REDUCED PRESSURES

T. F. Seamans
B. E. Dawson

Thiokol Chemical Corporation
Reaction Motors Division

TECHNICAL REPORT AFRPL-TR-67-129

June 1967

Air Force Rocket Propulsion Laboratory
Research and Technology Division
Air Force Systems Command
Edwards Air Force Base, California

SPECIAL NOTICES

Qualified users may obtain copies of this report from the Defense Documentation Center.

When U. S. Government drawings, specifications, or other data are used for any purpose other than a definitely related Government procurement operation, the Government thereby incurs no responsibility nor any obligation whatsoever, and the fact that the Government may have formulated, furnished, or in any way supplied the said drawings, specifications, or other data, is not to be regarded by implication or otherwise, or in any manner licensing the holder or any other person or corporation, or conveying any rights or permission to manufacture, use, or sell any patented invention that may in any way be related thereto.

AFRPL-TR-67-129

HYPERGOLIC IGNITION AT REDUCED PRESSURES

T. F. Seamans
B. E. Dawson

Submitted by: T. F. Seamans
Senior Research
Physicist

Approved by: W. G. Courtney
Supervisor,
Physics and Combustion
Laboratory

S. J. Tunkel
Section Head
Combustion Staff

D. J. Mann
Manager, Research &
Technical Staff

THIOKOL CHEMICAL CORPORATION
Reaction Motors Division
Denville, New Jersey
07834

FOREWORD

This is the Final Report covering work performed by Thiokol Chemical Corporation, Reaction Motors Division, Denville, New Jersey under Air Force Contract AF04(611)-11650. The internal report number is Report RMD-5809-F. The work was administered under the direction of Capt. William H. Summers, Rocket Propulsion Laboratory, Edwards Air Force Base, under Project No. 3148.

The research effort reported herein was conducted during the period 1 June 1966 to 30 November 1966 under RMD Project 5809. This work is an extension of previous work performed by Thiokol-RMD under Contract No. AF04(611)-9946 and reported in AFRPL-TR-65-257, dated February, 1966.

The principal investigator of the effort described herein is Mr. T. F. Seamans. Other contributors to the program are Dr. M. Vanpee and Messrs. G. A. Brown, B. E. Dawson, F. G. Hoffman, A. F. Lum and R. L. Storms. Dr. Vito D. Agosta, Professor of Aerospace Engineering, Polytechnic Institute of Brooklyn, served as a consultant principally for the heat transfer aspects of the vaporization model.

This technical report has been reviewed and is approved.

W. H. Ebelke, Colonel, USAF
Chief, Propellant Division

ABSTRACT

By experimental and theoretical means, a workable, fundamental model of hypergolic ignition in space-ambient engines has been developed by refining an earlier model in three important areas. The model applies to propellant combinations whose dominant ignition reactions are gas phase reactions, specifically N_2O_4/hydrazine-type fuels. The model is based on both physical kinetics of propellant droplet evaporation and overall kinetics of ignition reactions. The refinements made to the earlier model are: (a) incorporation of propellant flashing effects within the injector manifold volume following valve opening, (b) accounting for pre-ignition heat transfer between the thrust chamber walls and the vaporizing vapor/drop system, and (c) accounting for formation of a reaction intermediate by N_2O_4/MMH during the ignition delay period. For two different engine configurations, the resulting computerized model predicted pre-ignition chamber pressure histories and ignition delay times that agree well with experimental values. The N_2O_4/MMH reaction intermediate, which was found to be a mixture of at least four compounds the principal ones of which are MMH·H_2O and MMH·HNO_3, evolves heat upon its formation and consequently causes markedly shorter ignition delays than would otherwise occur. From thermochemical determinations, it appears that the reaction intermediate plays an important role in severe ignition pressure spiking and possibly oxidizer manifold explosions as well.

TABLE OF CONTENTS

TABLE OF CONTENTS (cont')

TABLE OF CONTENTS (cont')

LIST OF FIGURES

LIST OF FIGURES - cont'd

LIST OF FIGURES - cont'd

LIST OF FIGURES - cont'd

LIST OF TABLES

LIST OF TABLES - Cont'd

NOMENCLATURE

A	Frequency factor, cc/mole-sec for bimolecular reaction
A^*	Nozzle throat area, ft^2
A_c	Surface area of the thrust chamber, ft^2
c_1, c_2	Concentrations of reactants 1 and 2, mole/cc
c_p	Heat capacity, $Btu/lb_m\text{-}^oR$
C_p	Molar heat capacity, $Btu/lb\text{-}mole\text{-}^oR$
C_i	Constant, Eq. 3
D_{iw}	Idealized path length of propellant drop from injector orifice to chamber wall, ft.
E	Energy of activation, cal/mole
f	Wall heating factor, dimensionless
g_c	Dimensional factor, $32.2\ lb_m\text{-}ft/lb_f\text{-}sec^2$
G_{ij}	Mass evaporated from one drop in the i^{th} class of the j^{th} ensemble during one time interval, lb_m
G_N	Total mass evaporated from all drops in the system during one time interval, lb_m
G_w	Mass of vapor condensed on chamber walls during one time interval, lb_m
h	Heat transfer coefficient, $Btu/sec\text{-}ft^2\text{-}^oR$
k	Isentropic exponent
k_1, k_2	Rate constants for first and second order reactions, sec^{-1}, cc/mole-sec
K	Thermal conductivity, $Btu/sec\text{-}ft^2\text{-}(^oR/ft)$

L^*	Characteristic length, V_c/A^*, in
L_c	Idealized path length of propellant drop from injector orifice to chamber wall to nozzle throat, ft
m	Mass, gr, lb_m
m_c	Mass of vapor in the thrust chamber, lb_m
m_{noz}	Vapor mass efflux through the nozzle during one time interval, lb_m
M	Molecular weight, lb_m/lb-mole
N_i	Number of drops in i^{th} drop class
N_{FP}	Time interval in which the temperature of a drop reaches the freezing point
N_x	Time interval in which the drop becomes frozen solid
P_c	Chamber pressure, psia
P_g	Total pressure, $p_f + p_{ox}$, mmHg, PSF
$P_g(T_g)$	Gas pressure in the thrust chamber, PSF
$P_v(T_d)$	Propellant vapor pressure corresponding to the drop temperature, PSF
$P_v(T_w)$	Propellant vapor pressure corresponding to the wall temperature, PSF
P_r	Prandtl number, dimensionless
Q	Heat of reaction, cal/mole
Q_r	Heat evolved in one time interval due to formation of reaction intermediate, Btu
Q_N	Total energy reaching the surface of all drops in the system in one time interval, Btu
q_v	Rate of energy transfer to one drop, Btu/sec

r_{ij}	Radius of drops in i^{th} class of j^{th} ensemble, ft.
r_m	Mass-median drop size, micron
R	Universal gas constant, 1546 lb_f-ft/lb-mole ^oR, 1.987 cal/gr-mole ^oK
R_e	Reynolds number, dimensionless
t	Time, sec
t_{ss}	Time for propellant flow to reach nominal steady state level, sec
T	Temperature, ^oR, ^oK
t_{dh}	Time interval during which f goes from f_{max} to f_{min}, sec
V_c	Chamber volume, ft^3
V_d	Drop velocity (assumed constant and equal to liquid injection velocity), ft/sec
$\dot{w}$	Weight flow of propellant, lb/sec
W	Reaction velocity, mole/cc-sec
W_i	Mass of drops of i^{th} class injected in one time interval, lb_m
W_j	Mass of propellant injected in one time interval, lb_m
x_1, x_2	Mole fractions of reactants 1 and 2
X_{ij}	Fraction of a drop that is frozen, $0 \leq X_{ij} \leq 1$
Z, z	Heat transfer factors (Eq. 12), dimensionless
α	Accommodation coefficient
β	Ratio of partial pressures of oxidizer to fuel
ΔH_f	Heat of formation, kcal/mole
ΔH_r	Heat of reaction, kcal/mole, Btu/lb_m

Δt_N	Length of time interval, sec
Θ	Drop residence time expressed in number of time intervals, $= L_c/(V_d \Delta t_N)$
Θ_f, Θ_{ox}	Weight fraction of initial reactant in reaction intermediate
λ_e	Heat of vaporization, Btu/lb_m
λ_F	Heat of fusion, Btu/lb_m
λ_s	Heat of sublimation, Btu/lb_m
μ	Absolute viscosity, $lb_m/ft\text{-}sec$
ρ	Density, lb_m/ft^3, gr/cc
τ_{ig}	Calculated ignition delay time, msec

Subscripts:

d	drop
f	fuel
g	vapor
i	drop class, $1 \leq i \leq 3$
ign	ignition
int	reaction intermediate
j	drop ensemble consisting of three drop classes, $1 \leq j \leq N$
l	liquid
N	time interval
o	initial
ox	oxidizer
ss	steady state
w	wall

SECTION I

INTRODUCTION

A major problem of attitude control engines operating on nitrogen tetroxide and hydrazine-type fuels is the repeatability and reliability of the ignition of these hypergols. In high-response engines capable of very short minimum impulse bits, ignition pressure spikes occur at space conditions. The amplitude of these spikes can attain many thousands of pounds per square inch and cause structural failure of the thrust chamber. This is especially true for those chambers fabricated of a brittle material such as molybdenum.

Ignition pressure spikes can also trigger combustion instability which, if the pulse is of sufficient duration, can likewise cause structural failure due to excessive local heating. Even with short pulses, the impulse developed is different with unstable combustion. Consequently, impulse reproducibility is compromised, leading to potential control difficulties.

Another phenomenon occurring during the ignition interval concerns explosions within the oxidizer injector manifold which can also lead to failure of the hardware, especially the propellant valve. The genesis of the oxidizer injector explosions is believed to originate during tail-off of the previous pulse and involves propellant vaporization and condensation and possibly the formation and subsequent rapid reaction of a reaction intermediate within the manifold.

Hardware "fixes" and propellant additives to alleviate these ignition-related problems have been only partially effective (1-3). A need exists, therefore, for a more fundamental study of ignition of these propellants at reduced pressures in order to provide information from which to develop rational corrective and/or preventive measures.

This report covers a fundamental study performed by Thiokol Chemical Corporation, Reaction Motors Division, during a six-months program sponsored by Edwards-RPL under Contract AF04(611)-11630. The overall objective of the program is to refine and verify a fundamental, mathematical model of hypergolic ignition delay in space-ambient engines.

The initial development of the model, for N_2O_4/hydrazine-type fuels, was performed at Thiokol-RMD under Contract AF04(611)-9946, Part II. Reference 1 is the final report of the six months program. It was found that at low ambient pressures the dominant ignition reactions of N_2O_4/hydrazine-type fuels are gas phase reactions and strongly pressure dependent. It was necessary, therefore, for the model to include pre-ignition chamber pressurization due to propellant vaporization, as well as chemical kinetics of ignition reactions.

The resulting model consisted of two coupled sets of equations. In one set, the pre-ignition pressure-time history in a thrust chamber is determined taking into account:

a) propellant physical properties,
b) rate of propellant injection,
c) physical kinetics of propellant droplet evaporation and vapor condensation,
d) heat transfer between propellant vapor and drops,
e) drop residence time,
f) propellant vapor efflux through the nozzle, and
g) thrust chamber geometry.

In the other set, the chemical delay time as a function of pressure, temperature and vapor-phase composition is determined. The needed overall kinetic factors for the vapor-phase ignition reactions of these hypergols were experimentally determined during the earlier program.

Verification of the ignition delay model was precluded by two unexpected findings: appreciable pre-ignition heat transfer between injected propellants and thrust chamber walls, and formation of a reaction intermediate at sub-ignition pressures. Both of these affect the pre-ignition pressure rise in a thrust chamber and thereby the ignition delay time as well.

The objectives of the present program are to refine and then verify a computerized mathematical procedure for calculation of hypergolic propellant ignition delay in space ambient engines, including the effects of pre-ignition heat transfer and formation of a sub-ignition reaction intermediate. The program consists of three closely interrelated phases whose specific objectives are:

Phase I - Experimental evaluation of pre-ignition heat transfer between injected propellants and thrust chamber walls for N_2O_4/MMH and two thrust chamber configuration.

Phase II- Investigation of the effect of pre-ignition formation of the N_2O_4/MMH reaction intermediate on ignition delay and ignition pressure spikes including rate of formation, heat of formation, shock sensitivity and contribution to pre-ignition pressure transients.

Phase III- Refinement of the mathematical ignition delay model developed by previous AF04(611)-9946 contract efforts to include the effects of pre-ignition heat transfer and formation of a sub-ignition reaction intermediate. Verification of the refined model by calculating

ignition delays for N_2O_4/MMH in various different thrust chamber configurations and comparing the results with test values.

It has been necessary to expand the Phase I effort to include the effect on chamber pressurization of propellant "flashing" within the injector volume at valve opening. The short but finite times required for the propellant flows to reach nominal steady state levels slow the pre-ignition pressure rise in a thrust chamber and thereby affect ignition delay times.

The results of the theoretical and experimental program are discussed in the following sections.

SECTION II

SUMMARY

The overall objective of the program reported herein is to refine and verify a fundamental, mathematical model of hypergolic ignition delay in space-ambient engines. The model applies to propellant combinations whose dominant ignition reactions are gas phase reactions, specifically N_2O_4/hydrazine-type fuels. The model, which has been refined in three important areas in the present program, is based on both physical kinetics of propellant droplet evaporation and overall chemical kinetics of gas-phase ignition reactions.

This report is the final report of a six-month program which was performed in three interrelated phases. The purpose of Phase I was to experimentally evaluate pre-ignition heat transfer between thrust chamber walls and the vaporizing vapor/drop system in two thrust chamber configurations. The propellant combination of concern in this phase and throughout the program is N_2O_4/MMH. Phase I was expanded to include evaluation of propellant "flashing" effects within the injector volume following valve opening. Both the heat transfer and the initial propellant flashing within the injector volume affect pre-ignition pressure rise in a thrust chamber and thereby affect the ignition delay time as well.

Phase II was an investigation of a reaction intermediate formed by N_2O_4/MMH at sub-ignition conditions. The existence of the reaction intermediate had been established previously but it remained for the present program to determine its composition, properties, stability, heat of formation and rate of formation in order to incorporate formation of the material during an ignition delay period into the fundamental hypergolic ignition model.

The purpose of Phase III was to refine the mathematical ignition delay model developed by previous AF04(611)-9946 contract efforts to include pre-ignition heat transfer and formation of the sub-ignition reaction intermediate. Propellant flashing effects within the injector volume were included as well. The refined model was then to be verified by comparing calculated and experimentally measured engine ignition delays for various thrust chamber configurations.

Tests were conducted with five 50-lb thrust engines during the program at a simulated altitude of 185,000 ft. The ranges of chamber design parameters covered are: design chamber pressure, 20 to 200 psia; L*, 10 to 50 inches; and contraction ratio, 3.2 to 9.0. It was planned to use two injectors during the program: a one-on-one impinging stream doublet injector for hot firings and a self-impinging doublet injector for cold flow tests with each propellant individually. The purpose of the cold flow tests, in which chamber

pressurization due to propellant vaporization was measured, was to provide a basis against which to compare computed vaporization pressurization curves for each propellant. The self-impinging injector was used in order to obtain the effects of stream interaction on spray break-up for a singly flowed propellant. This injector maintains the same manifold volume and liquid injection velocity as one propellant side of the one-on-one doublet injector used for hot firings. The two injectors also have the same impingement angle and impingement length. Of necessity, however, the internal surface area of the self-impinging injector is larger and the propellant path is not as direct as would be desirable.

Despite the similarities between the injectors, chamber pressurization due to vaporization of each propellant singly flowed proceeded more slowly with the self-impinging injector as a consequence of its higher internal surface-to-volume ratio and the more tortuous propellant path. The one-on-one doublet injector was therefore used for subsequent cold flow tests and for all hot firings.

Experimental evidence of important pre-ignition reactions was obtained in two ways from the engine tests with the one-on-one doublet injector. In addition to chamber pressure histories which were measured in all engine tests, chamber wall temperature histories were measured in several of the cold flow and hot firing tests. With regard to the pressure measurements, it was found that the pre-ignition chamber pressure of a hot firing increases markedly more rapidly and to higher levels than the simple sum of the pressure histories of each reactant singly flowed. The chamber wall temperature histories, which were obtained with a flush mounted, high response, surface junction thermocouple, show that the walls cool in the case of singly flowed propellants whereas they heat up during the ignition delay times of hot firings.

The effects of propellant flashing within the injector volume on pre-ignition chamber pressurization were incorporated into the ignition delay model by empirically determining time-dependent coefficients of injected mass flowrate for each propellant. For the feed systems/propellant valves/injector assembly used during the program, a "best fit" was obtained with times from initial entry of propellant into the thrust chamber to attainment of full steady state flowrates of 1.6 and 0.8 msec for N_2O_4 and MMH, respectively. Using linearly increasing mass flowrates during these time intervals, good agreement between calculated and experimental chamber pressure histories during the flow build-up period was obtained for each propellant.

The predominant mechanism for pre-ignition heat transfer between thrust chamber walls and the vaporizing vapor/drop system was determined by analysis to be conductive heating of propellant droplets upon impingement with chamber walls. Other mechanisms considered were radiant heating

and convective heating of propellant vapor. The effects of conductive droplet heating were incorporated into the ignition delay model by empirically determining time-dependent coefficients for the time-varying temperatures of the drops of each propellant. The time dependent characteristic of the coefficients is required to account for the experimentally determined fact that chamber wall surfaces quickly cool during vaporization of each propellant. The wal. temperatures level-off, however, as the walls become coated with condensed phase propellant and, thus, the coefficients used to account for wall heating are held independent of time after being initially time-dependent.

In practice, three coefficients had to be empirically evaluated to account for wall heating. They are related to the maximum heating rate during a run, the minimum (steady state) rate, and the time during which the rate decreased from the maximum to the minimum. Conductive heating of each drop is permitted in the computer program only after the drop has had time to travel from the injector to the chamber wall. Values of the coefficients giving good agreement between calculated and experimental chamber pressure histories were determined for N_2O_4 and MMH in each of two engine configurations. It remained therefore to incorporate into the ignition delay model the formation of the N_2O_4/MMH reaction intermediate during the ignition delay period.

Reaction intermediates, or "residues", formed by N_2O_4/hydrazine-type fue' have bee.n observed under various conditions in several laboratories and during engine testing, particularly at simulated altitudes. Little was known about the material, and therefore, a number of analyses and determinations were made on the liquid reaction intermediate which forms from vapor N_2O_4/MMH at low pressure and room temperature.

The initial tests on the material were performed to determine its stability and sensitivity. The material was found to be less stable thermally and to impact than monomethyl hydrazine nitrate, $CH_3N_2H_3 \cdot HNO_3$, synthesized in the laboratory from MMH and HNO_3. The explosive strength of the N_2O_4/MMH reaction intermediate was found to be close to that of lead azide.

The density of the liquid material was determined at three temperatures. Its density at 25°C is 1.18 gr/cc. Vapor pressure measurements were attempted but these were unsuccessful due to the slow but significant decomposition of the material. Nevertheless, it could be ascertained from the reaction intermediate production runs, in a low pressure apparatus, that the vapor pressure of the material is less than 0.5 mmHg at room temperature.

Various chemical analyses were performed on several samples of the material. From the results of elemental analyses, an empirical formula for the reaction intermediate was computed to be $C_4H_{24}N_9O_6$. However the fresh material appears to be a mixture of at least four compounds, the principal ones being MMH· H_2O and MMH· HNO_3. The effect of the gradual decomposition, referred to above, is apparently to reduce the percentage of MMH· HNO_3 in the sample and to convert the monohydrate of MMH to the dihydrate, MMH· $2H_2O$. Also CO_2 is produced and it is believed to exist in the degraded samples as $CH_3N_2H_2COON_2H_4CH_3$.

The heat of formation of fresh reaction intermediate was determined from measurements of the heat of combustion of the material with oxygen. The heat of formation for the liquid material was found to be -0.509 kcal/gr, using the empirical formula given above. Then, for an overall stoichiometry given by:

$$3NO_2(g) + 4CH_3N_2H_3(g) \longrightarrow C_4H_{24}N_9O_6(l) + N_2(g)$$

the heat of this reaction for formation of the reaction intermediate during an ignition delay period is calculated to be ΔH_r = -66.2 kcal/mole of MMH. This value is only 21% of the total heat of complete combustion on a fuel basis.

To determine the rate of formation of the reaction intermediate, a low pressure flow tube apparatus was used in which the reactant vapors were greatly diluted with nitrogen. The temperature profile along the tube axis was measured by fine wire Pt-10% Rh/Pt thermocouples positioned at known distances from the mixing point of the reactants. The overall order of reaction for formation of vapor phase reaction intermediate was found to be approximately two from tests at elevated (75°C) initial temperature and various total pressures (30 to 60 mmHg). In the room temperature tests, condensation of the reaction intermediate occurred and thus activation energy for formation of reaction intermediate could not be extracted from the effect of initial temperature on temperature rise along the flow tube. The activation energy must be low, however, because the reaction proceeds, and proceeds rapidly, at room temperature. Further, the activation energy must be less than that of the ignition reactions since the material forms at conditions under which ignition does not occur (in the flow tube, for instance).

Formation of the reaction intermediate during an ignition delay period was incorporated into the ignition delay model by adding a heat source and a vapor mass sink. The heat source accounts for the heat evolved as the material forms and the vapor mass sink accounts for consumption of vapor phase reactants as the condensed phase reaction intermediate is produced.

In the calculations for ignition delay in an engine, an activation energy of 4.5 kcal/mole was used for the formation reaction of the reaction intermediate. Since the activation energy for ignition of these propellants is 5.2 kcal/mole (determined in a previous program), the selected value of 4.5 kcal/mole for the activation energy for formation of the reaction intermediate is reasonable.

Ignition was determined analytically by summing over successive 50 microsecond time intervals of the solution the fractional degree of ignition computed for each time interval. The fractional degree of ignition for each time interval is the ratio of the length of the time interval (50 microseconds) to the ignition delay time calculated for the conditions of pressure, temperature and composition of the reactant vapors prevailing at that time. The analytical expression used to calculate the ignition delay time for each time interval (derived in a previous program) is:

$$(\tau_{ig})_N = \frac{R^2 T_{g_{av}}^{\ 3}}{P_g E_{ign} (AQ)_{ign}} \left(1 + \frac{1}{\beta}\right)\left(C_{p_f} + \beta C_{p_{ox}}\right) \exp\left(\frac{E_{ign}}{R T_{g_{av}}}\right)$$

where $P_g = p_f + p_{ox}$ and $\beta = \frac{p_{ox}}{p_f}$. p_{ox}, p_f and $T_{g_{av}}$ are obtained for each time interval from the pre-ignition chamber pressurization analysis which also takes into account formation of the reaction intermediate. The fractional degrees of ignition are summed over successive time intervals until the fraction becomes unity, indicating ignition. The ignition delay time in an engine is that time in the computer solution at which the fraction becomes unity.

A series of calculations was made in which A_{int}, the frequency factor for formation of reaction intermediate, was varied in order to obtain for one engine configuration (design chamber pressure of 200 psia) the best fit between (1) calculated and experimental pre-ignition chamber pressure-time histories and (2) calculated and experimental ignition delay times. A very good fit was obtained for $A_{int} = 1.7 \times 10^{11}$ cal. cc/mole^2-sec. This value was then used in a computer run for a second engine configuration (design chamber pressure of 75 psia) with the result that, again, a good fit was obtained. For each engine configuration, the calculated and experimental ignition delay times agreed to within 1%.

The calculations indicate that the reaction intermediate plays an important role in ignition of these hypergols. Although formation of the reaction intermediate removes mass from the vapor phase and thereby tends to retard pre-ignition chamber pressurization, the heat which is evolved more than compensates for the vapor mass removal and finally results in markedly shorter ignition delay times. A further consequence of the evolved heat, however, is that the reactant temperatures are substantially raised during the ignition delay period to levels at which, first, condensation of the reaction intermediate will no longer occur, second, the composition of subsequently formed reaction intermediate will

likely differ from the composition of material formed earlier in the ignition delay period, and third, the material will undergo decomposition or possibly reaction with additional oxidizer. Thus, although considerable insight has been obtained into the many events occurring during an ignition delay time, further study of the latter part of the ignition delay period is needed.

The computed results predict that many of the smaller N_2O_4 drops cool evaporatively to a point at which MMH vapor will tend to condense upon them. This previously unanticipated phenomenon raises a question as to what chemical reaction will occur at the oxidizer liquid/fuel vapor interface. The reverse situation was found not to apply, i. e. fuel drops do not cool sufficiently to cause condensation of oxidizer vapor upon them.

From the thermochemical determinations performed on the reaction intermediate, it is found that the reaction between the condensed phase material and additional oxidizer is very energetic and is a likely contributor to severe ignition spikes. The calculations of ignition delay in an engine indicate that sufficient oxidizer exists in the vapor state at ignition to react with all of the computed amount of reaction intermediate formed during the delay period. Therefore, for an increased understanding of severe ignition pressure spikes, it is necessary to determine the energy release rate of the reaction between oxidizer and the reaction intermediate.

The present hypergolic ignition delay model, though not complete in every detail, is nevertheless suitable for developing design information pertaining to ignition phenomena. For example, the effects of propellant leads/lags and various transient flow increase schemes for each propellant from time zero can be analytically evaluated as to their effect on ignition delay time and the amount of reaction intermediate formed. This information can assist engine development programs by economically defining specific development objectives.

SECTION III

PHASE I - PHYSICAL KINETICS ASPECTS OF PRE-IGNITION CHAMBER PRESSURIZATION

The hypergolic ignition delay model developed previously under Contract AF04(611)-9946 is based on both physical kinetics of droplet evaporation and chemical kinetics of ignition reactions. The resulting model consists of two coupled sets of equations (1). In one set, the pre-ignition pressure-time history in the chamber is calculated taking into account the physical properties of the propellants, the rate of propellant injection, propellant evaporation and condensation, heat transfer between vapor and droplets, droplet residence time, rocket engine chamber geometry, and propellant vapor efflux through the nozzle. In the other set, the chemical delay time as a function of pressure, temperature and vapor-phase composition is determined. In this section of the report, we are concerned with the first-mentioned set which deals with chamber pressurization.

It was found from the initial model development effort that the vaporizing vapor/drop system is non-adiabatic (i.e., significant heat transfer with thrust chamber walls occurs), and that a short but finite time is required, following flow initiation, for the propellants to attain their nominal steady-state flowrates. Both phenomena affect pre-ignition chamber pressurization and thereby the ignition delay time as well.

In this section of the report, the experimental and analytical work performed to incorporate these phenomena into the mathematical model is described. In the following sub-sections, the equations describing pre-ignition chamber pressurization due to propellant vaporization are reviewed (from Ref. 1); then the experimental program which includes both cold flow and hot firing tests is discussed. Finally in this section, the analytical results to include injector flashing and wall heating effects in the model are given.

A. THEORY - CHAMBER PRESSURIZATION DUE TO PROPELLANT VAPORIZATION

The injected propellant spray is represented mathematically by a three-drop-size spray model. The three drop sizes are obtained by applying a logarithmiconormal distribution (with a specific geometric standard deviation depending on the type of injector) to a given mass median drop size and then selecting three radii such that 30% of the injected weight flow is in drops of the smallest radius, 40% in the intermediate size drops, and 30% in the largest drops (4). Thus there are three classes of drops, $1 \leq i \leq 3$. The number of drops in each class is obtained from

$$N_i = \frac{3\ Wi}{4\pi\ r_i^3 \rho_l} \qquad \text{where } W_1 = 0.3\ W_j,\ W_2 = 0.4\ W_j,\ W_3 = 0.3\ W_j \tag{1}$$

and $W_j = \dot{w} \Delta t_N$, the mass of propellant enjected during one time interval.

Pressurization of a thrust chamber is treated mathematically as a sequence of steady state processes in very short time intervals. At the start of each time interval, a new three-class ensemble of drops enters the thrust chamber. These undergo evaporation during the time interval as do the drop ensembles which entered previously. At any time, each class of drops has a unique radius, temperature and fraction of an individual drop that is frozen.

Each drop is identified by i, j and N numbers which indicate respectively the class to which the drop belongs, the time interval in which the drop entered the thrust chamber, and the time interval in question. Thus the possible values of i, j and N are: $1 \leq i \leq 3$, $1 \leq j \leq N$, and $N = 1, 2. \ . \ .$

Based on the kinetic theory of gases, the mass evaporated from a single drop in one time interval is given by (5);

$$G_{ij} = [\, P_v(T_{dij})_{N-1} - P_g(T_g)_{N-1} \,] \alpha (r_{ij})^2_{N-1}\ \Delta t_N \sqrt{\frac{8\pi M g_c}{R(T_{dij})_{N-1}}} \tag{2}$$

where $P_v(T_{dij})_{N-1}$ is the vapor pressure corresponding to the temperature of the i^{th} size drop of the j^{th} ensemble at the end of the previous time interval.

The assumptions involved are:

1. The number of molecules leaving the liquid surface per unit time (when the ambient pressure is below the liquid vapor pressure) is the same as the number which impinge on the same surface when the liquid is in equilibrium with its vapor.

2. The gas evaporates at the same temperature as the liquid drop from which it evolves.

3. The molecular weight of the vapor and liquid is the same.

4. Ideal gas law.

The total mass evaporated during one time interval depends in part on the total surface area of all the drops in the system. The total surface area depends in turn on the number and radius of the drops in each class.

Multiplying Eq. 2 by N_i, the number of drops in each class as given by Eq. 1, and then summing over the i's and j's, one obtains for the total mass evaporated during one time interval:

$$G_N = \sum_{j=1}^{N} \sum_{i=1}^{3} G_{ij} N_i = \sum_{j=1}^{N} \sum_{i=1}^{3} [P_v(T_{dij})_{N-1} - P_g(T_g)_{N-1}] \frac{3C_i a W_j \Delta t_N}{\rho_l (r_{ij})_{N-1}} \sqrt{\frac{Mg_c}{2\pi R(T_{dij})_{N-1}}} \quad (3)$$

where $C_1 = 0.3$, $C_2 = 0.4$ and $C_3 = 0.3$ The density of the liquid, ρ_ℓ, is assumed constant.

Condensation onto chamber walls can occur if the gas pressure exceeds the propellant vapor pressure evaluated for the wall temperature. The mass of vapors condensing on chamber walls in one time interval is given by:

$$G_w = [P_g(T_g)_{N-1} - P_v(T_w)] a A_c \Delta t_N \sqrt{\frac{Mg_c}{2\pi R(T_g)_{N-1}}} \quad (4)$$

but with the constraint $0 \leq G_w < \infty$.

The mass efflux through the nozzle during one time interval for constant k for the gas is given by

$$m_{noz} = (Pg)_{N-1} A^* \Delta t_N \sqrt{\frac{kMg_c}{R(Tg)_{N-1}} \left(\frac{2}{k+1}\right)^{\frac{k+1}{k-1}}} \quad (5)$$

The mass of vapor in the chamber at the end of the N^{th} time interval is obtained from the perfect gas law.

$$(m_c)_N = \frac{V_c M}{R} \left[\frac{P_g}{T_g}\right]_N \quad (6)$$

The temperature of the gas in the chamber at the end of the N^{th} time interval is obtained by taking a mass weighted average of the temperature, which includes the temperature of the gas generated due to evaporation during the time interval plus the temperature of the gas left from the previous time interval minus the temperature of the gas which condenses on the chamber walls and that which passes through the nozzle. For a single specie system and a constant vapor heat capacity,

$$T_{gN} = \frac{\sum_{j=1}^{N} \sum_{i=1}^{3} G_{ij}(T_{dij})_{N-1} + (T_g)_{N-1}[(m_c)_{N-1} - (G_W)_N - (m_{noz})_N] - \frac{Q_N}{c_{pg}}}{\sum_{j=1}^{N} \sum_{i=1}^{3} G_{ij} + (m_c)_{N-1} - (G_W)_N - (m_{noz})_N} \quad (7)$$

where Q_N is the total heat transferred from the vapors to all the drops in the system during one time interval. Q_N is derived subsequently.

A mass balance of the system yields the gas pressure in the chamber at the end of the N^{th} time interval.

$$G_N-(G_W)_N-(m_{noz})_N=(m_c)_N-(m_c)_{N-1} \tag{8}$$

The terms on the left hand side are given by Eqs. 3, 4, and 5 while the right hand side is Eq. 6 evaluated at the end of the N and N-1 time intervals.

The gas pressure in the chamber at the end of the N^{th} time interval is therefore:

$$P_{gN}=T_{gN}\left(\left[\frac{P_g}{T_g}\right]_{N-1}+\frac{R}{V_c M}\left[\sum_{j=1}^{N}\sum_{i=1}^{3}G_{ij})_N-(G_W)_N-(m_{noz})_N\right]\right) \tag{9}$$

where T_{gN} is evaluated from Eq. 7.

New drop radii and drop temperatures must be calculated at the end of every time interval to account for the effect of evaporation during the time interval on the size and temperature of each drop. A new radius for each drop is obtained from a mass balance on the drop together with Eq. 2, giving:

$$(r_{ij})_N=(r_{ij})_{N-1}\left[1-\frac{3[P_v(T_{dij})_{N-1}-P_g(T_g)_{N-1}]\,a\,\Delta t_N}{\rho_l (r_{ij})_{N-1}}\sqrt{\frac{Mg_c}{2\pi R(T_{dij})_{N-1}}}\right]^{1/3} \tag{10}$$

The new drop temperature is obtained from an energy balance on the drop, including the effect of heat transfer from the vapors to each drop. The energy reaching the surface of a drop from the gas during one time interval is, according to (4):

$$q_{V_{ij}}\Delta t_N=4\pi h(r_{ij})^2_{N-1}Z\Delta t_N[(T_g)_{N-1}-(T_{dij})_{N-1}] \tag{11}$$

where

$$Z=\frac{z}{e^z-1}\,,\quad z=\frac{G_{ij}\,c_{pg}}{4\pi h\Delta t_N (r_{ij})^2_{N-1}} \tag{12}$$

$$h=\frac{K_g}{2(r_{ij})_{N-1}}[2+0.6\,Pr^{1/3}Re^{1/2}],\quad Pr=\left[\frac{c_p\mu}{K}\right]_g \tag{13}$$

and $$Re = \frac{2(r_{ij})_{N-1} \; V_d \; M(P_g)_{N-1}}{\mu_g \, R(T_g)_{N-1}} \tag{14}$$

G_{ij} in Eq. 12 is given by Eq. 2. Equation 14 omits drag effects.

An energy balance on the drop is then

$$G_{ij}\lambda_e = \frac{4}{3} \pi (r_{ij})^3_N \rho_l \, c_{pl} \left[(T_{dij})_{N-1} - (T_{dij})_N \right] + q_{v_{ij}} \Delta t_N \tag{15}$$

from which the new drop temperature at the end of the time interval is

$$(T_{dij})_N = (T_{dij})_{N-1} - \frac{3[P_v(T_{dij})_{N-1} - P_g(T_g)_{N-1}] \, a \, (r_{ij})^2_{N-1} \, \lambda_e \Delta t_N}{\rho_l \, c_{pl} \, (r_{ij})^3_N} \sqrt{\frac{Mg_c}{2\pi R (T_{dij})_{N-1}}} + \Phi \tag{16}$$

where $$\Phi = \frac{3h \left[(T_g)_{N-1} - (T_{dij})_{N-1} \right] (r_{ij})^2_{N-1} \, Z \, \Delta t_N}{\rho_l \, c_{pl} \, (r_{ij})^3_N} \tag{17}$$

The temperature within the drop is assumed to be uniform. The heat of vaporization, λ_e, the heat capacity of the liquid, c_{pl}, and the liquid density, ρ_l, are assumed constant. Values of these quantities corresponding to the mid-temperature of the range encountered are used.

A drop being cooled by evaporation can arrive at its freezing point. Once T_{dij} equals T_{FP}, then T_{dij} remains constant as the drop freezes. The fraction of the drop that freezes in one time interval due to evaporation and including vapor-droplet heat transfer effects is given by

$$G_{ij}\lambda_s = X_{ijN} \frac{4}{3} \pi \rho_l (r_{ij})^3_N \lambda_F + q_{v_{ij}} \Delta t_N \tag{18}$$

The solid fraction of the drop, or its "quality" X_{ij}, increases in successive intervals until the drop is frozen solid. X_{ij} is given by

$$X_{ij} = \sum_{N=N_{FP}}^{N_x} \left[\frac{3G_{ij} \, \lambda_s}{4\pi \rho_l (r_{ij})^3_N \lambda_F} - \frac{c_{pl}}{\lambda_F} \Phi \right] \tag{19}$$

with the constraint that $0 \leq X_{ij} \leq 1$. G_{ij} and Φ are given by Eqs. 2 and 17 respectively. The summation over successive time intervals for the drop in question begins when the temperature of the drop, T_{dij}, reaches T_{FP}. The summation ends when the drop is completely frozen, i.e. $X_{ij} = 1$.

Once the drop is frozen solid, further evaporation (sublimation) causes the temperature of the drop to decrease. Equation 16, modified to reflect the solid state of the droplet, becomes applicable again.

The total energy reaching the surface of all drops in the system in one time interval, i.e. Q_N of Eq. 7 is:

$$Q_N = \sum_{j=1}^{N} \sum_{i=1}^{3} q_{v_{ij}} \Delta t_N N_i = \sum_{j=1}^{N} \sum_{i=1}^{3} 4\pi h (r_{ij})^2_{N-1} Z N_i \Delta t_N [(T_g)_{N-1} - (T_{dij})_{N-1}] \quad (20)$$

where N_i, the total number of drops in each class, is given by Eq. 1 and h and Z are given by Eqs. 13 and 12, respectively.

The above equations together with the vapor pressure equation for the propellant under consideration have been programmed for an IBM 360 Model 50 computer. The length of the time intervals Δt_N, used in calculations ranges from 20 to 50 microseconds depending on the particular propellant and motor geometry under consideration.

Typical gas pressure and temperature histories calculated by the above equations are given in Fig. 1 for N_2O_4 and MMH in a specific engine configuration (Configuration #1). The calculation assumes a step function increase in flow rate at time zero and an adiabatic vapor/drop system.

In the computer program, the active lifetime of each drop is limited. The drop residence time used is defined simply as the time required for a drop, moving at a constant velocity equal to the liquid injection velocity, to travel from the injector orifice to a point on the chamber wall and then to the nozzle throat. The point on the chamber wall is obtained from the direction of the injected propellant stream and the radius of the chamber. Computer runs in which drop residence times were varied by a factor of two showed that this factor is unimportant for an adiabatic vapor/drop system. The reason for this is that once a drop has been in the system for one residence time period, its temperature is such that its vapor pressure is close to the gas pressure prevailing at that time. In accordance with Eq. 6, the amount of evaporation (or condensation) from that time onward is small.

Also, in the computer program, a drop is made inactive before one residence time period lapses if it freezes solid, i.e. $X_{ij} = 1$. It is assumed that due to the low conductivity of the solid, an excessive temperature gradient exists in a solid drop which markedly reduces the evaporation rate at the surface of the drop.

B. EXPERIMENTAL PROGRAM - THRUST CHAMBER TESTS

1. Test Apparatus and Instrumentation

a. Experimental Facilities

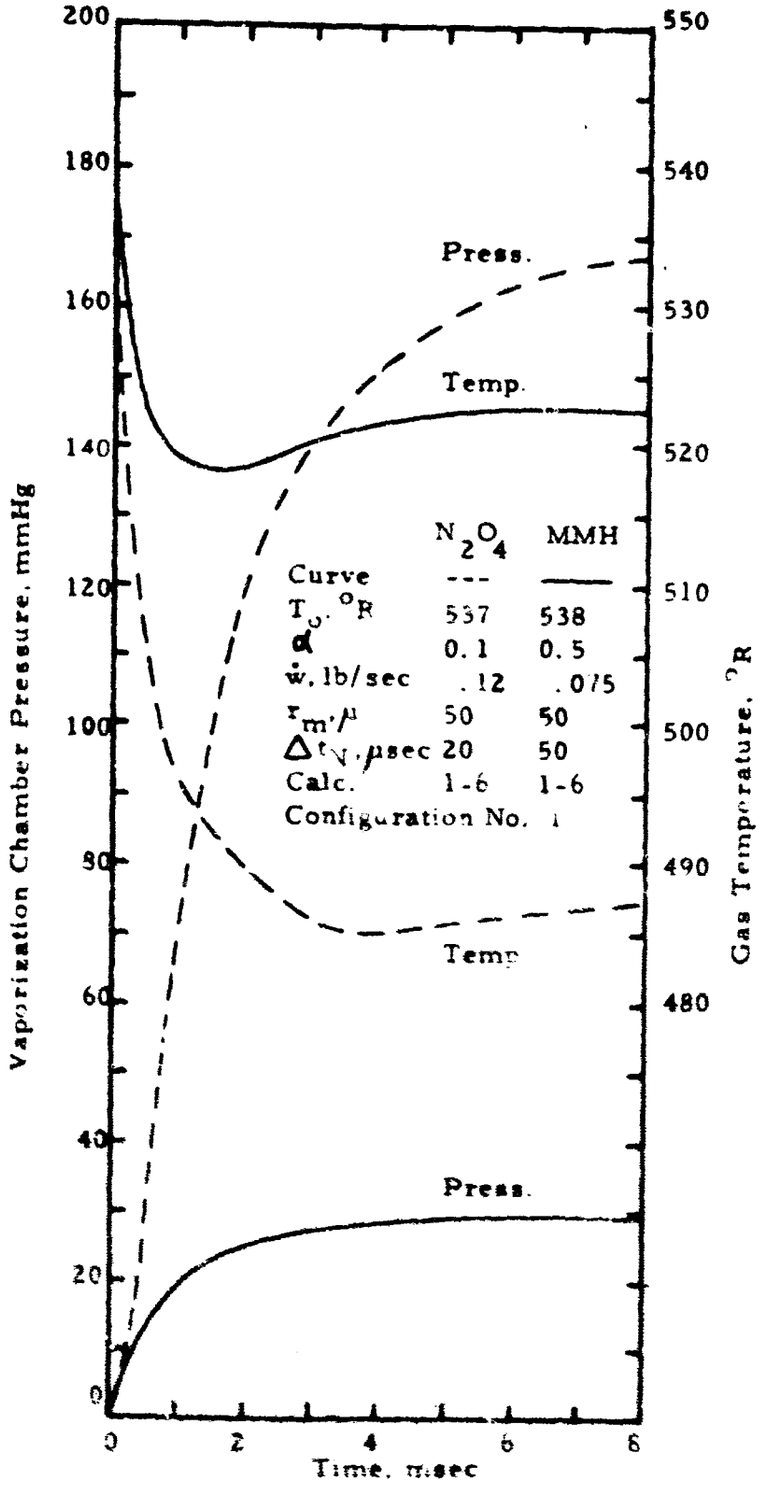

Figure 1. Calculated Vaporization Pressure and Temperature Histories Without Reaction for an Adiabatic Vapor/Drop System and a Flowrate Step-Function at Time Zero.

All thrust chamber tests were performed in a large stainless steel vacuum tank to minimize the increase in ambient pressure due to propellant vaporization or combustion. The vacuum tank, which is shown in Fig. 2, is 7 ft in diameter and 25 ft long, providing a volume of approximately 1000 ft^3. The tank has four 8 in. diameter ports along each side for instrumentation and observation purposes.

The pumping system consists of a Kinney KD 780 pump having a 625 cfm pumping capacity at a pressure of 1 mmHg and a Roots 6000 blower which has a pumping capacity of 3250 cfm at a pressure of 10^{-1} mmHg. All thrust chamber tests were conducted at an ambient pressure of 0.3 mmHg and were less than 120 msec duration, so the ambient pressure was essentially constant for the entire test period. Schlieren movies of the flow issuing from an injector were taken at a higher pressure, 5 mmHg, to permit better definition of the initial gas propellant flow which is difficult to detect at the lower ambient pressures.

The oxidizer and fuel propellant systems consisted of a 300 cc stainless steel tank, Jamesbury safety valve, Fox propellant solenoid valve, and associated hand valves and tubing as shown in Fig. 3. Each set was mounted on a separate plate which contained provisions for all necessary external connections such as pressurization and vent systems. The propellant valves and chamber were mounted under the plates with the injector facing downward as shown in Fig. 4. Also visible in this photograph are the actuators for the Jamesbury safety valves which are mounted out of view on the top of the plates.

b. Experimental Hardware

The 50 lb thrust, attitude control thrust chamber consisted of an injector-valve assembly, a chamber flange, a transparent chamber section, and a stainless steel nozzle. An exploded view of a thrust chamber assembly is shown in Fig. 5, although the particular chamber length shown in the photograph was not tested in the present program. The Kistler water-cooled adapters shown in this picture were replaced with the uncooled adapters shown in Fig. 4. The diaphragms of the flush-mounted transducers were protected with RTV silicone rubber. For short run times (several hundred milliseconds), the coating eliminates thermal effects on the transducers from either cold propellants or hot combustion gases which would otherwise lead to erroneous pressure signals.

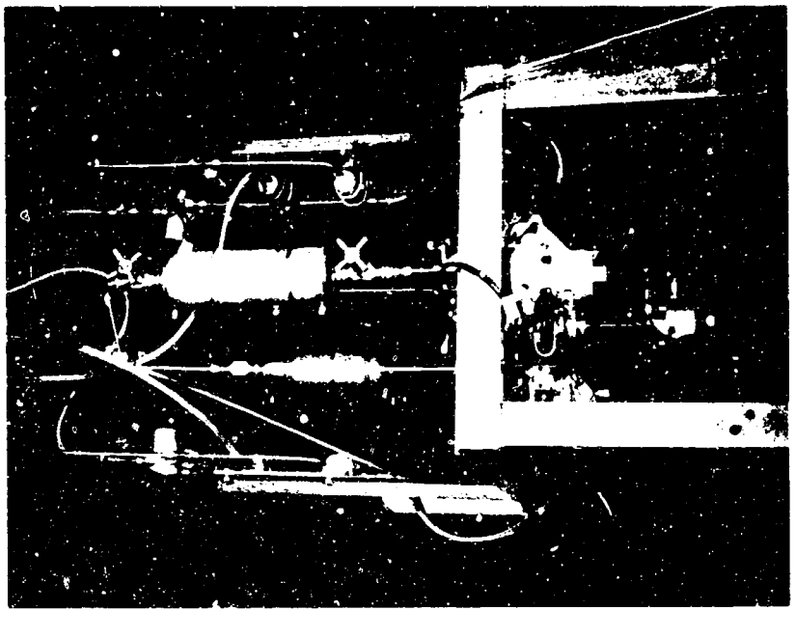

(5809-3)

Figure 3. Propellant Systems and Thrust Chamber Configuration No. 5.

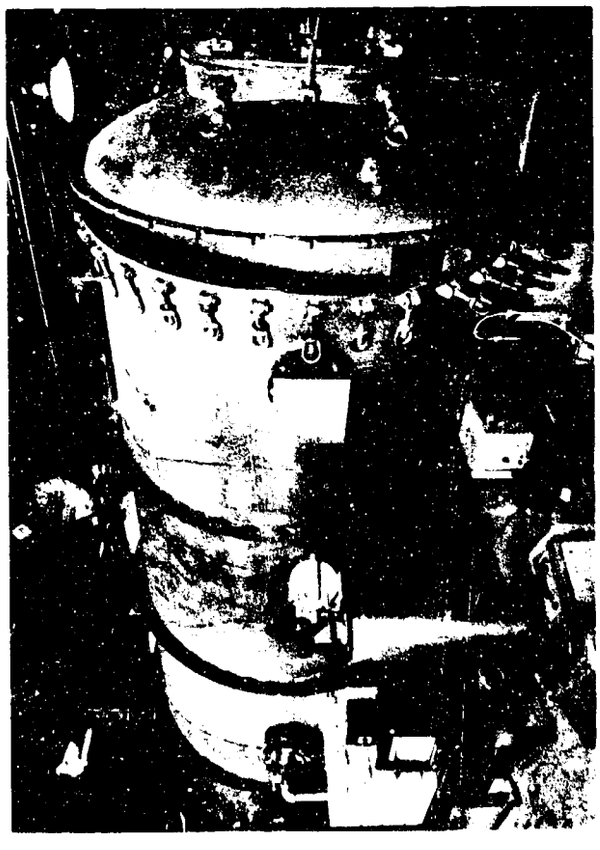

(5809-4)

Figure 2. Altitude Simulation Tank

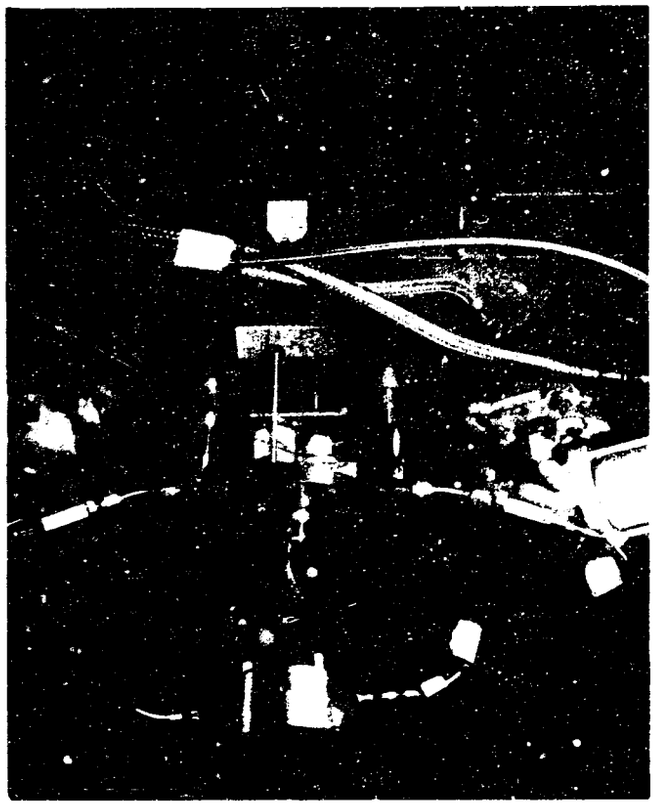

(5809-1)

Figure 4. Thrust Chamber, Propellant Valves and Instrumentation

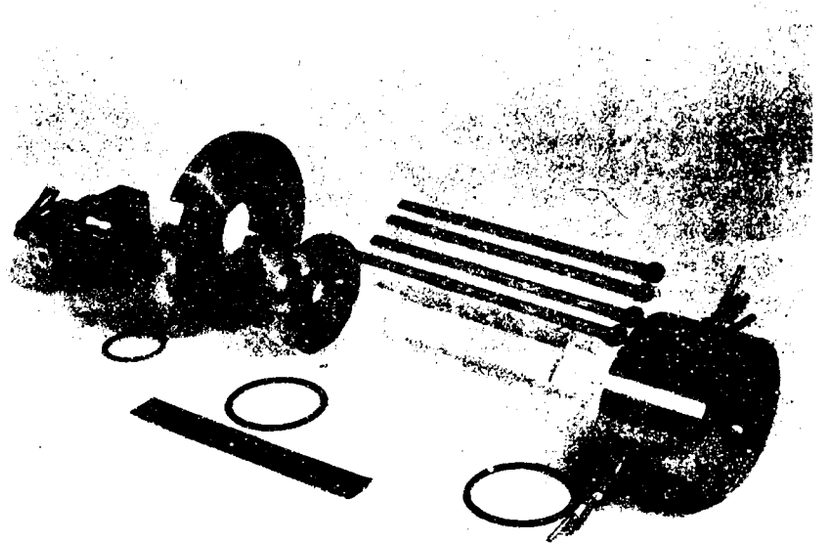

(5801-12)

Figure 5. Exploded View of Transparent Thrust Chamber

Five chamber and nozzle configurations were chosen from the 27 possible combinations available from the previous programs under Contract AF04(611)-9946. The design parameters for the five selected configurations are detailed in Table I. The transparent chamber sections were fabricated from commercially available sizes of acrylic tubing cut to the desired length.

TABLE I

THRUST CHAMBER CONFIGURATIONS

Configuration No.	1	2	3	4	5
Design P_c, psia	200	75	20	200	200
Chamber I. D., in.	1.25	1.875	3.50	0.75	1.25
Contraction Ratio	9.00	7.90	7.68	3.22	9.00
L*, in.	10.3	10.8	13.0	10.0	50.0
Chamber Length, in. (a)	0.25	0.25	0.25	2.21	4.69
Nozzle Throat Area, sq. in.	0.137	0.351	1.253	0.137	0.137

(a) Length of transparent section only.

Each stainless steel nozzle section includes a 3/4 inch long cylindrical portion whose internal diameter is the same as the inside of the respective transparent chamber section. Kistler pressure transducers were flush mounted in the cylindrical portion of the nozzle sections. The volume of this section, as well as that of the convergent portion of the nozzle, was included in the L* calculations for sizing the transparent sections.

The entire chamber assembly was held together with 1/4 inch threaded rods which were insulated from the metal nozzle to keep the Kistler transducers ungrounded. Buna-N O-rings sealed the flanges and the transparent chamber sections.

The propellant solenoid valves are 1/4 in. venturi valves manufactured by the Fox Valve Development Co., Inc. These stainless steel valves have a pintle with a Teflon poppet which provides a seal in the entrance of the venturi section. The propellant volume in the valve downstream of the seat is quite small. The valves were mounted directly to the back face of the injector to minimize dribble volumes. A high voltage pulse circuit was used to reduce the valve opening

time to about 1 msec.

Two injectors were used during the program: a one-on-one doublet injector and a self-impinging doublet injector. Originally, the one-on-one doublet injector was to be used for hot firings whereas the self-impinging injector was to be used for obtaining chamber pressurization data for vaporization of singly flowed propellants. This data would be the basis against which computed chamber pressurization histories (without chemical reaction) would be compared. The reason for using a self-impinging injector for singly flowed propellants was to duplicate the effects of stream interaction on break-up and atomization of the injected propellants in hot firings.

Section views of the two injectors are shown in Fig. 6, with the propellant valves outlined. The throats of the venturi valves are approximately in line with the rear face of the injector. The single-element doublet injector consists of two #53 (0.0595 in. dia.) drill holes impinging at a 90° angle 0.14 inches from the injector face. The self-impinging injector was designed to duplicate one propellant side of the single-element doublet injector, but provide stream interaction effects on spray break-up. Therefore the impingement length, impingement angle, injector dribble volume (0.0021 cu. in. downstream of venturi hole), and liquid propellant injection velocity (69.0 and 71.5 ft/sec for N_2O_4 and MMH, respectively) are identical in both injectors. The internal surface area is unavoidably larger in the self-impinging injector and the propellant path is not as direct as would be desirable. The effect of these differences is discussed in Section III. B. 2.

c. Instrumentation

In addition to conventional instrumentation required for propellant pressurization and system monitoring, special instrumentation was employed to determine ignition delays and monitor pressure transients during the ignition delay period. This instrumentation included high speed schlieren movies of the propellant impingement zone, photomultiplier tube to detect ignition, and high response pressure transducers and recording equipment.

The purpose of the schlieren system was to investigate propellant stream characteristics prior to ignition. Although the schlieren instrumentation could not be used to detect propellant entry during the actual thrust chamber tests because of the poor optical properties of the plastic chambers, it was

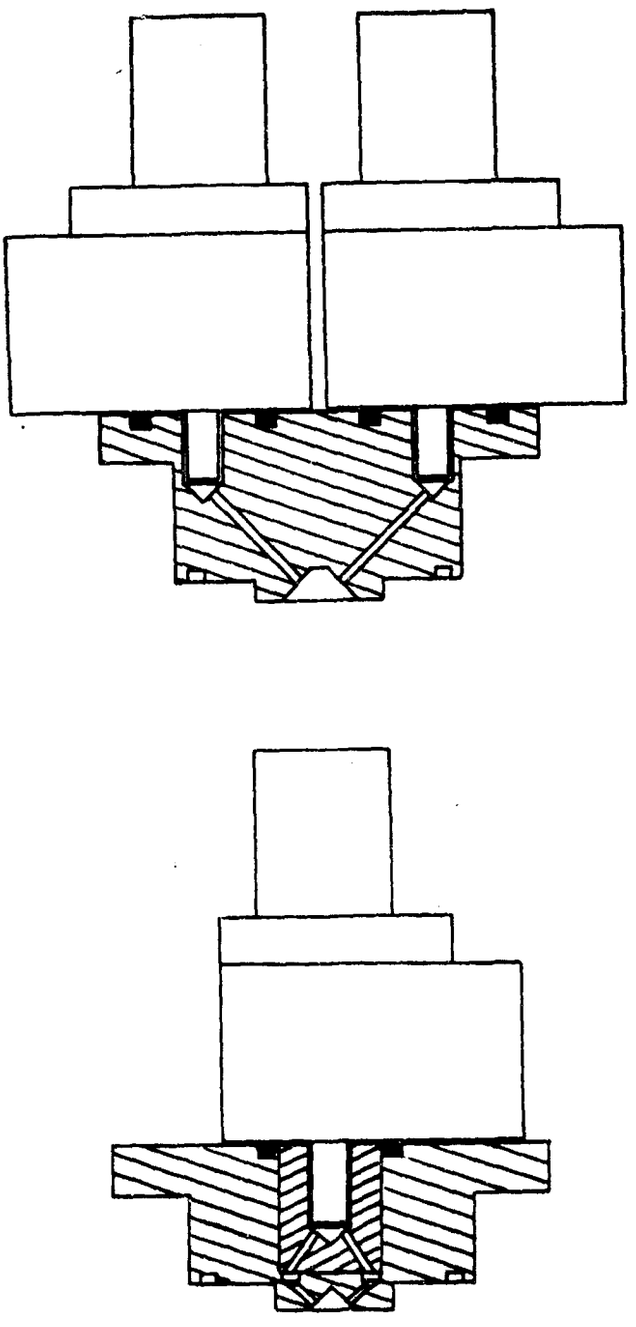

Figure 6. Section Views of One-on-One Doublet Injector (top) and Self-Impinging Doublet Injector (bottom).

used to study the injection characteristics of both injectors without a chamber installed. Times could be determined from valve signal to vapor entry, liquid entry, and steady-state liquid flow.

A two-mirror, parallel-beam schlieren system was used with a Fastax high-speed camera to obtain suitable time resolution. The essential components of the system included a Unertl Model BH 6 Normal and Color Schlieren Source, a pair of eight-inch front-surface parabolic mirrors of 64-inch focal length, knife-edge, and the Fastax camera capable of approximately 16,000 pictures per second using split-frame optics. Time resolution when the valve opened was approximately 7 frames (14 pictures) per msec as determined by a 1000 Hz timing light. The Fastax camera and knife edge are visible in Fig. 2.

A flame detector consisting of an RCA 1P28 photomultiplier tube was used to determine the time at which ignition occurred. The tube is sensitive to wavelengths from about 2200Å to 6000Å but no filter was required since the tank was not illuminated for the thrust chamber tests. It could sense ignition through the plastic chambers. A short-duration, single-flash strobe light was also detected by the photomultiplier tube, as well as by the camera, for a time reference to correlate the various instrumentation.

Chamber pressure was measured by Model 701A and 603A Kistler pressure transducers and Model 566 Kistler charge amplifiers. The two transducers were mounted in the same plane at the nozzle end of the thrust chamber as shown in Fig. 4. The 701A transducer with a rise time of 6 microseconds and high sensitivity was used to detect chamber pressure rise due to propellant entry and vaporization prior to ignition. The 603A transducer, with less sensitivity but with a resonant frequency over 400,000 Hz and a rise time of 1 microsecond, was used for the pressure transients at and after ignition. Two additional 603A transducers in the propellant lines upstream of the Fox propellant valves (Fig. 4) measured the feed line pressure transients when the valves opened.

Propellant temperatures were monitored at the propellant valves using metal sheathed copper-constantan thermocouples. A bare bead thermocouple on the back face of the injector was used to measure initial hardware temperature. All temperatures were recorded prior to a run on a single Brown strip chart recorder using a selector switch.

The transient data were recorded on a Tektronix Type 555 Dual-Beam Oscilloscope with type CA amplifiers to permit simultaneous display of four parameters. The four parameters selected differed for the cold flow tests and the ignition tests. For cold flow of one propellant, the parameters were the 701A chamber pressure transducer, the 603A valve inlet pressure transducer for the respective propellant, valve current, and also the photomultiplier tube signal when the schlieren movies were taken. For ignition tests, the 701A chamber pressure transducer was used to measure pressure rise prior to ignition due to both propellants vaporizing and reacting, the 603A chamber pressure transducer was used for ignition spikes and transients, the photomultiplier tube for ignition detection, and the combined valve currents for valve operation. Oscilloscope sweep rates varied from 1 to 20 msec/cm depending on the test information desired.

2. Experimental Results

Experimental chamber pressure-time curves for vaporization of singly-flowed propellants in thrust chambers of various configurations were measured to serve as the basis against which to compare the computed vaporization pressurization curves. Two injectors were used in the tests: a self-impinging doublet injector and a single element one-on-one doublet injector.

a. Self-impinging Injector vs. 1-on-1 Doublet Injector.

The self-impinging injector was used in order to obtain the effects of stream interaction on spray break-up for a singly-flowed propellant. Although the self-impinging injector maintains the same manifold volume, impingement angle, liquid injection velocity and impingement length as the single element doublet injector, vaporization chamber pressure rise times were markedly different for the two injectors, as shown in Fig. 7. The figure gives typical oscillograms of tests with each propellant singly flowed through each injector in two different engine configurations. In each oscillogram, the middle curve at

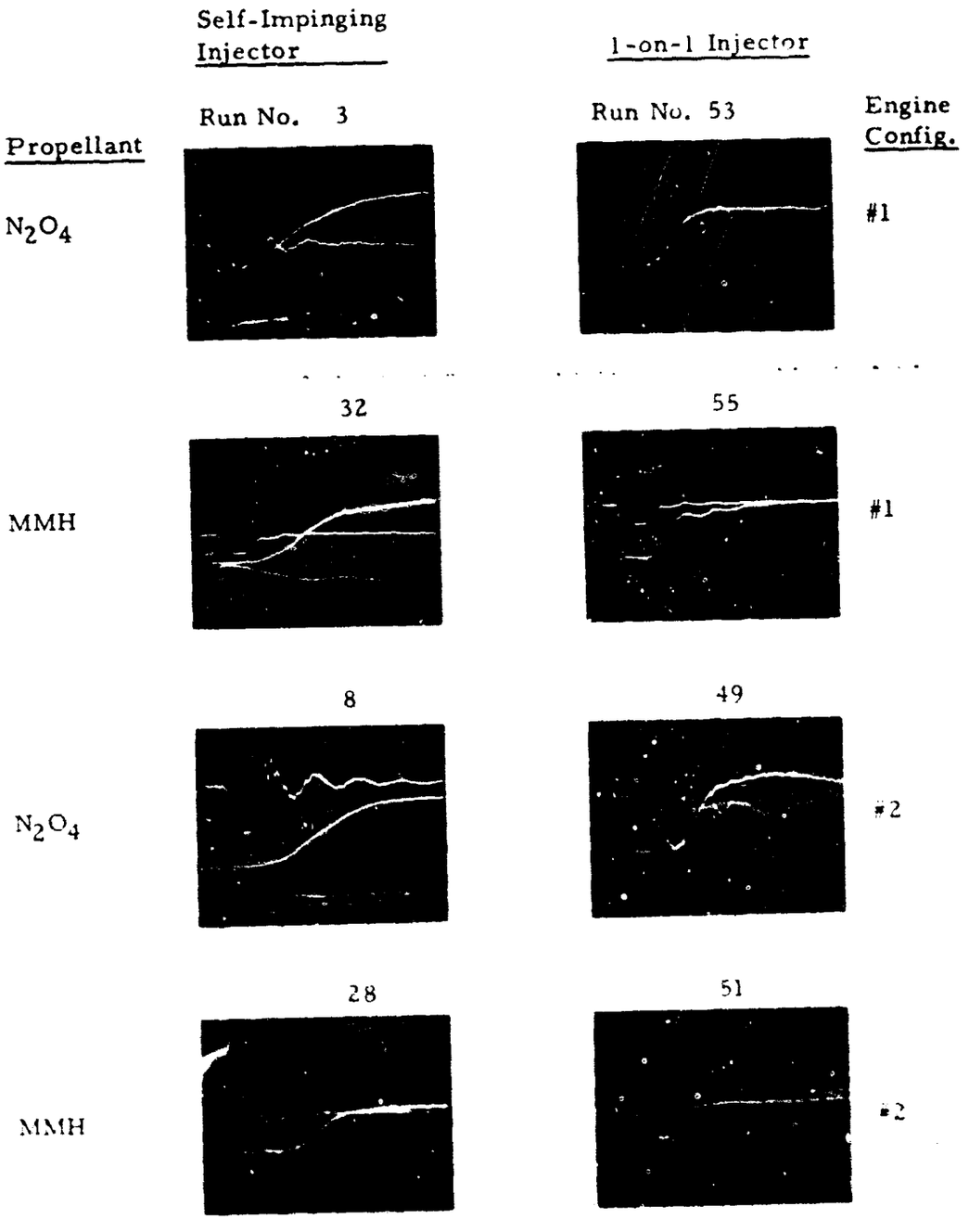

Figure 7. Oscillograms of Singly Flowed N_2O_4 and MMH Through Two Injectors in Each of Two Engine Configurations

the left side (start of trace) is the chamber pressure as measured by a Kistler 701A transducer. The upper curve gives propellant valve inlet pressure (Kistler 603A transducers) and the lower curve is propellant valve current. Deflection of the latter is downward in the case of N_2O_4 and upward in the case of MMH. Pertinent data and scale factors for the eight oscillograms are given in Table II.

With both engines and with both propellants, chamber pressure rise times are seen to be significantly slower with the self-impinging injector. The four chamber pressurization curves for Engine Configuration No. 2 are plotted on a common scale in Fig. 8. The longer rise times of the self-impinging injector are pronounced.

The transient flow characteristics of each injector with each propellant singly flowed were determined from high speed schlieren movies (approx. 14,000 pictures per second). Because of the poor optical quality of the acrylic thrust chamber sections, the schlieren movies were taken without chambers or nozzles attached to the injectors. A summary of the results is given in Table III which gives the average times from valve signal to emergence of vapor, vapor/liquid mixture, all liquid, and steady state liquid flow. The transition from vapor flow to vapor/liquid mixture flow is sudden and is "caught" in a single picture of the movie. By contrast, the transitions to all liquid flow and to steady state liquid flow are gradual. Consequently the times from valve signal to these latter transitions are subject to an error of perhaps one millesecond. Nevertheless, it is clear that steady state liquid flow is achieved more quickly with the one-on-one doublet injector. Although the manifold volumes are the same for each propellant in the two injectors, the more tortuous path in the self-impinging injector (Fig. 6) and its higher internal surface-to-volume ratio (which tends to increase propellant flashing) retard attainment of steady state liquid flow. The reduced mass throughput during the flow build-up period with the self-impinging injector causes a slower pressure rise in a thrust chamber and would lead to a longer ignition delay time. Thus, the self-impinging injector flow did not properly simulate the hot firing flow of one propellant through the one-on-one injector. The latter injector, then, was used subsequently for both cold flow tests of singly flowed propellants and for hot firings as well.

TABLE II

PERTINENT DATA AND SCALE FACTORS FOR OSCILLOGRAMS OF FIGURE 7

RUN NO.	3	53	32	55	8	49	28	51
Propellant	N_2O_4	N_2O_4	MMH	MMH	N_2O_4	N_2O_4	MMH	MMH
Engine Configuration No.	1	1	1	1	2	2	2	2
Injector	Self	1-on-1	Self	1-on-1	Self	1-on-1	Self	1-on-1
Propellant and Hardware Temperature, $^{o}F \pm 1^{o}$	80	79	76	80	74	78	76	78
Scale Factors:								
Valve Inlet Pressure (503A), psi/cm	83	83	71	71	83	83	71	71
Chamber Pressure (701A), mmHg/cm	103	103	20.6	20.6	51.5	51.5	20.6	20.6

Parameters Common to All Runs of Figure 7 :

Initial Ambient Pressure	=	0.3 mmHg
Propellant Tank Pressure - N_2O_4	=	740 psig
Propellant Tank Pressure - MMH	=	710 psig
Steady State N_2O_4 Flowrate	=	0.120 lb_m/sec
Steady State MMH Flowrate	=	0.075 lb_m/sec
Oscillogram Time Base	=	2 msec/cm or 20 msec total time

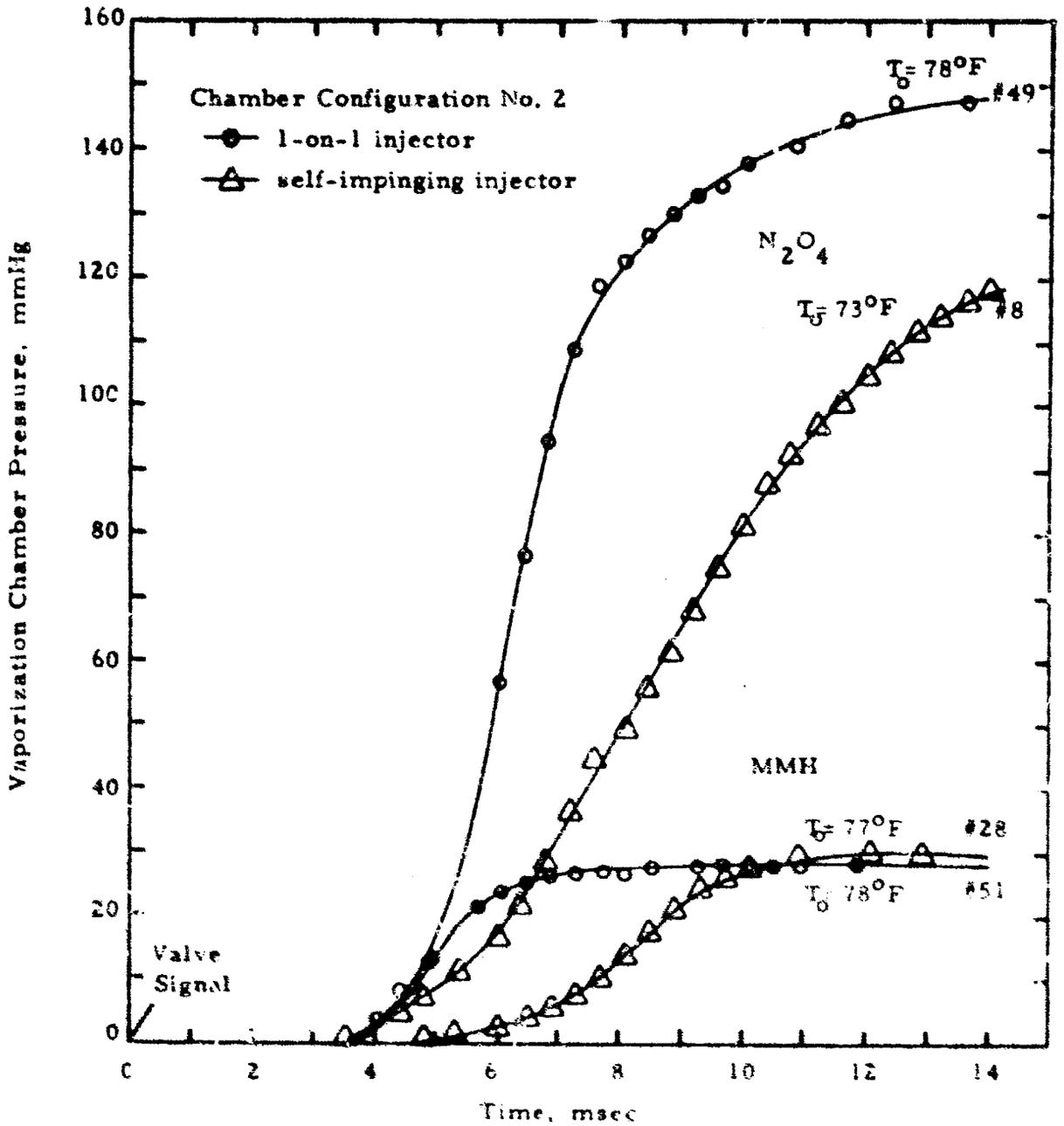

Figure 8. Experimental Chamber Pressure Histories for Singly Flowed Propellants Through Two Injectors.

TABLE III

SUMMARY OF SCHLIEREN CHARACTERIZATION OF INJECTORS

Propellant	Injector	Time from Valve signal to:* Vapor msec	Vapor/ Liquid msec	All Liquid msec	St. St. Liquid** msec	Run Nos.
N_2O_4	1-on-1	-	4.6	6.1	7.3	44, 44a, 45
	self impinging	1.8	4.2	7.0	11.5	11-14, 16
MMH	1-on-1	3.6	3.9	-	7.6	46, 47
	self impinging	2.0	4.5	6.7	12.0	17-19

*Valve opening times ± 0.8 msec for each valve based on valve current traces.

**St. St. = Steady State.

b. Cold Flow and Hot Firing Pre-Ignition Chamber Pressurization

Experimental chamber pressure-time curves were measured for each propellant singly flowed using the one-on-one doublet injector and all five engine configurations (Table I). Similar curves for hot firings in the five engines were also obtained. Figures 9 and 10 give typical oscillograms for each propellant singly flowed and for a hot firing in each of the five engine configurations. Corresponding oscillograms in each figure differ only in the time base, Fig. 9 having the faster sweep rates.

For all cold flow tests in the two figures, the upper curve at the left side (start of trace) of each oscillogram is valve inlet pressure (Kistler 603A transducer). The middle curve gives the chamber pressure rise (Kistler 701A transducer) due to vaporization of the propellant. The lower curve is valve current.

For the hot firings, the two upper curves are chamber pressure. The first of these two to rise is the signal from the 701A transducer. When ignition occurs, this trace goes off scale and is not seen thereafter. The second of the two upper curves is the signal from a 603A transducer also flush mounted in the thrust chamber. The gain for this transducer is reduced so that chamber pressure during combustion is recorded. The lower two traces in the hot firings are photo-

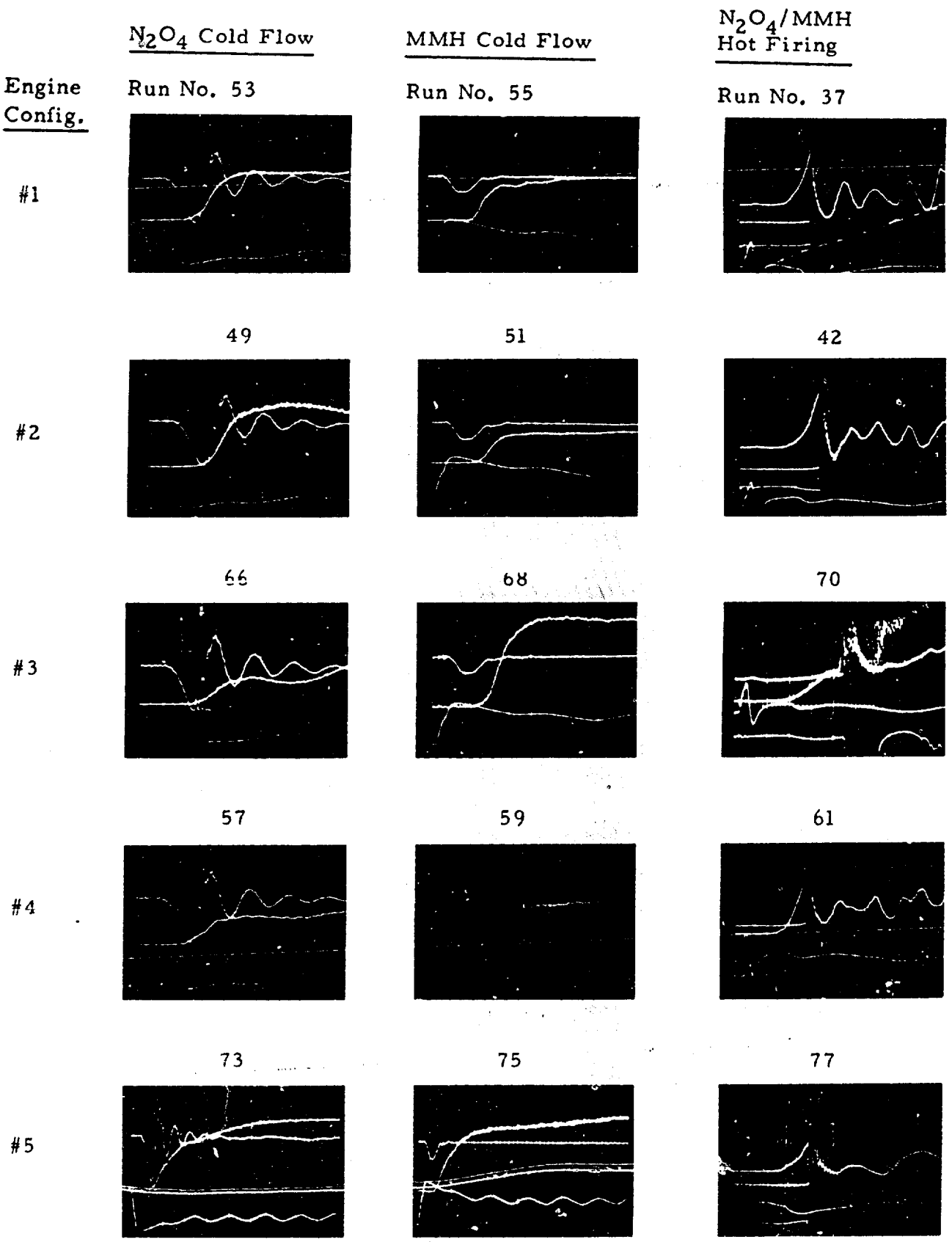

Time Base = 5 msec/cm for Runs 73 and 75
= 2 msec/cm for All Other Runs

Figure 9. Oscillograms (Faster Sweep) of Cold Flow and Hot Firings in Five Engine Configurations

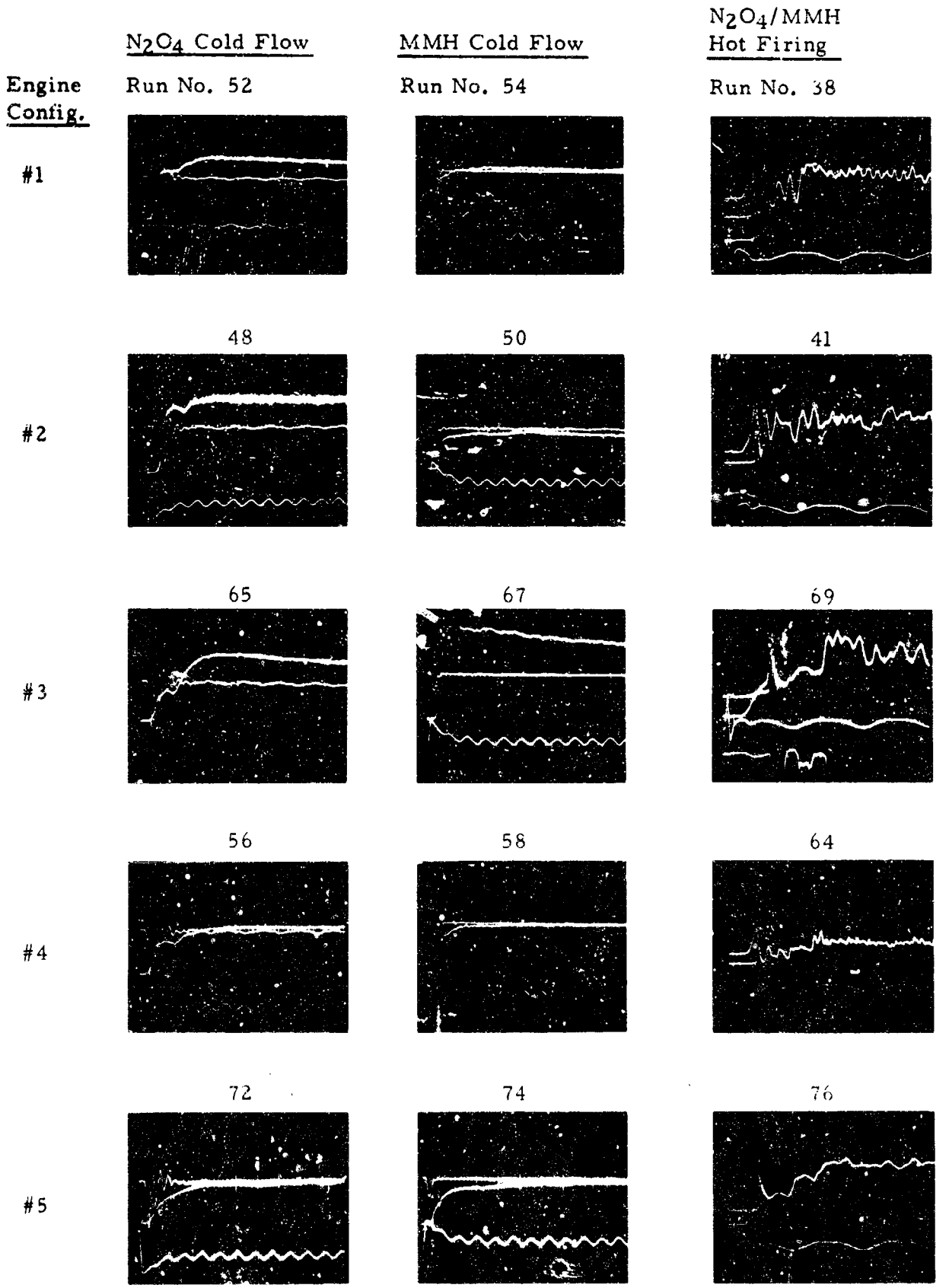

Figure 10. Oscillograms (Slower Sweep) of Cold Flow and Hot Firings in Five Engine Configurations

multiplier signal and a combined valve current signal. The latter is the one that remains on-scale throughout the runs. When the photomultiplier receives light from ignition or combustion, the signal deflects off-scale downward. Pertinent data and scale factors for the oscillograms of the figures are given in Table IV.

Ignition delays and pressure in the chambers at ignition were obtained for the five engine configurations from these hot firing oscillograms and those of repeated runs. The results are summarized in Table V. As noted in the table, the ignition delays are times from valve signal to ignition. The valve current traces in the cold flow runs indicate a valve opening time of less than one millisecond. Because the pressure in the chamber just prior to ignition is rising rapidly generally, the pressure at ignition is difficult to specify with good precision (for example, see Run No. 61 in Fig. 9). In a few cases, the pressures at ignition as determined from repeated runs varied by as much as 20%.

The two cold flow chamber pressurization curves and the hot firing pre-ignition chamber pressurization curve for Engine Configurations 1 and 2 are plotted on common scales in Figs. 11 and 12 respectively. In each figure, the dashed curve is simply the sum of the cold flow chamber pressurization curves for each reactant. A comparison of these sum-of-partial-pressures curves and their respective hot firing pre-ignition curves shows good agreement for the first millisecond of the rising pressures. A gradual divergence then begins, the hot firing pre-ignition curves rising more steeply than the sum-of-partial-pressures curves. For both engine configurations, the slopes of the two hot-firing pre-ignition curves increase with time until ignition occurs, which causes a discontinuity in the curves (Figs. 9 and 10). The divergence, which reaches 100-130 mmHg at ignition, indicates appreciable pre-ignition reactions. The divergence and its cause are the subjects of Section IV of this report. In the present section, we are concerned with analytically predicting the cold flow chamber pressurization curves of each propellant singly flowed.

TABLE IV
PERTINENT DATA AND SCALE FACTORS FOR
OSCILLOGRAMS OF FIGURES 9 AND 10

Run No.	Propellant	Propellant and Hardware Temp. °F ± 2°	Scale Factors P_c-701A mmHg/cm	P_c-603A psi/cm	Sweep Rate msec/cm
37	NTO/MMH	77	103	75.5	2
38	NTO/MMH	77	103	75.5	5
41	NTO/MMH	77	103	30.2	5
42	NTO/MMH	77	103	30.2	2
48	NTO	78	51.5	-	10
49	MMH	78	51.5	-	2
50	MMH	78	20.6	-	10
51	MMH	78	20.6	-	2
52	NTO	79	103	-	10
53	NTO	79	103	-	2
54	MMH	80	20.6	-	10
55	MMH	80	20.6	-	2
56	NTO	80	103	-	10
57	NTO	80	103	-	2
58	MMH	81	20.6	-	10
59	MMH	81	20.6	-	2
61	NTO/MMH	81	103	75.5	2
64	NTO/MMH	81	206	151	5
65	NTO	82	20.6	-	10
66	NTO	82	20.6	-	2
67	MMH	83	5.2	-	10
68	MMH	83	5.2	-	2
69	NTO/MMH	83	51.5	7.6	5
70	NTO/MMH	83	51.5	7.6	2
72	NTO	72	103	-	10
73	NTO	73	51.5	-	5
74	MMH	74	20.6	-	10
75	MMH	74	10.3	-	5
76	NTO/MMH	74	103	75.5	5
77	NTO/MMH	74	103	75.5	2

TABLE IV - cont'd
PERTINENT DATA AND SCALE FACTORS FOR
OSCILLOGRAMS OF FIGURES 9 AND 10

Parameters Common to All Runs of Figures 9 and 10 :

Initial Ambient Pressure	=	0.3 mmHg
Propellant Tank Pressure - N_2O_4	=	740 psig
Propellant Tank Pressure - MMH	=	710 psig
Steady State N_2O_4 Flowrate	=	0.120 lb_m/sec
Steady State MMH Flowrate	=	0.075 lb_m/sec
Injector: 1-on-1 doublet		
Scale Factors:		
Valve Inlet Pressure - Ox	=	83 psi/cm
Valve Inlet Pressure - Fuel	=	71 psi/cm

TABLE V

SUMMARY OF EXPERIMENTAL IGNITION DELAYS
AND CHAMBER PRESSURES AT IGNITION

ENGINE CONFIGURATION NO.	AVERAGE IGNITION DELAY* msec	APPROX. AVERAGE CHAMBER PRESSURE AT IGNITION mmHg
1	5.7 ± 0.2	260
2	6.6 ± 0.2	230
3	9.4 ± 0.4	70
4	6.0 ± 0.2	330
5	6.7 ± 0.2	130

* Valve signal to ignition.

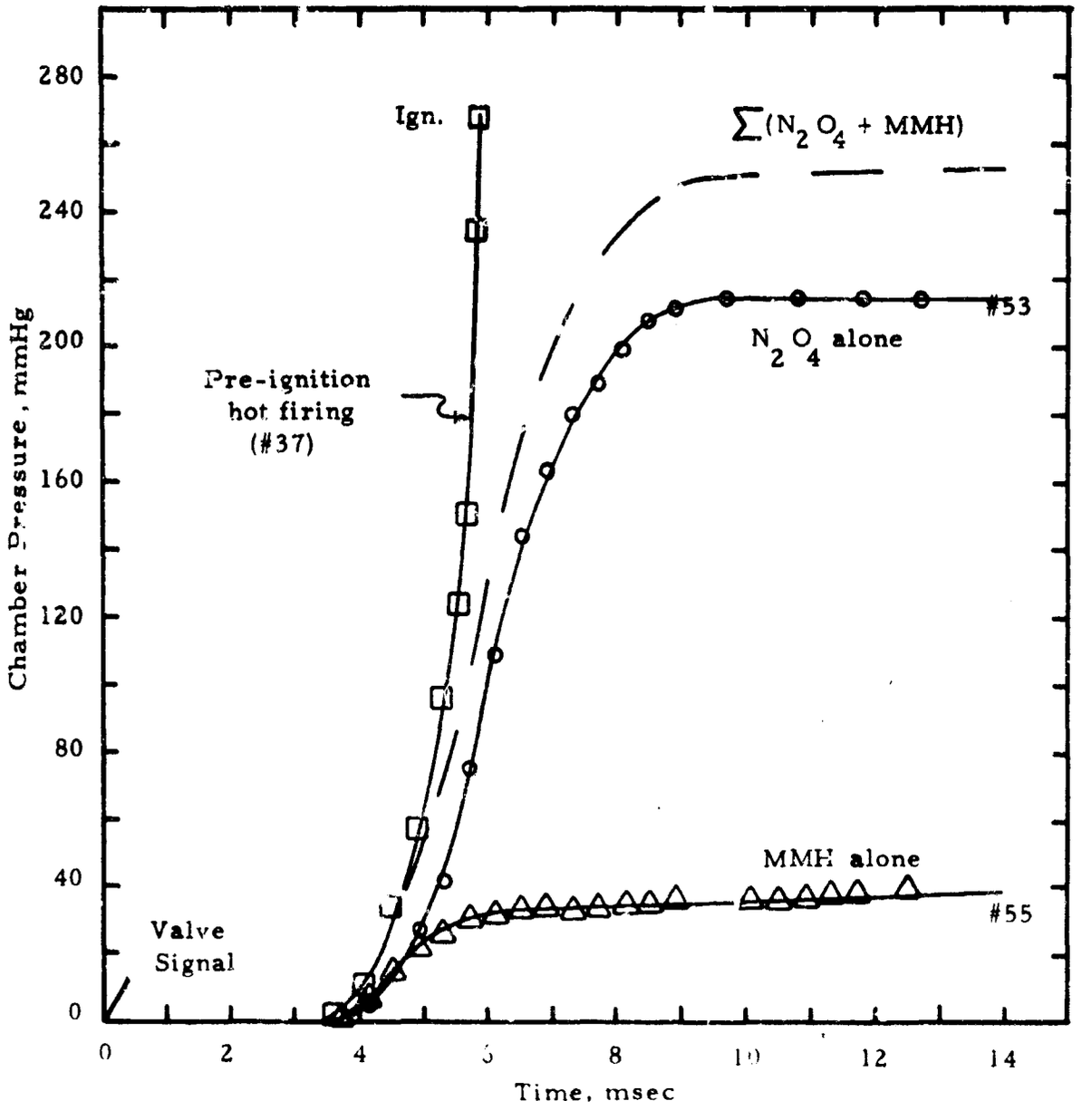

Figure 11. Experimental Chamber Pressurization Curves for Cold Flow and Hot Firing - Engine Configuration No. 1.

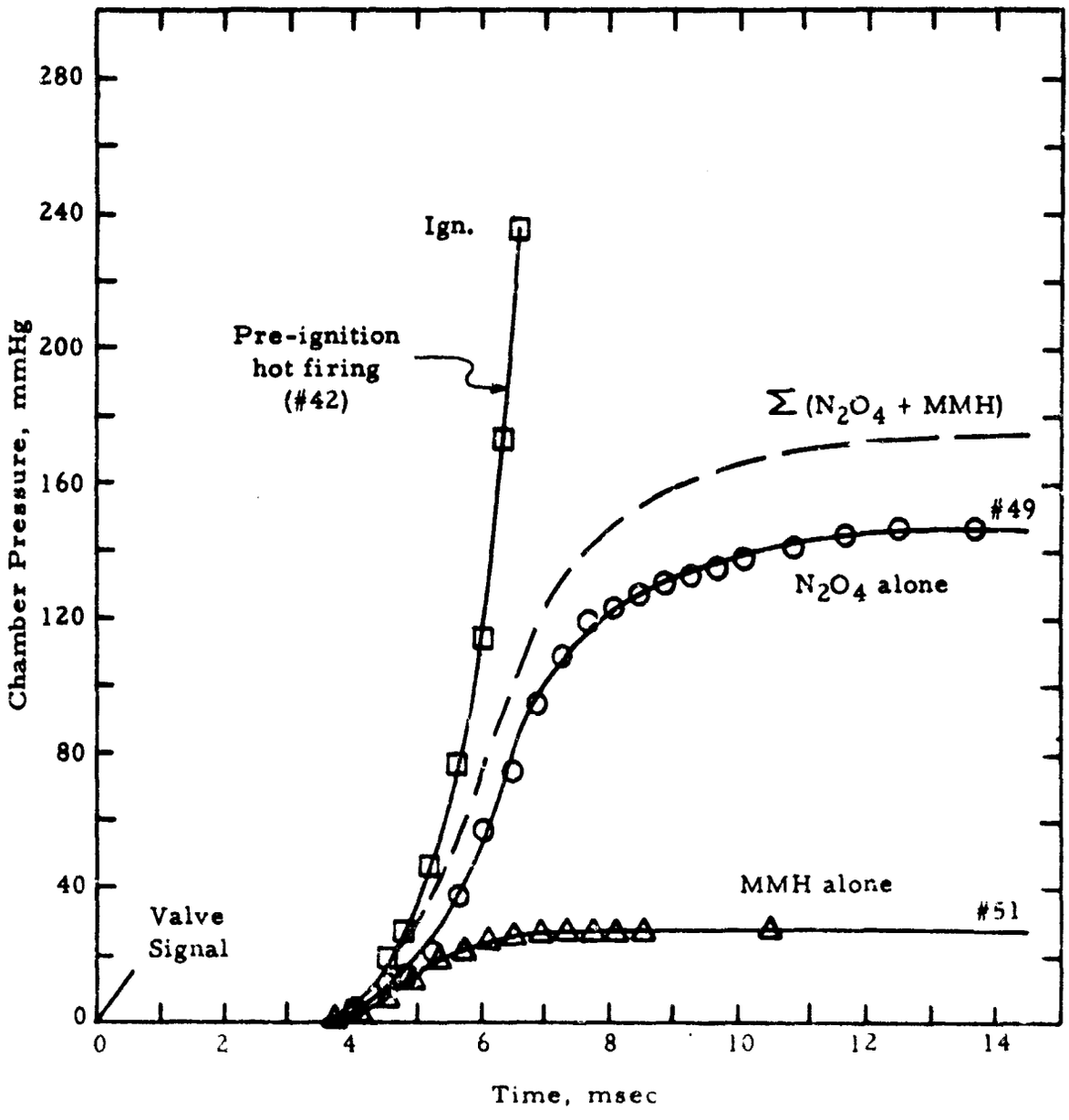

Figure 12. Experimental Chamber Pressurization Curves for Cold Flow and Hot Firing - Engine Configuration No. 2.

c. Cold Flow and Hot Firing Chamber Wall Temperature Histories

Experimental thrust chamber wall temperature histories were measured for singly flowed N_2O_4 and MMH in Engine Configurations 1 and 2. Wall temperature histories were also obtained for hot firings in Engine Configuration No. 1.

The measurements were made using a high-response (approximately 10 microsecond response time) chromel-alumel Nanmac surface junction thermocouple flush mounted in the cylindrical portion of the nozzle section and diametrically opposite the Kistler 701A transducer. The cold junction of the thermocouple was at 32°F. Oscillograms of cold flow tests with each propellant in the two engines are given in Fig. 13.

In the oscillograms, the upper trace is valve current, the middle trace is chamber pressure (Kistler 701A), bottom trace is the inside surface wall temperature as given by the flush mounted Nanmac thermocouple. The polarity of the recorder is such that an upward deflection of the thermocouple trace means a decrease in temperature. Time bases for the oscillograms are 2 msec/cm for the left-hand column and 20 msec/cm for the right hand column. Other pertinent data and scale factors are given in Table VI.

Although the same tank pressures were used as in the earlier runs given in Figs. 9 and 10, the flowrate of the oxidizer is lower in the present runs as indicated by the chamber pressurization curves for N_2O_4 in Fig. 13 versus the corresponding curves of Figs. 9 and 10. Apparently partial plugging of the oxidizer passages occurred during the interval between the two groups of tests. The reduced N_2O_4 flowrate however does not negate the wall temperature trends measured in these runs.

In the case of a singly flowed propellant through the one-on-one doublet injector, the propellant initially impinges on the chamber wall at a localized area. Chamber wall cooling is therefore non-uniform as may be seen by comparing the top two oscillograms of Fig. 13 with the two directly below. The nozzle section, and therefore the

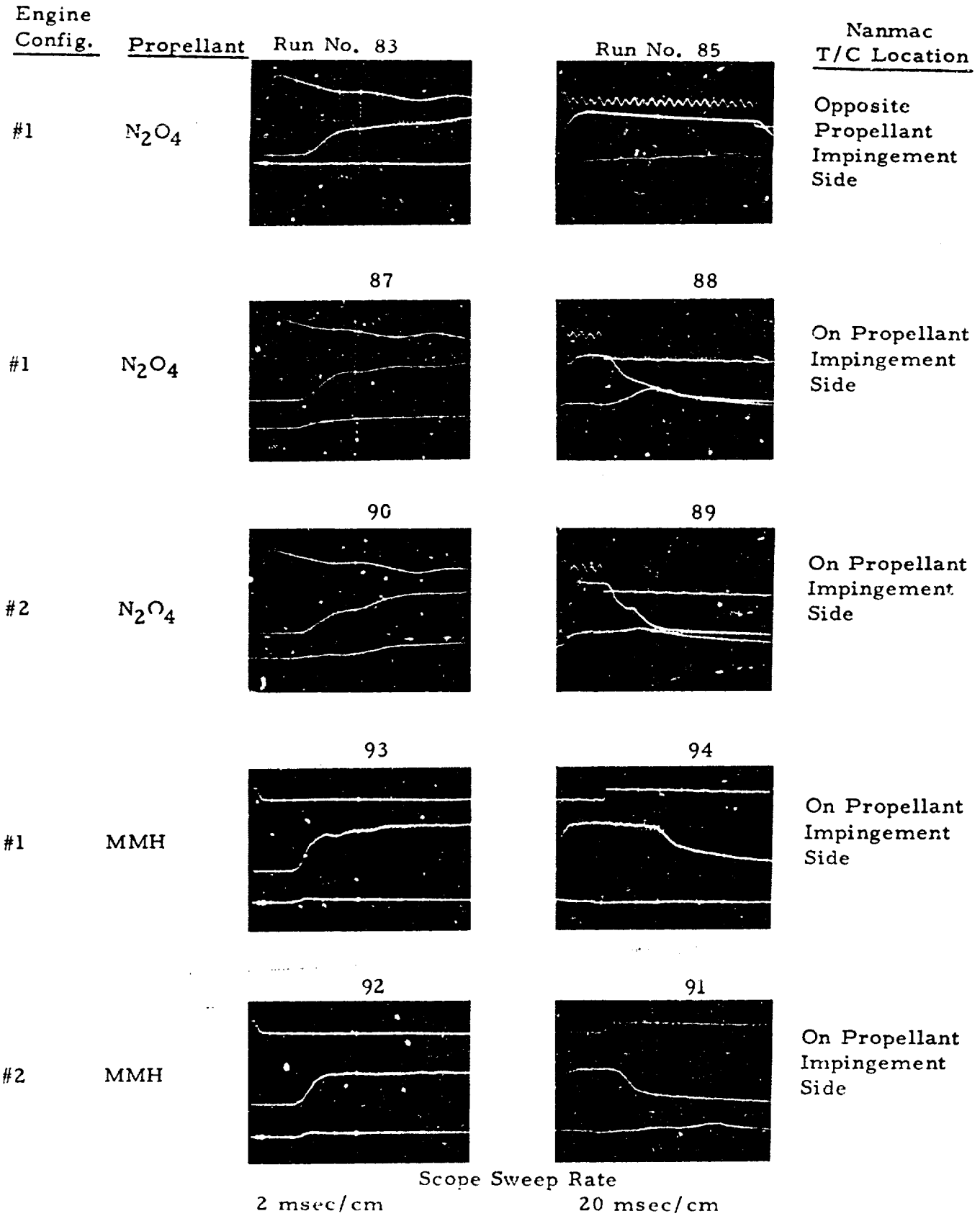

Figure 13. Experimental Chamber Wall Temperature Histories for Singly Flowed N_2O_4 and MMH in Engine Configurations 1 and 2

TABLE VI

PERTINENT DATA AND SCALE FACTORS FOR OSCILLOGRAMS OF FIGURE 13

Run No.	Propellant	Engine Configuration	Propellant and Hardware Temperature °F ± 2°	Scale Factors P_c-701A mmHg/cm	Scale Factors Sweep Rate msec/cm	Thermocouple Location *
83	NTO	#1	81	103	2	Opposite
85	NTO	#1	81	103	20	Opposite
87	NTO	#1	80	103	2	On
88	NTO	#1	80	103	20	On
90	NTO	#2	80	51.5	2	On
89	NTO	#2	80	51.5	20	On
93	MMH	#1	80	20.6	2	On
94	MMH	#1	80	20.6	20	On
92	MMH	#2	80	20.6	2	On
91	MMH	#2	80	20.6	20	On

* Relative to chamber side on which propellant stream impinges.

Parameters Common to All Runs of Figure 13:

Initial Ambient Pressure = 0.3 mmHg
Propellant Tank Pressure - N_2O_4 = 740 psig
Propellant Tank Pressure - MMH = 710 psig
Steady State N_2O_4 Flowrate = less than 0.120 lb_m/sec
Steady State MMH Flowrate = 0.075 lb_m/sec
Injector: 1-on-1 doublet
Scale Factor:
Nanmac Thermocouple = 1 mv/cm or approx. 47F9cm

thermocouple, could be rotated relative to the injector in 90° steps. In Runs 83 and 85, the thermocouple was located on the side of the chamber opposite the localized impingement area and it registered only a slow, gradual decrease in wall temperature. In Runs 87 and 88 as well as in the remaining runs of Fig. 13, the thermocouple was located on the same side of the chamber as the principal localized impingement area. In these cases, wall temperature begins to decrease very soon after the pressure begins to rise in the chamber. The extent of wall cooling near the localized impingement area is markedly greater with N_2O_4 as propellant than with MMH.

The oscillograms with the slower sweep rates indicate that the temperature of the wall near the localized impingement area decreases fairly quickly to a level which remains approximately constant until shutdown. With a given propellant the nearly constant wall temperature during a run is slightly lower for a lower design chamber pressure, as may be seen by comparing Runs 89 with 88 for N_2O_4 and 91 with 94 for MMH.

At shutdown, wall temperature undergoes further cooling, as shown most noticeably in Run 88. The increased wall cooling during tail-off is attributed to vaporization of propellant which had coated the wall surface during the run time. This behavior is observed to a greater or lesser extent for both propellants and both engine configurations tested.

The wall temperature histories of Fig. 13 indicate significant cooling even during typical ignition delay times. The start of wall cooling lags only slightly (approx. 1/2 msec) the start of chamber pressure increase due to propellant vaporization. However, cooling of the walls is non-uniform over the inside surface of the chambers. The curves suggest also that the walls become coated with propellant during the runs, the propellant acting as insulation to slow, together with the cooled walls, subsequent heat addition to the vaporizing vapor/drop system.

Wall temperature histories were also measured during hot firings of Engine Configuration No. 1. Oscillograms for these runs are shown in Fig. 14 together with oscillograms of appropriate cold flow tests from Fig. 13. In the oscillograms for the hot firings, the upper trace is a combined valve current trace, the middle trace is wall temperature (Nanmac thermocouple) and the bottom trace is chamber pressure (Kistler 701A). As before, a decrease in temperature causes and upward deflection of the thermocouple trace. Also, the N_2O_4 flowrate is at a reduced level as in the cold flow runs of Fig. 13. Pertinent data and scale factors for the oscillograms of Fig. 14 are given in Table VII.

Nanmac Thermocouple Location Relative to Injector Orifices:

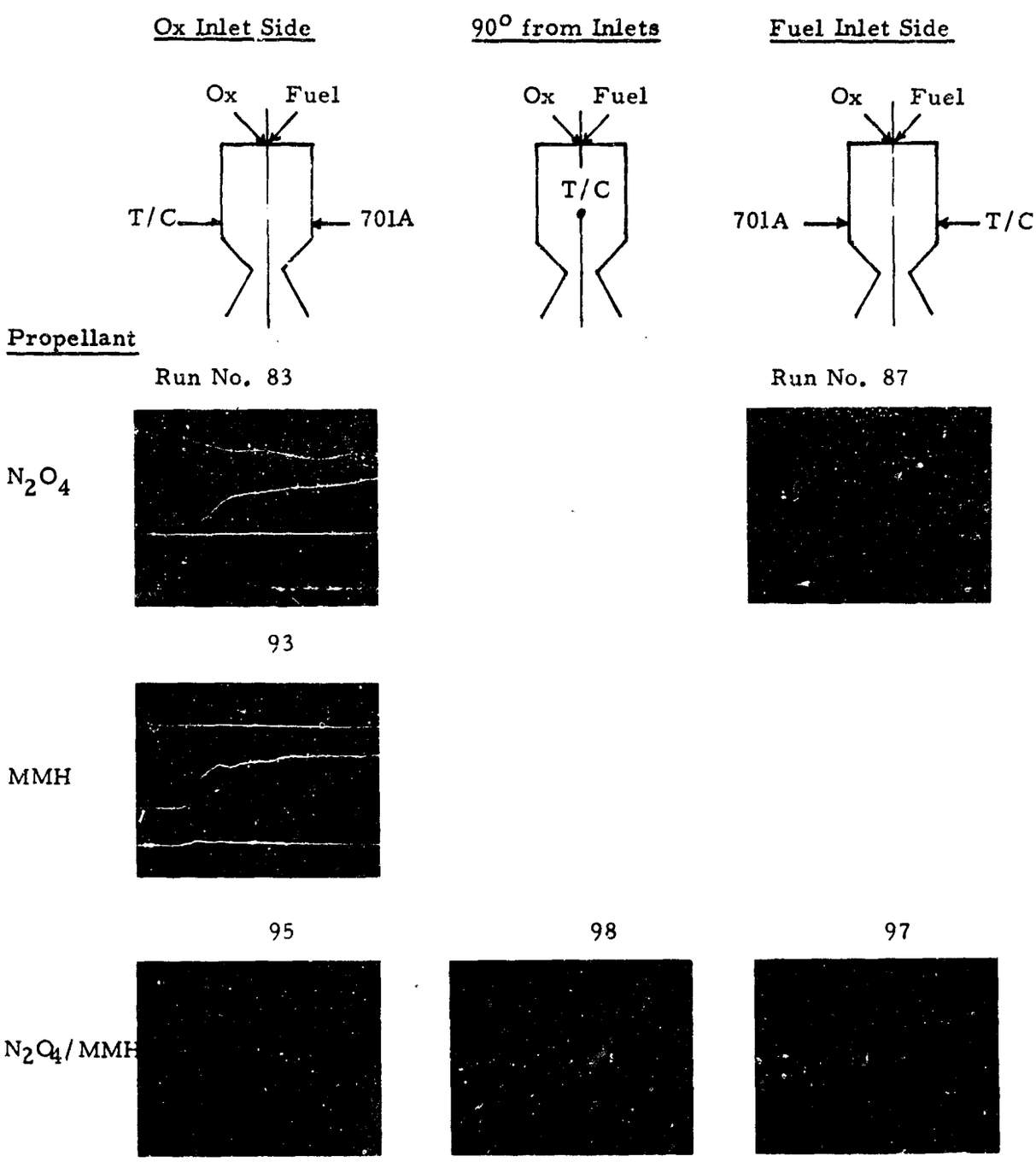

Figure 14. Experimental Chamber Wall Temperature Histories for Cold Flow and Hot Firings in Engine Configuration No. 1

TABLE VII

PERTINENT DATA AND SCALE FACTORS FOR OSCILLOGRAMS OF FIGURE 14

Run No.	Propellant	Propellant and Hardware Temperature °F ± 2°	Scale Factors		Thermocouple Location
			P_c-701A mmHg/cm	Sweep Rate msec/cm	
83	NTO	81	103	2	Ox Inlet Side
87	NTO	80	103	2	Fuel Inlet Side
93	MMH	80	20.6	2	Ox Inlet Side
95	NTO/MMH	80	103	2	Ox Inlet Side
98	NTO/MMH	82	103	1	Between Inlets
97	NTO/MMH	81	103	1	Fuel Inlet Side

Parameters Common to All Runs of Figure 14.

Initial Ambient Pressure = 0.3 mmHg
Propellant Tank Pressure - N_2O_4 = 740 psig
Propellant Tank Pressure - MMH = 710 psig
Steady State N_2O_4 Flowrate = less than 0.120 lb_m/sec
Steady State MMH Flowrate = 0.075 lb_m/sec
Injector: 1-on-1 doublet
Engine Configuration: No. 1
Scale Factor:
Nanmac Thermocouple = 1 mv/cm or approx. 47F°/cm

As discussed above, the cold flow oscillograms of Fig. 14 indicate significant wall cooling near the localized impingement point for each propellant singly flowed. The wall temperature traces for the hot firings of Fig. 14 exhibit a quite different behavior. Regardless of the orientation of the thermocouple relative to the propellant injection orifices, the wall temperature trace, during the ignition delay period, initially deflects upward very slightly (slight wall temperature decrease) and then deflects noticeably, though gradually, downward (wall temperature increase). At ignition, a discontinuity in the downward deflection occurs, indicating greater wall heating. The point of interest here is that wall temperatures decrease in cold flow tests but, in hot firing, wall temperatures decrease very slightly initially and then increase during the remainder of the ignition delay period. The wall temperature increase (obtained at all three thermocouple locations) during the ignition delay period is clear evidence of heat evolution from pre-ignition reactions.

C. INJECTOR FLASHING EFFECTS ON PRE-IGNITION CHAMBER PRESSURIZATION

High speed schlieren movies readily record that when propellant emerges from an injector following valve opening, the propellant emerges as a vapor initially, then as a vapor/liquid mixture, and finally as all liquid flow. The reduced mass flow during this flow build-up period slows the vaporization pressure rise in a thrust chamber from the pressurization rates that would result from a step-function increase in propellant flowrate. Injector flashing effects must therefore be incorporated into the chamber pressurization analysis given in Sec. III. A. That analysis as presented assumes a step increase in propellant flowrate at time zero.

A rigorous theoretical treatment of the problem of transient flow increase upon valve opening involves flash vaporization, feed system dynamics, complex heat transfer problems, two phase flow, etc. and is beyond the scope of the present six-months program. Nevertheless the transient flow period is treated empirically for the specific feed system/propellant valves/injector (1-on-1) assembly used during the program.

As a first approximation, the mass flowrate is assumed to increase linearly with time until the nominal steady state flow is reached. Then, in Eq. 1 of Sec. III. A, the mass of propellant W_j injected during one time interval Δt_N becomes:

$$W_j = \dot{w}_{ss}\Delta t_N\left(\frac{1}{t_{ss}}\right) \quad \text{if} \quad 0 \leq t < t_{ss} \tag{21a}$$

and $$W_j = \dot{w}_{ss}\Delta t_N \quad \text{if} \quad t_{ss} \leq t < \infty \tag{21b}$$

where t_{ss} is the time to reach the nominal steady state flowrate, $\dot{w}_{ss}$.

Since the mass of an ensemble (j values) of drops injected in one time interval must remain constant (i. e. mass of drops plus mass of vapors generated from these drops is constant) as the ensemble is "operated on" in succeeding time intervals (N values), Eq. 21a is modified for use in the computer program giving:

$$W_j = \dot{w}_{ss}\,(\Delta t_N)^2\left(\frac{N - j' + 0.5}{t_{ss}}\right) \quad \text{if} \quad 0 < N < \left(\frac{t_{ss}}{\Delta t_N} + \theta\right) \tag{22}$$

$$\text{and } \left(N - \frac{t_{ss}}{\Delta t_N}\right) < j' \leq N$$

where θ = drop residence time expressed in number of time intervals and $j' = N - j + 1$. (It is more convenient for the machine calculations to use j'-values rather than the j-values as defined in Sec. III. A).

The effect of using Eqs. 22 and 21b in place of $W_j = \dot{w}\,\Delta t_N$ of Eq. 1 is shown in Fig. 15 for N_2O_4 and MMH in Engine Configuration No. 1. The two solid curves in the figure are obtained from the equations given in Sec. III. A applied to Engine Configuration No. 1 (Table I) with the experimental conditions given in Table IV. The equations assume a step function increase in flowrate.

The two dashed curves in Fig. 15 are obtained using Eqs. 22 and 21b to describe the flow increase. Values of t_{ss} were obtained by curve fitting, 1. 6 msec and 0. 8 msec (from propellant entry) for N_2O_4 and MMH, respectively, giving adequate agreement between the initial portions of the experimental and computed chamber pressurization curves. The discrepancies between the latter portions of the experimental and computed curves are due to wall heating effects which are described in the following section.

D. WALL HEATING EFFECTS ON PRE-IGNITION CHAMBER PRESSURIZATION

From comparisons of experimental and calculated chamber pressurization histories for singly flowed propellants, it was concluded in the previous program that heat is transferred from the chamber walls to the vaporizing vapor/drop system during an ignition delay period (1). The added energy leads to significantly higher vaporization chamber

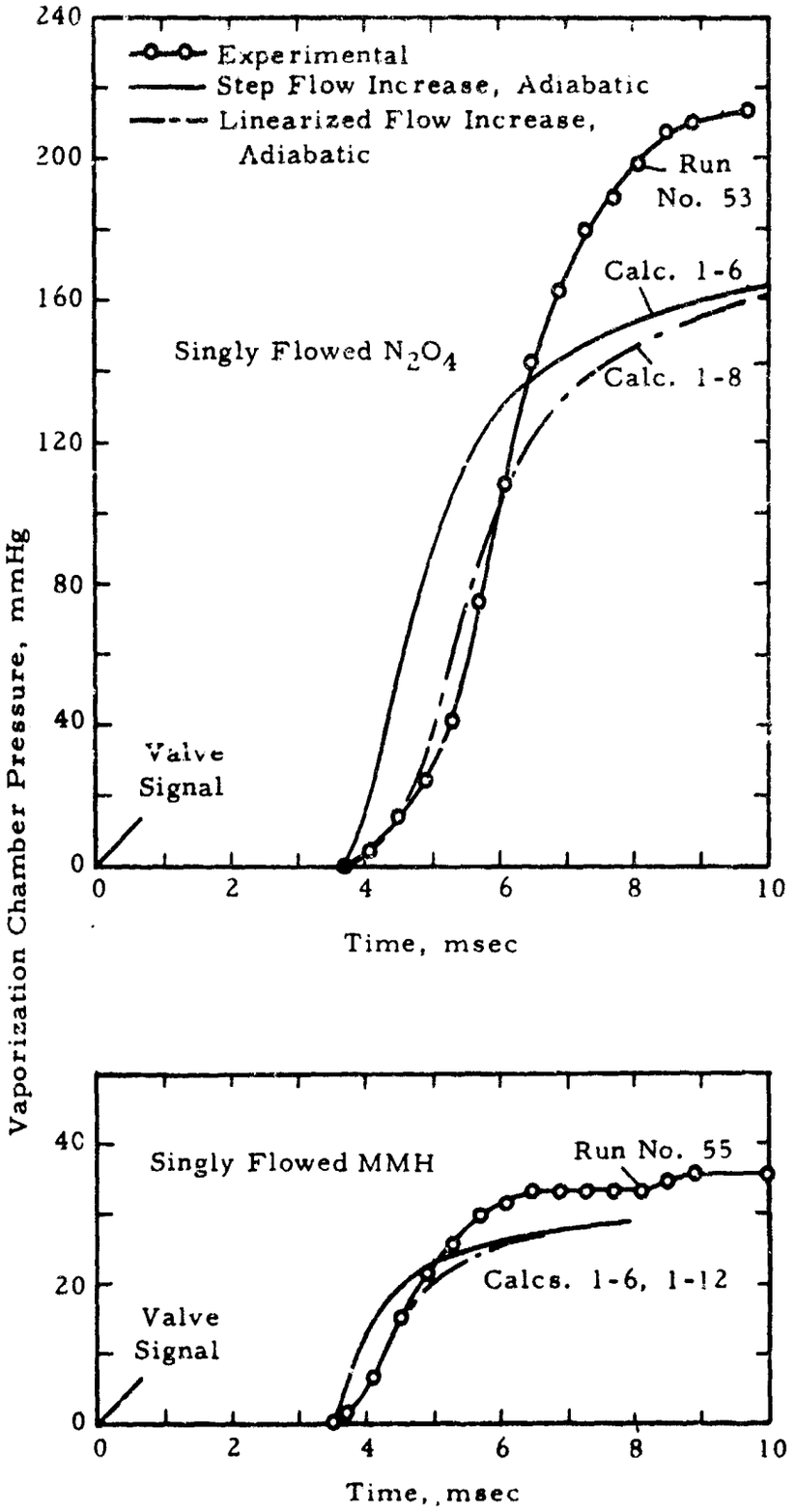

Figure 15. Effect of Linearized Flow Increase on Chamber Pressurization by N_2O_4 (top) and MMH (bottom) in Engine Configuration No. 1.

pressures than would result from an adiabatic vapor/drop system (Fig. 15).

In the present program, three possible mechanisms for pre-ignition heat transfer between injected propellants and thrust chamber walls have been considered: radiant heating, convective heating of propellant vapor, and conductive heating of droplets upon impingement with chamber walls. Because of the low temperatures involved (0° to $85^{\circ}F$), radiant heating is insignificant. Also convective heating of propellant vapors is relatively minor, amounting to only a 5 to $10^{\circ}F$ gas temperature increase, depending on engine configuration. The temperature increase was calculated by conventional methods for convective heat transfer in a tube (6).

The problem of conductive heating of propellant droplets impinging upon chamber walls is complex. A rigorous theoretical treatment would take into account drop shattering and the effects thereon of various impingement angles and velocities, gradual wetting of the chamber walls and the resulting "insulation" effect, contact area between drops and the walls, varying total drop surface area over which vaporization occurs, varying wall surface temperature, etc. Such a treatment, of course, is beyond the scope of the present program. The effects of conductive droplet heating have nevertheless been accounted for by empirically determining time-dependent coefficients for the time-varying drop temperatures of the three drop-size spray model. The time dependent characteristic of the coefficients is required to account for the experimentally determined fact that chamber wall surfaces cool during the propellant vaporization period (Fig. 13).

Drop heating is caused to begin in the computer program once the initially entering drops have been in the system long enough to travel to the chamber walls. Once a drop reaches the walls, its temperature, which has been and continues to be calculated by Eq. 16 of Sec. III. A, is increased by a fraction, f, of the temperature difference between the chamber wall and the theoretical new drop temperature, i. e.

$$(T_{dij})'_N = (T_{dij})_N + f\left[T_w - (T_{dij})_N\right] \qquad (23)$$

The fraction f is time-dependent initially to reflect cooling of the chamber walls (T_w in Eq. 23 is held constant at the initial hardware temperature). The fraction f therefore starts at a high value, f_{max}, and decreases with time to a lower value. f_{min}, which thereafter remains constant i. e.

$$f = (f_{max} - f_{min}) \left(1 - \frac{t - \frac{D_{iw}}{V_d}}{t_{dh}} \right) + f_{min} \quad \text{if} \quad \frac{D_{iw}}{V_d} < t < \left(\frac{D_{iw}}{V_d} + t_{dh} \right) \tag{24a}$$

$$\text{and } f = f_{min} \quad \text{if} \quad \left(\frac{D_{iw}}{V_d} + t_{dh} \right) \leq t < \infty \tag{24b}$$

$$\text{For completeness, } f = 0 \quad \text{if} \quad 0 \leq t \leq \frac{D_{iw}}{V_d} \tag{24c}$$

The factors required by Eqs. 23 and 24 to empirically account for wall heating are therefore f_{max}, f_{min}, t_{dh} (the time interval during which f goes from f_{max} to f_{min}), and D_{iw} (the pathlength a drop traverses from its injector orifice to impingement on the chamber wall). The former three are obtained empirically by curve fitting; the latter, D_{iw}, is calculated from the chamber geometry and the propellant injection angle.

The effects of using Eqs. 23 and 24 to account for wall heating are shown in Figs. 16 and 17 for N_2O_4 and MMH in Engine Configurations 1 and 2. The computed curves take into account the appropriate engine geometry (Table I) and the conditions of the appropriate experimental runs (Table IV). The figures show reasonable agreement between the experimental chamber pressurization curves for each propellant singly flowed in each engine and the corresponding calculated pressurization curves which include wall heating as well as the linearized flow increase discussed above. The empirically determined values for the coefficients and factors for including wall heating and linearized flow increase in the calculated curves of Figs. 16 and 17 are:

	Engine Configuration No. 1		Engine Configuration No. 2	
	N_2O_4	MMH	N_2O_4	MMH
t_{ss}, msec	1.6	0.8	1.6	0.8
f_{max}	0.15	0.15	0.25	0.25
f_{min}	0.02	0.02	0.03	0.03
t_{dh}, msec	2.5	2.5	2.5	2.5

The calculations show that many N_2O_4 drops evaporatively cool to the freezing point, 11.8°F, and then progressively solidify as evaporation continues. In contrast, none of the MMH drops reaches the freezing temperature, -62°F. In the drop heating calculations, those N_2O_4 drops

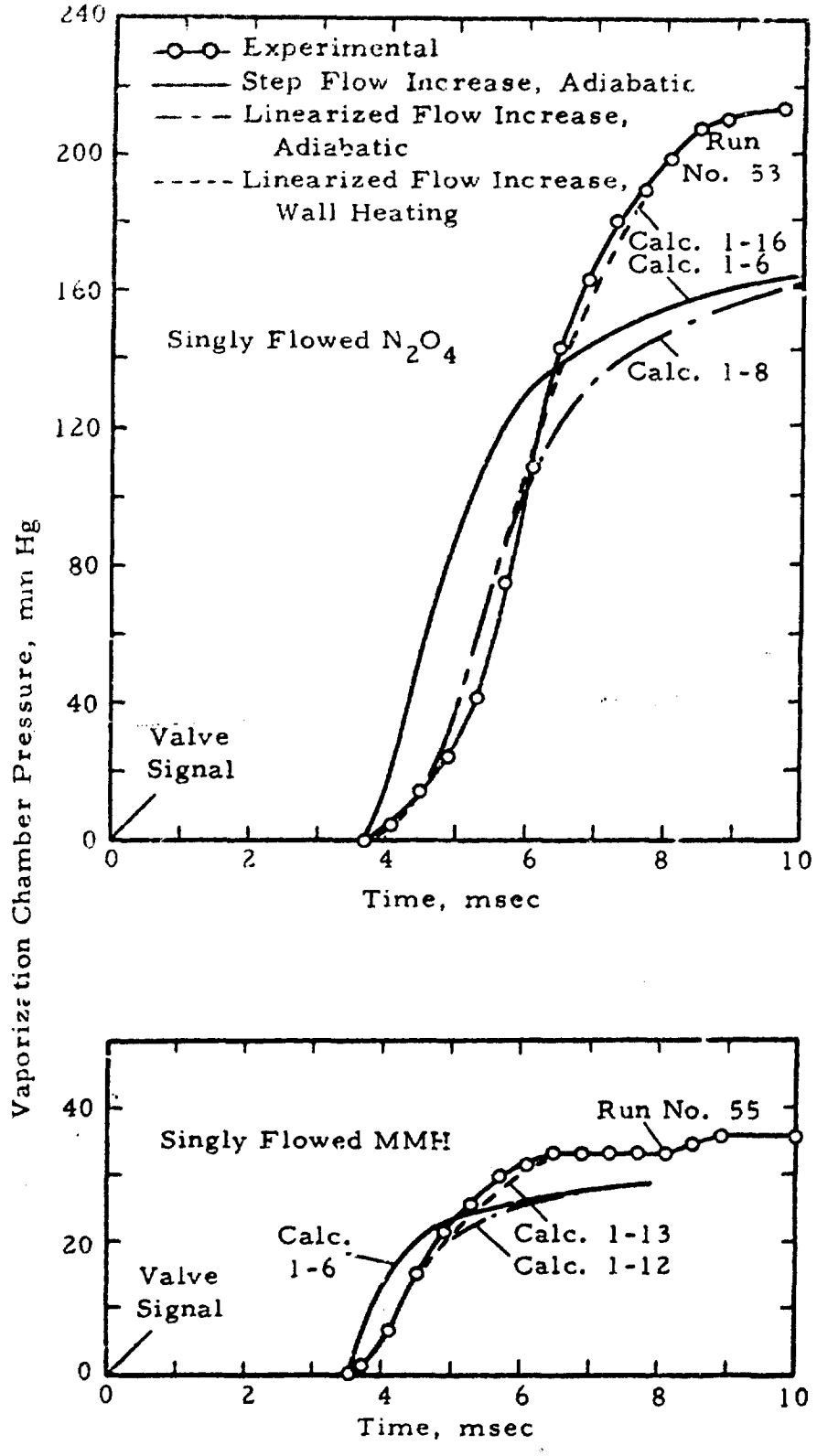

Figure 16. Experimental and Analytical Chamber Pressure Histories for Singly Flowed N_2O_4 (top) and MMH (bottom) in Engine Configuration No. 1.

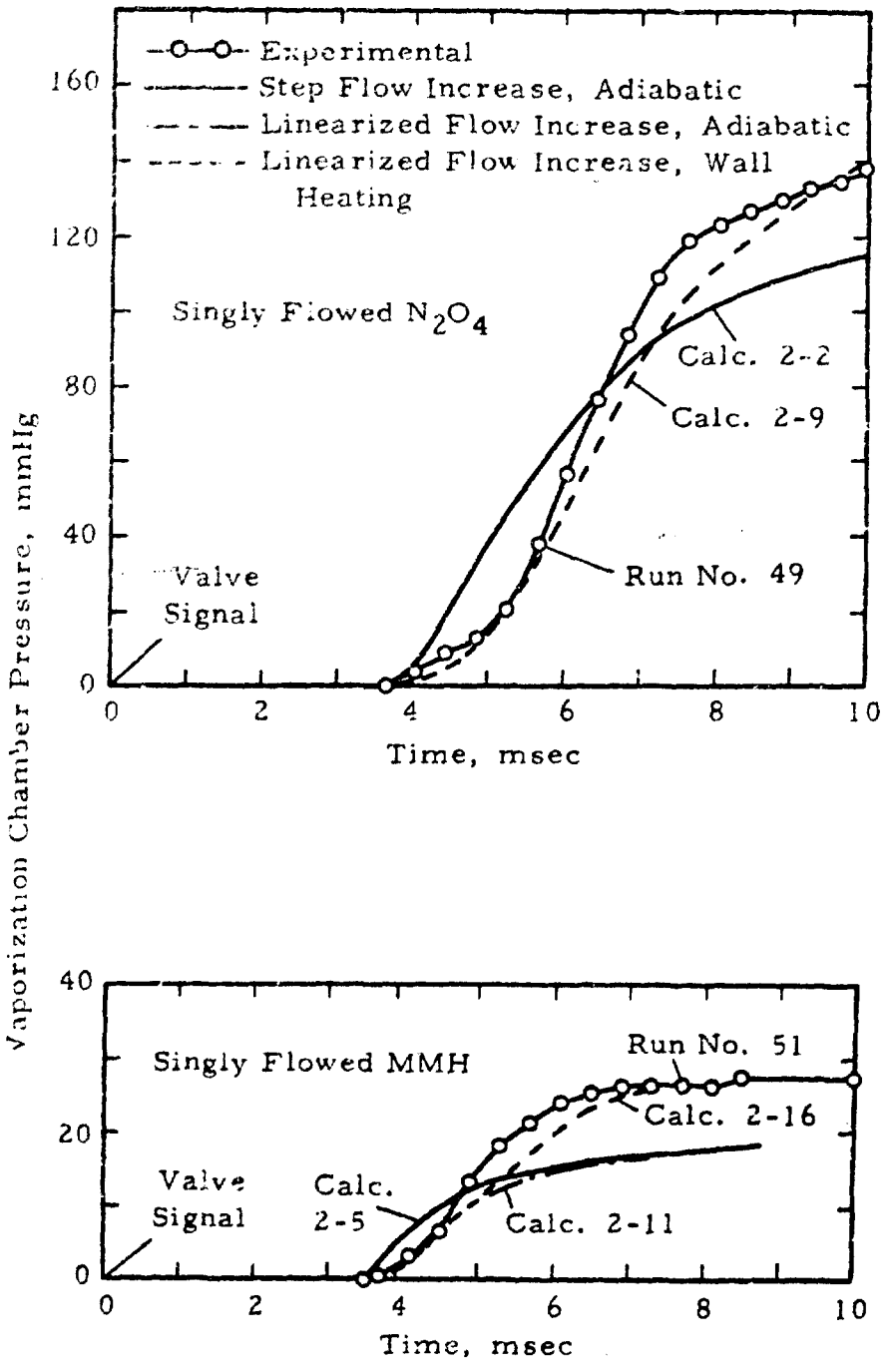

Figure 17. Experimental and Analytical Chamber Pressure Histories for Singly Flowed N_2O_4 (top) and MMH (bottom) in Engine Configuration No. 2.

having a frozen fraction X_{ij} (Eq. 19) of less than 0.6 when they first reach the chamber wall are first melted, upon impingement with the wall, and then their temperatures are augmented (by Eqs. 23 and 24) in subsequent time intervals. Those N_2O_4 drops having a frozen fraction of 0.6 or greater at impingement with the chamber walls are assumed to ricochet off the walls without being warmed.

The calculated curves which include drop heating and linearized flow increase satisfactorily reproduce the chamber pressurization histories of the singly flowed propellants. Thus, the calculations satisfactorily predict the dashed curves of Figs. 11 and 12 for Engine Configurations 1 and 2, respectively. In addition, the calculations give the gas temperature history in each engine the vapor mass histories of each propellant in the chambers, time-dependent propellant vaporization rates, vapor flowrates through the nozzles, drop temperature histories, etc. The next step in the development of the mathematical model for hypergolic ignition delay in space-ambient engines is to account for the disparity between the dashed curves of Figs. 11 and 12 and their corresponding experimental pre-ignition curves for hot firings given in the same two figures. This step requires an understanding of the pre-ignition reactions which occur during an ignition delay period with these propellants. The next section of the report is concerned with these pre-ignition reactions, the reaction intermediate formed, and the method by which to incorporate formation of the reaction intermediate into the ignition delay model.

SECTION IV

PHASE II - CHEMICAL KINETICS ASPECTS OF PRE-IGNITION CHAMBER PRESSURIZATION

In the case of nitrogen tetroxide/hydrazine-type fuels as propellants, a condensed phase reaction product has been observed during engine testing at simulated altitudes. This section of the report is concerned with the role of this reaction product in hypergolic ignition delay. The general experimental conditions under which the reaction product has been observed are briefly discussed first. Then, the explosive characteristics of the material as determined from standard hazard evaluation tests are described. Next, some physical properties of the material are given, followed by discussions of the composition of the liquid reaction product, its heat of formation, and its formation kinetics. Finally in this section of the report, the manner in which formation of the reaction product affects ignition delay time is analyzed.

A. OCCURRENCE AND APPEARANCE OF SUB-IGNITION REACTION INTERMEDIATE

1. Laboratory Occurrences

The overall kinetic factors of ignition reactions of N_2O_4/hydrazine-type fuels were experimentally determined at Thiokol-RMD during a previous program on hypergolic ignition at reduced pressures (Contract No. AF04(611)-9946, Part II). It was found that a condensed phase reaction product formed from vapor-phase reactants under conditions of room temperature and low (sub-ignition) pressures (1). The material appeared as a clear, yellow, viscous liquid of low vapor pressure. Sub-ignition reaction intermediates were found for N_2O_4 in combination with MMH, 50-50, UDMH and N_2H_4. The quantity of material formed depended on the fuel: MMH and 50-50 giving approximately ten times as much as UDMH, and N_2H_4 yielding only very small amounts under the conditions of the experiments.

The occurrence of a reaction intermediate in the N_2O_4/N_2H_4 system has been observed elsewhere under very different experimental conditions (7, 8). Using infrared absorption spectroscopy, Weiss monitored low temperature reactions of solid-phase N_2O_4/N_2H_4 at atmospheric pressure. Upon gradual warming of the reactants from an initial temperature of liquid nitrogen, Weiss found one reaction with little heat evolution occurring at temperatures as low as -205°F. A further reaction, involving measurable heat evolution, occurred at about -75°F. The spectrum of the higher temperature reaction was found to agree well with that of hydrazinium nitrate.

In experiments conducted by the Bureau of Mines (8), mixtures of granulated N_2O_4/N_2H_4 at liquid nitrogen temperature were permitted to warm at atmospheric pressure. Eventually, while the mixture still appeared to be frozen, a violent reaction occurred and often a yellow, viscous, liquid residue remained. From IR spectra of the residue and other spot tests it was concluded that the residue contains an appreciable percentage of hydrazinium nitrate which is a moderately unstable explosive.

While the work of Weiss and of Christos et al corroborate the existence of important reaction intermediates in N_2O_4/N_2H_4 systems, the initial conditions of the reactants in their experiments differ greatly from those in an engine. In Section III of this report, it is found that the fuel (MMH) does not freeze during the ignition delay period and that, although the smaller N_2O_4 droplets do freeze, the minimum oxidizer drop temperatures at near 0°F. Also, for a propellant feed temperature of 75°F, the minimum average gas temperature in a typical engine is about 25°F. Finally, the gas pressure increases from near zero of space to 100-300 mmHg, depending on engine configuration, during the ignition delay period.

2. Deduction from Experimental Engine Tests

Indications of appreciable pre-ignition chemical reactions involving substantial heat release are found in Figs. 11 and 12. In these figures, experimental chamber pressure-time histories of singly flowed propellants in Engine Configurations 1 and 2 are plotted together with hot firing, pre-ignition P_c-time curves. The dotted curve in each figure is simply the sum of the pressure curves of each propellant singly flowed. Good agreement exists between the sum-of-partial-pressures curves and the pre-ignition hot firing curves for the first millisecond of the rising pressures. A gradual divergence then begins, the hot firing pre-ignition curves rising more steeply than the sum-of-partial pressure curves. For both engine configurations, the slopes of the two hot firing pre-ignition curves increase with time until ignition occurs. The divergences, which reach 100-130 mmHg at ignition, are evidence of appreciable pre-ignition reactions

A further indication of pre-ignition reactions comes from the chamber wall temperature data given in Section III. B. 2. c. The oscillograms of Figs. 13 and 14 show that wall temperatures decrease in the case of singly flowed propellants but that, in a hot firing, wall temperatures begin to increase early in the ignition delay period.

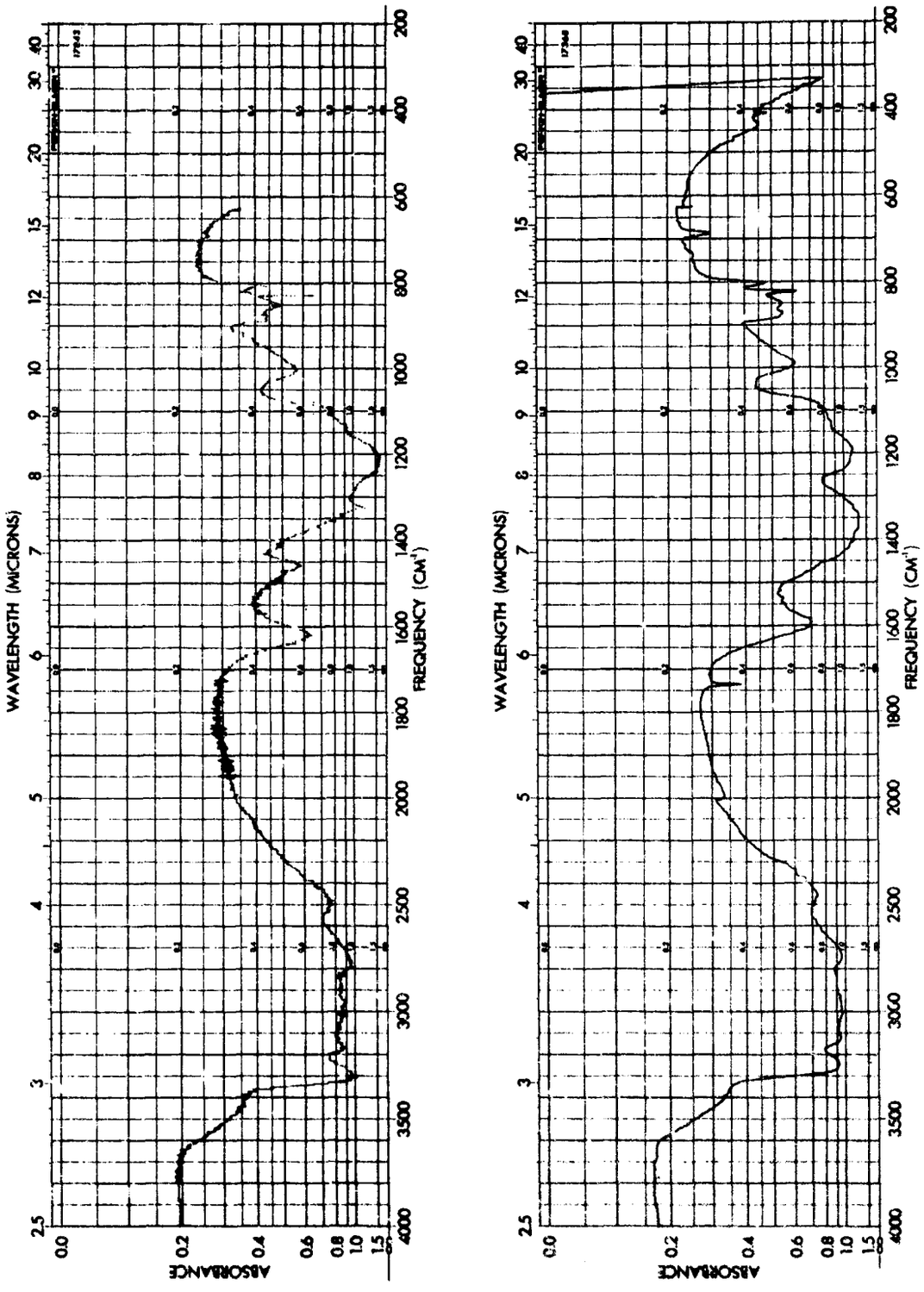

Figure 18. IR Spectra of Liquid-Phase Reaction Intermediates of N_2O_4/MMH Produced in an Engine (top) and in a Laboratory Apparatus (bottom).

3. Engine-Produced vs. Laboratory-Produced Reaction Intermediates.

IR absorption spectra of engine-produced and laboratory-produced reaction intermediates of N_2O_4/MMH are given in Fig. 18. The spectrum of the laboratory-produced material is taken from Reference 1. The liquid-phase sample was produced from an undiluted, stoichiometric mixture of the reactants in a pyrex flow system at low pressure (6 mmHg) and room temperature (Sec. IV. A. 4, below).

The engine-produced material and its spectrum were obtained under another program at Thiokol-RMD (9). The 100-lb thrust engine was operated in a pulse mode at a simulated altitude of approximately 125,000 ft. The pulsing rate was 2 hertz with an electrical pulse width of 10 msec. Hardware and propellant feed temperatures were 60°F. Under these conditions of very short pulse width and relatively long off-time, ignition did not occur during the 160 pulses of the test sequence. Consequently, sufficient material was available at the conclusion of the pulse train to permit collection and limited analysis.

As shown in Fig. 18, the spectrum of this sample is very similar to that of the laboratory-produced material. The only significant difference concerns the absorptions between 1250 and 1500 cm^{-1}. In this region, the laboratory material exhibits one broad absorption band, characteristic of a nitrate. In contrast, the engine-produced material has a weak absorption band at about 1325 cm^{-1} plus another band at about 1460 cm^{-1}.

Other features of the two spectra are essentially identical, including the absorption band at 1200 cm^{-1}. This band is generally attributed to nitrite; however, no nitrite has been detected by wet chemical analyses of the laboratory-produced material (see below, Section IV. D. 1).

It should be pointed out that the laboratory-produced sample was protected from environmental contamination at all times by collecting and maintaining the sample under a dry nitrogen atmosphere. In contrast, ambient air was used to bring the pressure to one atmosphere in the 22-ft diameter vacuum sphere before the engine sample could be withdrawn. Consequently, some contamination of the engine sample could have occurred. Evidence in support of this is given below in Sections IV. B. 1 and 3. Nevertheless, despite some sample contamination or degradation, the IR spectrum of the engine-produced sample is very similar to the spectrum of the laboratory-produced material. The latter is therefore assumed to be the same as the fresh material produced in an engine during an ignition delay period.

4. Production of Material for Analyses and Determinations

The N_2O_4/MMH reaction intermediate used for chemical analyses and property determinations in the present program was produced from gas-phase, undiluted reactants at low (sub-ignition) pressure and room temperature. The experimental apparatus was used initially in the previous hypergolic ignition program and is fully described in the final report of that investigation (1). The apparatus is shown in Figs. 19 and 20 of the present report, the latter figure being a schematic diagram. Briefly, the apparatus consists of vaporizing and flowmetering sections, a flow reactor and a low pressure housing with observation windows.

Gaseous N_2O_4 was taken directly from a No. 3 shipping cylinder (99.5 mole % minimum purity, Matheson Co., Inc.) immersed in a constant temperature bath at 30°C. The heat source was sufficient to maintain steady flow conditions of up to 0.2 gr/sec. The gaseous stream was metered in a Fischer-Porter 2F-1/4-20-5 flowmeter (glass float) at 30°C and 600 mmHg pressure. Under these conditions, the oxidizer exists as a mixture of NO_2 and N_2O_4. Therefore, the flowmeter was calibrated in terms of mass flow by collecting the vapors in a condenser at liquid nitrogen temperature and weighing the mass collected during measured time intervals.

The fuel, MMH, was flowmetered in the liquid state (08F-1/16-20-4/36, sapphire float) and then vaporized drop-wise in a glass coil heated to 90°C. The vapors expanded into a one-liter flask, which was also heated to 90°C, and then passed through an all-glass, heated line to the flow reactor.

The flow reactor shown schematically in Fig. 20 is a 47-mm diameter pyrex tube opened at one end to the ambient pressure of the low pressure vessel. The flow tube is housed inside a metal tube which extends downward from the 1 ft diameter x 3 ft high vacuum vessel (Fig. 19). The pressure in the latter is regulated both by a throttle valve in the connecting line to a high capacity vacuum pump (Kinney KD 780) and by an appropriate bleed of shroud gas (nitrogen) which has the additional function of diluting the corrosive gases.

The procedure for making the reaction intermediate is as follows. The apparatus is first evacuated. Then a bleed of nitrogen shroud gas of about 1 CFM is admitted into the vessel and, by adjusting the throttling valve in the vacuum line, a pressure of about 0.5 mmHg is obtained in the vessel. The desired flowrates of fuel and oxidizer are then set. The ambient pressure in the chamber is then gradually raised by bleeding room air into the vacuum line through an auxiliary, downstream valve. If the pressure is raised sufficiently (5 to 15 mmHg

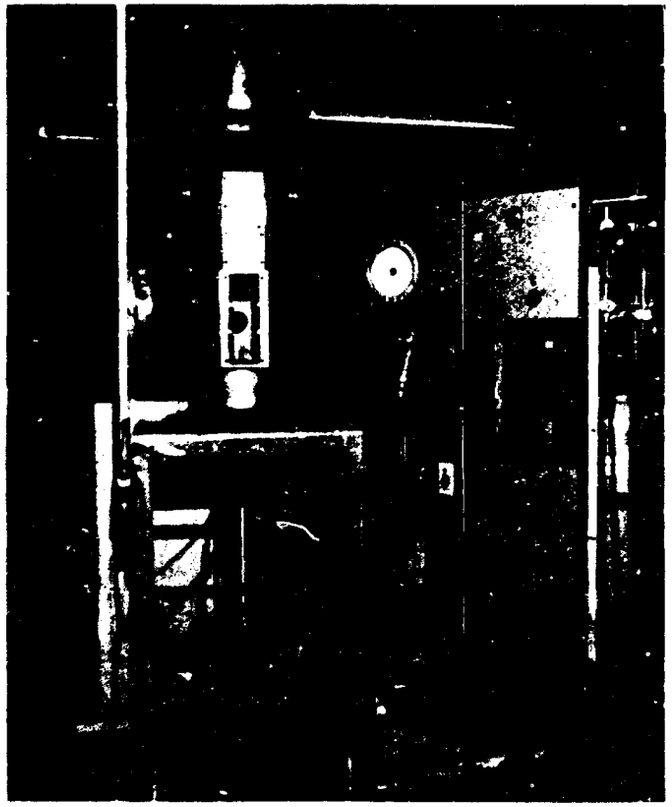

(72-1952)

Figure 19. Low Pressure Apparatus for Production of N_2O_4/MMH Reaction Intermediate

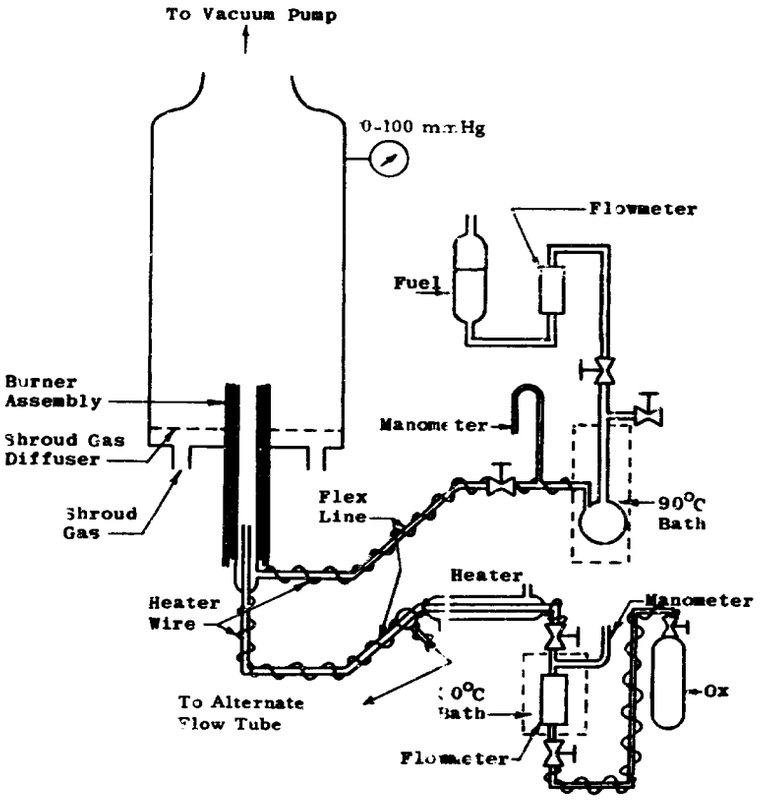

Figure 20. Schematic Diagram of Reaction Intermediate Production Apparatus

depending upon reactant mixture ratio, initial temperature and flow tube diameter) ignition occurs at a well-defined, reproducible, minimum pressure.

If the pressure is held below the minimum ignition pressure smoke is seen issuing from the flow tube. Some of the condensed phase material deposits onto the walls of the flow tube and eventually collects as a viscous yellow liquid at the base of the vertically-oriented flow tube. Six to eight cc of material are collected at a time.

After shutting off the propellant flows, the vacuum vessel and flow tube are filled to one atmosphere pressure with dry nitrogen. The sample is then removed, maintaining a nitrogen atmosphere over the liquid at all times.

Two N_2O_4/MMH mixture ratios were used in making samples for the various analyses and determinations performed during the program. The stoichiometric mixture (O/F = 2.5 by wt.) and an oxidizer-rich mixture (O/F = 5.0) were used, the latter is within the composition range of the vapor-phase reactants in an engine during an ignition delay period (O/F of simultaneously injected liquid propellants of 1.6). The lean vapor-phase mixture results from the higher volatility of the oxidizer.

B. SENSITIVITY CHARACTERIZATION OF REACTION INTERMEDIATE

Because of the unknown composition and characteristics of the N_2O_4/MMH reaction intermediate at the outset of the program, the initial tests performed on the material were of the hazard evaluation type. The purpose of the tests was to signal any need for extraordinary handling procedures and, as a by-product, to provide at least qualitative information on the role of the reaction intermediate in ignition pressure spiking.

The material used in these tests was made from the stoichiometric mixture of N_2O_4/MMH.

1. Impact Sensitivity

The impact sensitivity of a test sample is obtained in drop weight tests by dropping a known weight from various pre-set heights onto a carefully designed cup containing the material. A loud report, puncture of a retaining steel diaphragm, flame or evidence of combustion are all taken as signs of a positive test. The drop height which

yields a 50% probability of initiation is determined. The 50% height for the N_2O_4/MMH reaction intermediate tested is 10 inches using a 2 kg weight. Table VIII gives results for several materials for comparative purposes.

A portion of the engine-produced sample whose IR spectrum is given in Fig. 18 was subjected to drop weight tests under a separate program (9). The material was not sensitive in the drop weight tester at a drop height of 36 inches, the maximum height of the apparatus. The stability of the material is attributed to sample contamination and/or degradation, discussed above.

For comparative purposes, monomethyl hydrazine nitrate ($CH_3N_2H_3 \cdot HNO_3$) was prepared in the laboratory (9). The synthesis route involved the direct reaction of MMH in aqueous solution with a stoichiometric quantity of HNO_3 followed by dehydration and recrystallization. The IR spectrum of the material is given in Fig. 21.

TABLE VIII

DROP WEIGHT AND MODIFIED TRAUZL BLOCK TEST VALUES FOR VARIOUS MATERIALS

Material	Drop Weight 50% Height inch	Trauzl Block Expansion* cc/gr
Nitroglycerir	1	27
Hydrazine nitrate, $N_2H_4 \cdot HNO_3$	4	20
RDX (explosive)	7	25
98% H_2O_2	-	15
Lead Azide, $Pb(N_3)_2$	3**	10
N_2O_4/MMH Reaction Intermediate	10	9
$CH_3N_2H_3 \cdot HNO_3$	15	-
NH_4ClO_4	18	0

* Corrected for volume increase due to blasting cap alone.
**Picatinny Arsenal Apparatus, 2 kg weight (10).

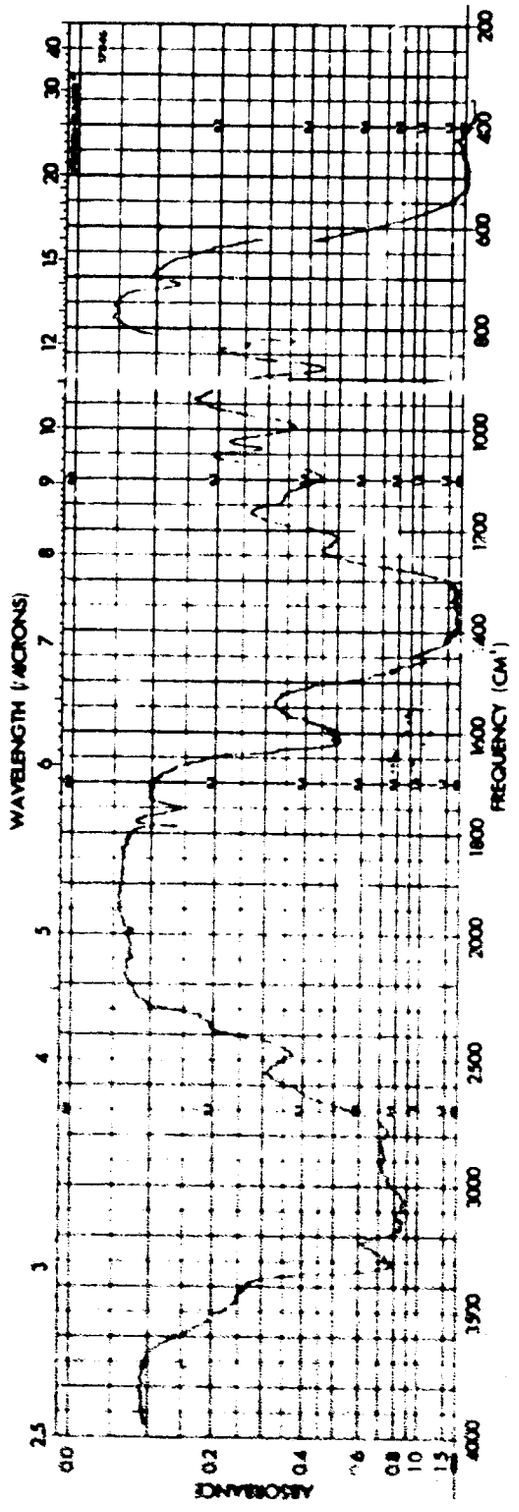

Figure 21. IR Spectrum of Monomethyl Hydrazine Nitrate, $CH_3N_2H_3 \cdot HNO_3$.

The 50% drop height for the synthesized compound was found to be 15 inches, indicating that the laboratory-produced N_2O_4/MMH reaction intermediate is more sensitive to impact than $MMH \cdot HNO_3$.

2. Explosive Strength

Modified Trauzl Block Tests conducted routinely at Thiokol-RMD use a sample size smaller than in standard, full-size Trauzl Block tests. Typically, one to three gram samples are used in a lead cylindrical cup of given dimensions. A standard No. 8 blasting cap is used for initiation. Detonation of the blasting cap in contact with the sample causes an increase in internal cylinder volume. Corrected for the blasting cap effect, the volume change is related semi-quantitatively to the explosive strength of the test sample. The modified Trauzl Block tests on the reaction intermediate gave a corrected expansion of 9 cc/gr for a 2.5 gram sample. This value is close to that of lead azide tested in the same apparatus (Table VIII).

3. Thermal Stability

The standard ICRPG thermal stability test was performed on a sample of reaction intermediate produced in the laboratory. The heating record is shown in Fig. 22 together with similar curves of engine-produced material and $CH_3N_2H_3 \cdot HNO_3$ synthesized from MMH and HNO_3 (9). In each case, the heating bath was programmed to increase at a rate of 8° C per minute. The curves are a record of the differential temperature ($T_{sample} - T_{bath}$) plotted against the temperature of the sample. Because of the polarity of the recorder, positive peaks represent exothermic reaction. The initial dip in each curve is due to the lag in heating of the sample when the bath heater is activated.

The thermogram of the reaction intermediate produced in the laboratory indicates that two exothermic reactions occur: the first starts at about 60°C, the second at about 110°C. The rate and intensity of the second reaction are greater than that of the first. At a sample temperature of 135°C following the strong exothermic reaction, the pressure was sufficient to burst a rupture diaphragm rated at 4700 psi.

The heating curve of the engine-produced material also shows two exotherms; however, they are displaced to slightly higher temperatures indicating somewhat greater thermal stability than the laboratory-produced material. The greater stability is attributed to sample contamination during retrieval (Sec. IV. A. 3). In

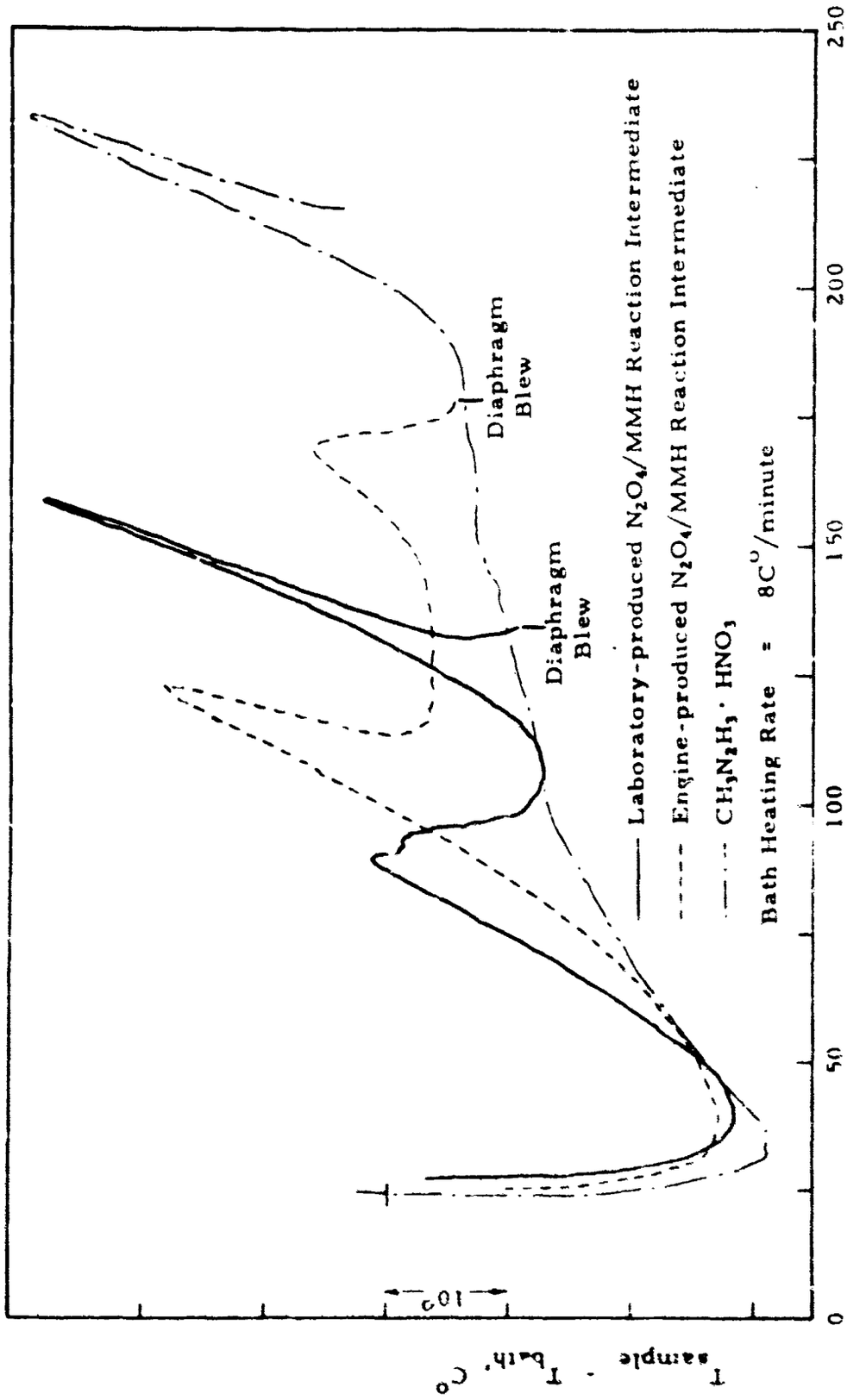

Figure 22. Heating Curves of Standard ICRPG Thermal Stability Tests of Laboratory and Engine Produced N_2O_4/MMH Reaction Intermediates and $CH_3N_2H_3 \cdot HNO_3$

addition, the curves of the two samples show that the intensities of the two exothermic reactions are reversed, indicating that the reactions are not sequential reactions of the same material but rather are due to two materials present in different proportions in the two samples.

The heating curve of monomethyl hydrazine nitrate prepared in the laboratory is significantly different from those of the reaction intermediates (Fig. 22). $MMH \cdot HNO_3$ begins to decompose exothermally at 190°C. The greater thermal stability of this compound over that of the reaction intermediate does not preclude the compound from being a constituent of the intermediates. However, the curves of Fig. 22 indicate that $MMH \cdot HNO_3$ is not the cause of the two exotherms at lower temperatures.

C. PHYSICAL PROPERTIES OF REACTION INTERMEDIATE

Measurements of a few physical properties of the reaction intermediate formed by stoichiometric N_2O_4/MMH in the laboratory apparatus were attempted: liquid density, vapor pressure, freezing point and molecular weight.

1. Liquid Density

The density of the material was determined at three temperatures. The results obtained are:

Temp., °C	Density, gr/cc
3.0	1.205
17.8	1.189
25.0	1.180

2. Vapor Pressure

Vapor pressure measurements of the material at temperatures from 0° to 40°C were attempted using standard techniques. However, values could not be obtained due to gradual but significant decomposition of the test sample throughout the temperature range investigated. Although the decomposition was slow, enough gas evolved to obscure the actual (low) vapor pressure of the sample.

From the laboratory production runs of the reaction intermediate, it could be determined that the vapor pressure of the material is less than 0.5 mmHg at room temperature. This value is, of course, well

below the vapor pressures of the reactants (760 and 41 mmHg at 70°F for N_2O_4 and MMH respectively).

Since it is believed that the reaction intermediate also forms during tail-off of a pulse, it is desirable to know the vapor pressure of the material at various temperatures for considerations of its removal between pulses by the pumping action of a space environment. In this regard, although the decomposition of the sample was sufficient to preclude accurate vapor pressure determinations by conventional techniques, on a gross scale the decomposition is very slow. For example, at the end of one month, the remainder of a batch of material which had been kept in a dry box qualitatively underwent little change in volume, although the original clear yellow color of the liquid did change to nearly water-white.

3. Freezing Point

The shape of a cooling curve of an unknown substance can provide information on whether the material is a pure compound or a mixture of compounds. For this reason, freezing point measurements of the laboratory produced reaction intermediate were attempted; they were unsuccessful, however, due to the very high viscosity of the material. In general, very viscous materials tend to greatly supercool and, when this occurs, accurate and reliable freezing point data cannot easily be obtained. In the present case, freezing points ranging from -20 to -50°C were observed but the data are not deemed reliable due to the viscosity effect. For example, at -10° to -20°C, the material "poured" a distance of one inch in about ten minutes.

4. Molecular Weight

An attempt to determine the molecular weight, or average molecular weight, of the reaction intermediate by the freezing point suppression technique in benzene as solvent was unsuccessful. It was found that the reaction intermediate is not soluble in benzene. Other solvents were not tested.

D. COMPOSITION OF REACTION INTERMEDIATE

To determine the composition of the N_2O_4/MMH reaction intermediate, a number of chemical and instrumental analyses were performed. The liquid samples were produced from vapor N_2O_4 and vapor MMH at sub-ignition pressures (5-9 mmHg) and room temperature in the laboratory apparatus. Two mixture ratios of the reactants were used in making the samples: O/F = 2.5 and 5.0 by wt. The former is the stoichiometric mixture ratio and the latter is within the composition range of the vapor phase reactants in an engine during an ignition delay period (O/F of simultaneously injected liquid propellants of 1.6). The lean mixture results from the higher volatility of the oxidizer.

The initial analyses of the reaction intermediates were made over a period of a few weeks following production of the samples. Because of gradual sample decomposition, which was learned subsequently from the attempted vapor pressure determinations (Sec. IV.C.2), the results of the initial analyses reflect changes in composition due to sample degradation. These results, which suggest that the composition of the reaction intermediate depends upon the mixture ratio of the initial reactants, are discussed subsequently.

The results of analyses given in the next paragraphs were obtained within two days of production of the sample and are taken as representative of freshly produced material in an engine.

1. Results of Analyses of Fresh Sample

A number of chemical and instrumental analyses were made of a fresh sample of the N_2O_4/MMH reaction intermediate and on the residue and condensate of fractionation experiments. The sample on which the analyses were performed was made at low pressure from N_2O_4/MMH at a mixture ratio of 5.0 by wt.

The infrared spectrum of the sample is given in Fig. 23. It is similar to the spectrum obtained under the previous program (1), and reproduced in Fig. 18, except that free MMH is indicated in Fig. 23 by the shapes of the absorptions between 1150 and 800 cm^{-1}.

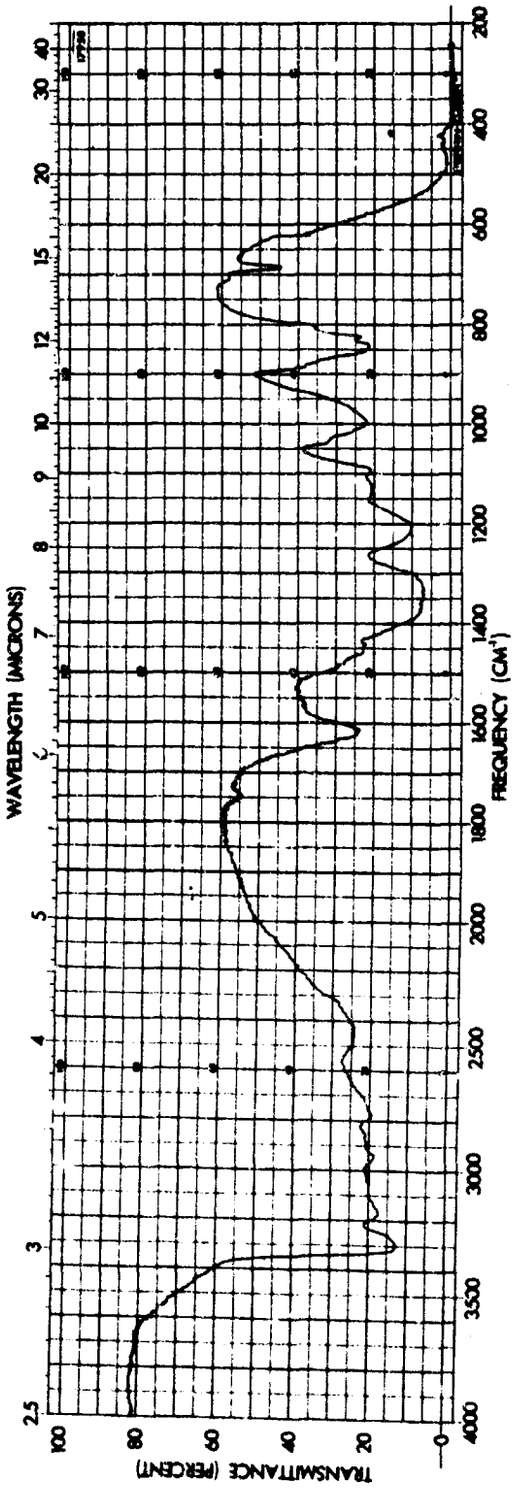

Figure 23. IR Spectrum of Fresh Sample of N_2O_4/MMH Reaction Intermediate (Initial Reactant O/F = 5.0 by wt.).

A summary of the results of the chemical analyses, which were performed within two days of sample production, is given in Table IX. For the elemental analyses, the percentages of carbon, hydrogen and nitrogen were determined; the values given are averages of two determinations. The balance of the sample is assumed to be oxygen.

As given in the table, the specie analyses account for 64.1% of the sample. However, it is reasonable to assume that the measured N-N exists as MMH, NH_3 as CH_3NH_2 and NO_3^- as HNO_3. Adjusted to reflect these compounds, the specie analyses then account for 85.6% by wt., as given in Table X. Approximately 15% of the sample is therefore unaccounted. No nitrite (NO_2^-) and no CO_2 were detected in the freshly prepared sample.

The water content of the sample (Tables IX and X) was determined by gas chromatographic analysis. It was noted during this analysis that the sample also contained free MMH. The amount of the latter, however, was not determined quantitatively.

Two long term pumping experiments were performed on samples of the fresh material. The samples were maintained at room temperature and any volatiles removed during pumping were trapped at liquid nitrogen temperature.

In one experiment, the sample was pumped on for 40 working hours at a pressure of 2 mmHg. The loss in weight of the sample was 0.238 gr, or 2.51% of the initial weight. IR analysis of the collected liquid condensate indicated pure MMH.

Analysis of the residue after pumping gave: C, 16.53% by wt.; H, 9.13%; and N, 40.64%. IR indicated that the residue was similar to the original material but with less free MMH. Gas chromatographic analysis of the residue indicated no significant change in H_2O content from the original material.

A second sample of the reaction intermediate was pumped on for 24 working hours at a pressure of 0.1 mmHg. The condensate and residue were examined by IR (Fig. 24). The condensate was found to be predominantly MMH but with some nitrate present as indicated by NO_3^- absorption at 1350 cm^{-1}. The spectrum of the residue is similar to that obtained from the previous pumping experiment.

TABLE IX

SUMMARY OF CHEMICAL ANALYSES OF REACTION INTERMEDIATE OF N_2O_4/MMH (O/F = 5.0 by wt)*

Elemental Analyses (duplicates):

C	16.30 ± 0.09% by wt.
H	8.60 ± 0.10%
N	42.79 ± 0.95%
O (by difference)	32.31%
Total	100.0% by wt.

Specie Analyses

Total N-N bond functionality (duplicate)	32.75 ± 0.04% by wt.
Total Ammoniacal functionality (NH_3) (duplicate)	0.24 ± 0.02%
NO_3^- (duplicate)	15.81 ± 0.18%
NO_2^-	none detected
CO_2	none detected
H_2O (by gas chromatography)	15.3%
Total	64.10% by wt.

*All analyses performed within two days of production of sample.

TABLE X

ADJUSTED SPECIE ANALYSES OF N_2O_4/MMH REACTION INTERMEDIATE

Total N-N bond functionality as MMH	53.81% by wt.
Total ammoniacal functionality as $CH_3 NH_2$	0.44%
NO_3^- as HNO_3	16.08%
H_2O	15.3 %
CO_2	none detected
NO_2^-	none detected
Total:	85.63% by wt.

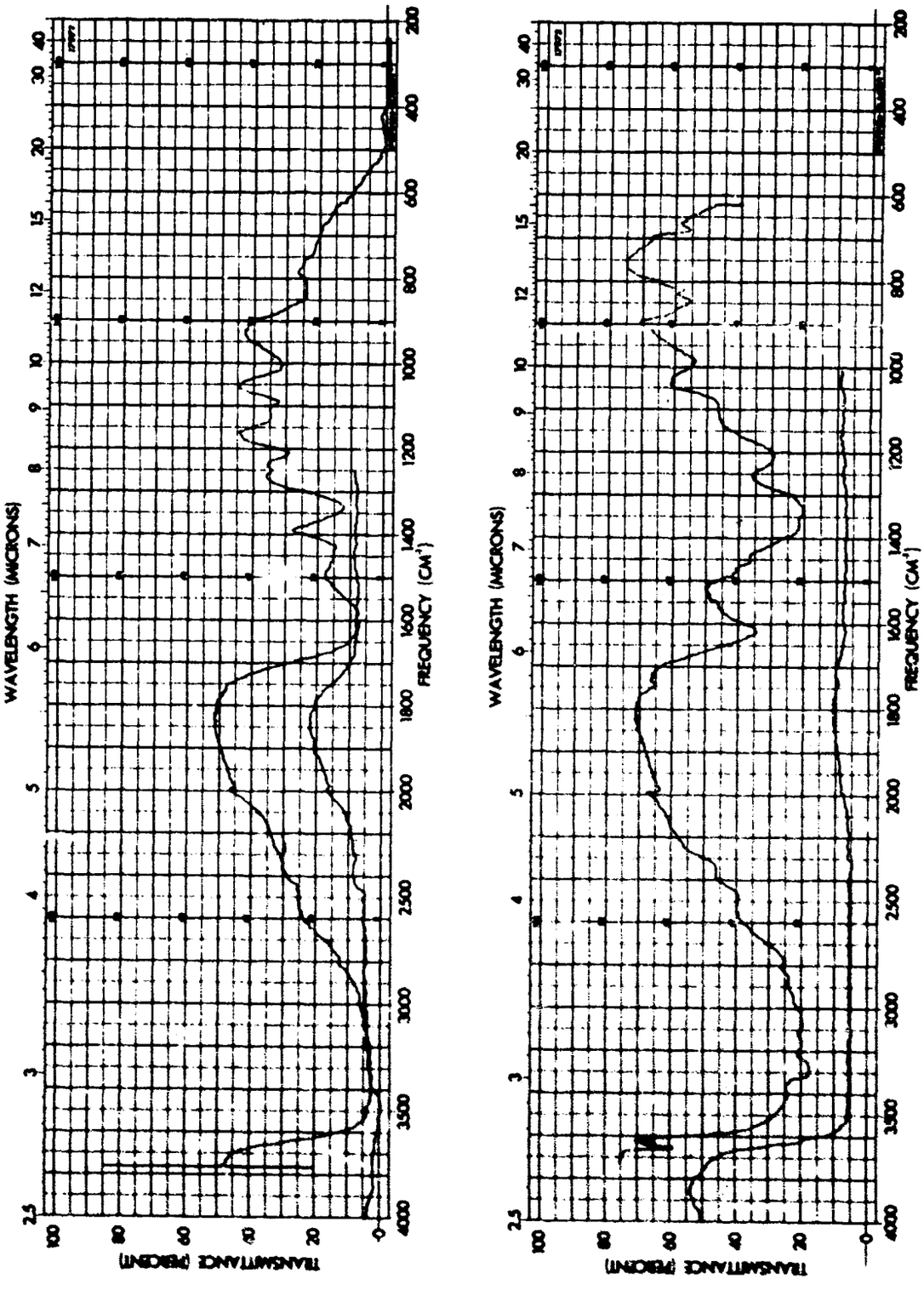

Figure 24. IR Spectra of Condensate (top) and Residue (bottom) of Low Pressure Fractionation of N_2O_4/MMH Reaction Intermediate.

Attempts were made to remove water from a sample of the original material by drying with molecular sieves (Type 4A). Apparently, the water is tied up strongly, for it was not removed by this method.

2. Comparison of Measured and Computed Elemental Analyses

To gain insight into the 15% of the reaction intermediate unaccounted for by the specie analyses, an elemental analysis was computed from the specie analyses given in Table X. The computed elemental analysis is compared to the measured analysis in Table XI. The table indicates that the various specie analyses do not account for significant amounts (>10%) of carbon, nitrogen and oxygen. Other species to account for the discrepancies have not been identified to date.

3. Possible Composition Derived from Specie Analyses

A possible composition of the reaction intermediate can be deduced from the specie analyses as follows. First, it is assumed that all of the CH_3NH_2 (Table X) exists in the reaction intermediate as $CH_3NH_3NO_3$. Next, the balance of HNO_3 is assumed to exist as $MMH \cdot HNO_3$. Finally, all of the H_2O exists as $MMH \cdot H_2O$. The derived composition of the intermediate is given in Table XII. The derived composition accounts for only as much of the reaction intermediate as do the specie analyses, which, as stated, are the basis of the derived composition. However, despite the still unaccounted 15%, the composition given in Table XII indicates a small but significant amount (3.2%) of free MMH. In corroboration, the IR spectrum of the original material indicates free MMH as a constituent and free MMH was also indicated by the gas chromatographic analysis. Furthermore, in one of the long term pumping experiments (Sec. IV. D. 1), the condensed volatiles were found to be pure MMH and the loss in weight of the original material amounted to 2.5%, a figure which compares favorably with the amount of free MMH in the derived composition (Table XII).

TABLE XI

COMPARISON OF MEASURED ELEMENTAL ANALYSIS WITH ELEMENTAL ANALYSIS COMPUTED FROM ADJUSTED SPECIE ANALYSES

Element	Measured Elemental Analysis by wt.	Computed Elemental Analysis ** by wt.	(Comp. -Meas.)100 / Meas.
C	16.30%	14.21%	-12.8%
H	8.60%	9.04%	+5.1%
N	42.8 %	36.52%	-14.7%
O	32.3 %*	25.86%	-20.0%
	100.0 %	85.63%	

* Obtained by difference

** Computed from Specie Analyses given in Table X.

TABLE XII

REACTION INTERMEDIATE COMPOSITION DERIVED FROM ADJUSTED SPECIE ANALYSES*

Constituent	Derived Composition of Intermediate by wt.
$CH_3NH_3NO_3$	1.33 %
$MMH \cdot HNO_3$	26.28%
$MMH \cdot H_2O$	54.8 %
Free MMH	3.22 %
Total:	85.63 %

* Table X

Despite the reasonableness of the derived composition with regard to the analytical results, an anomaly persists concerning vapor pressure. The vapor pressures of MMH and $MMH \cdot H_2O$ are very similar, being about 41 mmHg at 70°F. Although the vapor pressures of $MMH \cdot HNO_3$ and $CH_3NH_3NO_3$ are not known, they are expected to be quite low. Assuming that the latter are negligible and that no complicating molecular associations occur among the four compounds, the vapor pressure of the four-component mixture can be loosely estimated by Raoult's Law and is found to be 32 mmHg at 70°F. In the computation which utilizes the derived composition given in Table XII, MMH and $MMH \cdot H_2O$ are treated as a single solvent (after computing their mole fractions) since their vapor pressures are the same.

The very great discrepancy between the estimated vapor pressure of the reaction intermediate and the experimentally determined approximate value of 0.5 mmHg (Sec. IV. C. 2) suggests for one thing that there is considerable molecular association in the mixture. Of course, Raoult's Law assumes equal sizes for all molecules and this condition is clearly not met. However, it is considered unlikely that the size effect alone accounts for the nearly two orders of magnitude encountered here.

Despite the insights gained, the composition of the freshly prepared N_2O_4/MMH reaction intermediate is not yet completely resolved. The specie analyses suggest that the material is a mixture of four compounds: $MMH \cdot H_2O$, $MMH \cdot HNO_3$, free MMH and $CH_3NH_3NO_3$. In corroboration of this, the existence of free MMH has been independently substantiated by instrumental analyses (IR and GC) and by fractionation experiments.

The four compounds, however, account for only 85% of the reaction intermediate. The balance of the material is as yet unidentified, although the elemental and specie analyses indicate that it contains about 14% by wt. C, 43% N and 43% O. This gives an overall empirical formula for the unidentified 15% of approximately $C_4N_{10}O_9$.

It is apparent at this point that the composition of the freshly-produced reaction intermediate is complex. The situation is further complicated, however, by the dependence of composition of the reaction intermediate on mixture ratio of the initial reactants, N_2O_4 and MMH. This conclusion is reached, as will be discussed, based on the results of analyses which follow in the next sub-section.

4. Gradual Decomposition Effects and Composition Dependency Upon Initial Reactant Mixture Ratio

The chemical analyses performed initially in the program spanned a several week period following production of the samples. Because of gradual sample decomposition, which was subsequently learned, the results of the initial analyses do not describe the composition of freshly prepared material.

The chemical analyses discussed in the preceding sections were made within two days of sample production; the ones to be discussed in this section are the initial analyses made on "old" samples. These analyses are of interest for two reasons. First, a comparison of the results that follow with those given above gives some insight into the effects of the gradual decomposition of the material. Secondly, since the initial analyses were performed on two samples made from two different mixture ratios of N_2O_4/MMH, the degree of constancy of composition of the reaction intermediate with initial reactant mixture ratio can be ascertained.

The results of the analyses of both samples are summarized in Table XIII. In the specie analyses, the total N-N bond functionality, ammoniacal functionality and NO_3^- are given in terms of MMH, CH_3NH_2 and HNO_3 respectively, as in Table X for the fresh sample analyses.

The most striking difference between Tables XIII and X concerns CO_2: none was detected in the fresh sample whereas significant amounts were found in the degraded samples.

It is most probable that the CO_2 in the degraded samples exists as methylhydrazinium-N-methylcarbazate, $CH_3N_2H_2COON_2H_4CH_3$. Other constituents and their concentrations in the two reaction intermediates can then be deduced as follows: The CH_3NH_2 (Table XIII) is assumed to exist in the degraded samples (as well as in the fresh sample, Sec. IV. D. 3 above) as $CH_3NH_3NO_3$. Then, the balance of the HNO_3 is assumed to exist as $CH_3N_2H_3 \cdot HNO_3$. Finally, the remainder of the MMH, after allowing for that in the CO_2 containing compound above, exists as $CH_3N_2H_3 \cdot 2H_2O$.

The test as to the adequacy of this model for the compositions of the degraded reaction intermediates lies in whether the "remaining MMH" in the di-hydrated state satisfactorily completes the material balances between the derived compositions and the specie analyses. As shown in Table XIV, the agreement is very good. The derived compositions, which consist of the same four compounds for each degraded reaction intermediate, are well within experimental error of the specie analyses. It is to be noted that the amount of H_2O obtained by the specie analyses is just sufficient for the "remaining MMH" to exist as $MMH \cdot 2H_2O$. That is, the ratio of H_2O to "remaining MMH" is the same for both samples despite significant differences in constituent concentrations (Table XIV).

Although good accountability of the results of the specie analyses is achieved by the four-component model of intermediate composition, there remains an unidentified 7-8% portion of the degraded samples. By comparison, the specie analyses of the fresh sample leave an unidentified 15% (Table X). Nevertheless, because of the consistency of the derived-though-incomplete analyses of the degraded samples and the independent, experimental corroboration of one constituent in the fresh sample, it seems reasonable that the unidentified portion of each sample is a fifth (and sixth?) constituent and will not nullify the constituent compounds deduced above.

TABLE XIII

RESULTS OF CHEMICAL ANALYSES OF DEGRADED SAMPLES OF N_2O_4/MMH REACTION INTERMEDIATES

	Sample A (N_2O_4/MMH = 2.5)	Sample B (N_2O_4/MMH = 5.0)
Elemental Analyses:		
C	17.4% by wt.	15.5% by wt.
H	9.4%	8.5%
N	32.6%	30.7%
O (by difference)	40.6%	45.3%
Total	100.0%	100.0%
Specie Analyses:		
Total N-N bond functionality (computed in terms of MMH)	50.1% by wt.	49.7% by wt.
NO_3^- (computed in terms of HNO_3)	12.5%	12.4%
NO_2^-	none detected	none detected
Total ammoniacal functionality (computed in terms of CH_3NH_2)	0.88%	1.00%
CO_2	4.4%	8.4%
H_2O	25% (± 3%)	20% (± 3%)
Total	92.9%	91.5%

TABLE XIV

DERIVED COMPOSITIONS OF DEGRADED SAMPLES OF N_2O_4/MMH REACTION INTERMEDIATES

Constituent	Specie Analyses, wt. % N-N as MMH	Amine as CH_3NH_2	NO_3^- as HNO_3	CO_2	H_2O	Derived Compositions of Reaction Intermediates
SAMPLE A (N_2O_4/MMH = 2.5)						
$CH_3NH_3NO_3$		0.88%	1.78%			2.66%
$MMH \cdot HNO_3$	7.8%		10.7%			18.5%
$CH_3N_2H_2COON_2H_4CH_3$	9.2%			4.4%		13.6%
$MMH \cdot 2H_2O$	33.1%				25.9%	59.0%
Totals	50.1%	0.88%	12.48%	4.4%	25.9%	93.76%
Specie Analyses	50.1%	0.88%	12.5%	4.4%	25%	92.9%
SAMPLE B (N_2O_4/MMH = 5.0)						
$CH_3NH_3NO_3$		1.00%	2.03%			3.03%
$MMH \cdot HNO_3$	7.6%		10.4%			18.0%
$CH_3N_2H_2COON_2H_4CH_3$	17.6%			8.4%		26.0%
$MMH \cdot 2H_2O$	24.5%				19.2%	43.7%
Totals	49.7%	1.00%	12.43%	8.4%	19.2%	90.73%
Specie Analyses	49.7%	1.00%	12.4%	8.4%	20%	91.5%

Although the differences between the results of the elemental analyses of the two degraded samples are small (Table XIII), they are larger than experimental error. If degradation effects are similar in the two samples, then the original compositions of the samples were different. The implication, then, is that the reaction intermediate composition depends upon initial reactant mixture ratio. Furthermore, since the product is apparently a mixture rather than a single compound, it is likely that product composition depends also upon pressure. Consequently, the reaction intermediate formed early in an ignition delay period may be different from the material formed late in the delay period due to both changing reactant mixture ratio and pressure. Then, since shock sensitivity, thermal stability, detonability, etc. depend on composition, ignition pressure spikes are also affected. Further work is therefore required to determine more completely the dependency of product composition on initial reactant mixture ratio and on pressure and to evaluate resulting changes in sensitivity characteristics.

E. Heat of Formation of Reaction Intermediate.

One requirement for incorporating the formation of the reaction intermediate into the fundamental hypergolic ignition delay model is the heat evolved when the material forms. The heat of reaction for formation of the reaction intermediate can be calculated if the heat of formation of the material is known. The heat of formation was therefore determined experimentally.

The material used for the determination was made at low pressure from N_2O_4/MMH at a mixture ratio of 5.0 by wt. The material was taken from the same production batch as the samples used for the chemical analyses reported in Sec. IV. D. 1. The heat of formation determination was also performed within a few days of production of the material.

1. Method of Determination

The determination was made by measuring the heat of combustion of the sample in the presence of pure oxygen. A Parr oxygen-bomb adiabatic calorimeter was used. It was calibrated according to a standard NBS procedure using NBS benzoic acid with a known heat of combustion of 6318 cal/gr.

Six runs were made in determining the heat of combustion of the reaction intermediate. Corrections to the measured heats of combustion were applied for the heat liberated upon ignition of a standard 10 cm length of fuse wire and for nitric acid formed during the combustion. The nitric acid correction was determined by titrating the washings with a prepared

solution of Na_2CO_3 where 1 ml of titrant equalled one calorie. Carbon dioxide liberated during the combustion was determined by a CO_2 train of anhydrone and preweighed ascarite absorption tubes. The results are reported in terms of % C recovered.

2. Experimental Results

The calorimeter constant was found to be 2443 cal/C°.

The experimental data of the six runs for the heat of combustion of the reaction intermediate are given in Table XV. As shown in the table, the average heat of combustion is 3.591 kcal/gr.

From the elemental analysis of the sample (Table IX), an empirical formula for the reaction intermediate is found to be $C_{0.0136}H_{0.0860}N_{0.0306}O_{0.0202}$ for an arbitrary molecular weight of 1 gr. Then, an equation for the combustion reaction of the material in the presence of oxygen is:

$$C_{0.0136}H_{0.0860}N_{0.0306}O_{0.0202}(l)+J\,O_2\,(g) = K\,H_2O\,(l) + L\,CO_2\,(g)+M\,N_2\,(g)$$

for which ΔH_c, the measured heat of combustion, is -3.591 kcal/gr. The coefficients K and L in the equation are found to be, in units of mass, 0.744 gr and 0.598 gr, respectively, for one gram of reaction intermediate.

The heat of formation of the reaction intermediate is then obtained from $\Delta H_c = \Sigma\,\Delta H_{f\,products} - \Delta H_{f\,reactants}$ where ΔH_c = -3.591 kcal/gr and the heat of formation of H_2O (l) and CO_2 (g) are -3.793 kcal/gr and -2.137 kcal/gr, respectively. The heat of formation of the liquid reaction intermediate is therefore -0.509 kcal/gr. A "per unit mass" basis has been used, rather than the conventional "per mole" basis, because the molecular weight of the material is unknown. The latter can be postulated, however, as shown below.

TABLE XV

EXPERIMENTAL DATA ON HEAT OF COMBUSTION OF N_2O_4/MMH (O/F = 5.0) REACTION INTERMEDIATE

Run	Sample Weight gram	% C Recovered as CO_2	Δ H Combustion cal/gr
1	0.4269	---	3686
2	0.7659	---	3672
3	1.0223	15.35	3679
4	1.2139	14.66	3465
5	1.0140	14.87	3606
6	1.0630	14.79	3440
	Average	14.92	3591

3. Heat of Reaction for Formation of Intermediate

For calculating the heat released due to formation of the reaction intermediate during an ignition delay period, the overall stoichiometry of the formation reactions is required. In the absence of additional information, it is necessary to estimate the stoichiometry as follows.

From the elemental analysis of the material (Table IX), an empirical formula is found to be $CH_{6.32}N_{2.25}O_{1.486}$, or very nearly $C_4H_{25}N_9O_6$. Since the hydrogen and carbon must come from MMH, the H-to-C ratio must be 6:1 assuming no gaseous product involving either of these elements is formed. Thus, an empirical formula of $C_4H_{24}N_9O_6$ satisfies the H-to-C ratio and is very close to the empirical formula given by the elemental analysis. The overall stoichiometry for formation of this specie is given by:

$$3\ NO_2(g) + 4\ CH_3N_2H_3\ (g) \rightarrow C_4H_{24}N_9O_6(l) + N_2(g).$$

The heat of this reaction is calculated to be $\Delta H_r = -66.2$ kcal per mole of MMH using the value of the heat of formation of the intermediate determined above and 7.91 kcal/mole and 22.8 kcal/mole for the heats of formation of NO_2 (g) and MMH (g) respectively.

For complete combustion

$$10\ NO_2(g) + 4\ CH_3N_2H_3(g) \rightarrow 4\ CO_2(g) + 12\ H_2O(g) + 9N_2(g)$$

for which the heat of reaction is $\Delta H_r = -310.0$ kcal per mole of MMH. For the stoichiometry given above, the heat released upon formation of the intermediate is 21% of the total heat of complete combustion, on a fuel basis.

F. KINETICS OF FORMATION OF REACTION INTERMEDIATE

Overall formation kinetics are also required for incorporating the reaction intermediate into the fundamental hypergolic ignition delay model. An adiabatic, low pressure, flow tube system was used in which the reactant vapors were greatly diluted with nitrogen. The dilution technique was used in order to provide known gas velocities and stream properties, particularly heat capacity, along the flow tube. The temperature rise due to reaction along the flow tube axis was measured.

1. Experimental Apparatus and Instrumentation

The apparatus consists of propellant vaporizing and flowmetering sections and an instrumented flow tube which exhausts into a low pressure housing. The apparatus is shown photographically in Fig. 25 and schematically in Fig. 26.

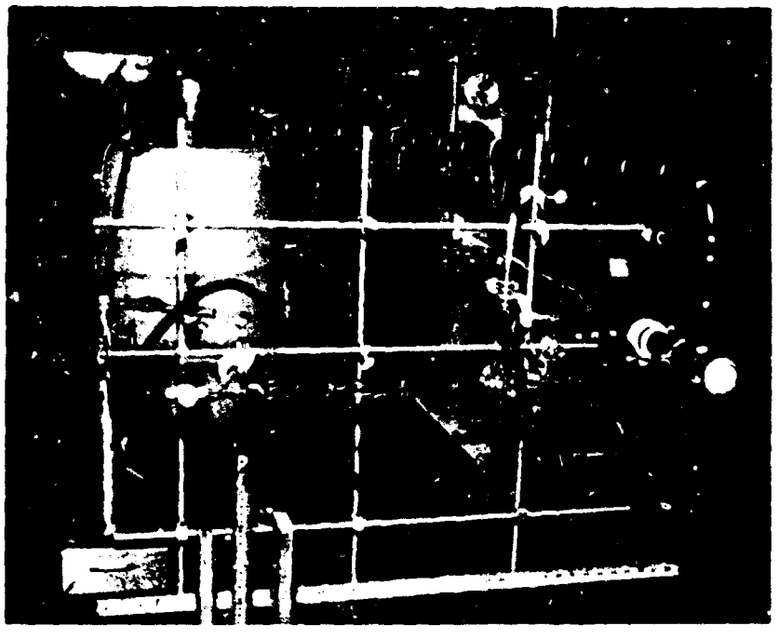

(5809-5)

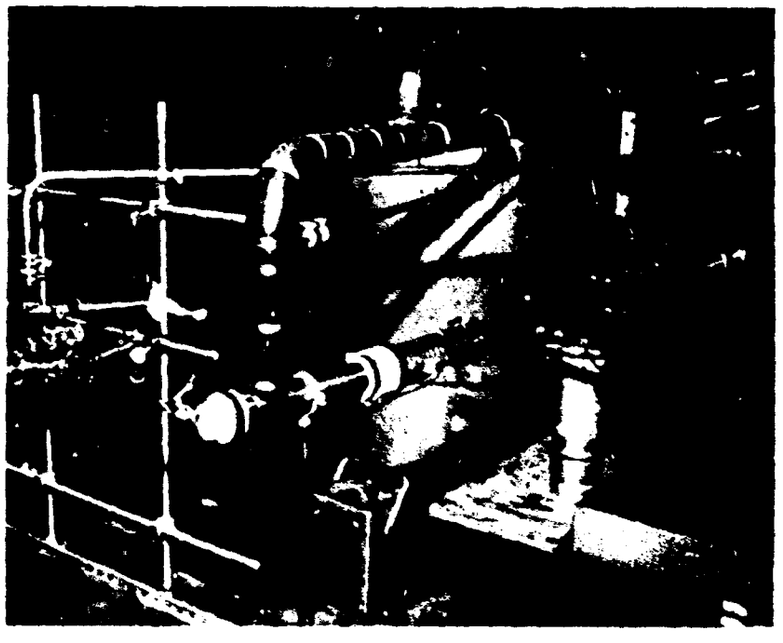

(5809-6)

Figure 25. Apparatus for Study of Formation Kinetics of Reaction Intermediate. Fuel Vaporizing and Flowmetering Sections (top) and Instrumented Flow Tube (bottom).

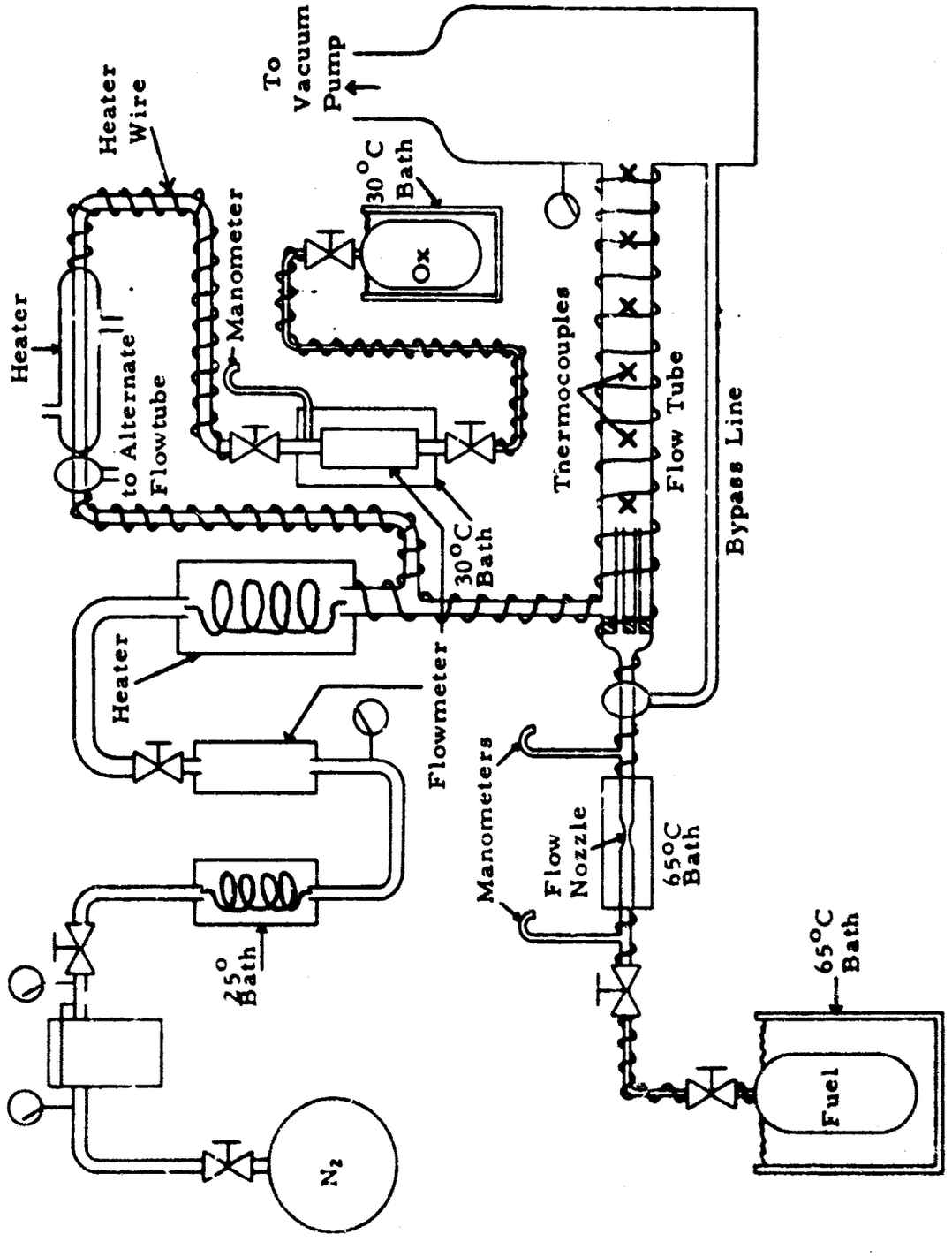

Figure 26. Schematic Diagram of Apparatus for Formation Kinetics Study.

The oxidizer vaporizing and flowmetering section of the apparatus were used for both the kinetics study and the sample production runs. The oxidizer feed system is described in Sec. IV. A. 4. The oxidizer transport line to the flow tube was wire wound to permit preheating of the vapor for runs at elevated initial temperatures. The gaseous oxidizer stream was pre-mixed with the diluent nitrogen stream prior to entering the flow tube.

In a new fuel feed system built for the kinetics study, MMH vapor was taken directly from a 300 cc stainless steel cylinder immersed in a 65°C temperature bath (Fig. 26). For the highest flows, two cylinders connected in parallel were used in the single temperature bath. Steady vapor flows of up to 0. 1 gr/sec could be maintained. The gaseous stream was metered by a calibrated nozzle sized to produce choked flow at the desired flowrates. The pyrex nozzle was jacketed permitting hot water (65°C) to be circulated continuously. Except where jacketed, all fuel feed lines were wrapped with nichrome heating wire (Fig. 25) in order to prevent condensation of the fuel vapors.

Downstream from the metering nozzle, a two-way stopcock directed the fuel stream either to the flow tube or into a line which bypassed the flow tube. The latter was used while setting the desired fuel flowrates (below). When an established fuel flow was shifted to the flow tube, the vapor passed first into a manifold (near-end of flow tube, Fig. 25) which fed eighteen pyrex tubes of 2 mm bore. The tubes distributed the fuel vapors across the inlet of the flow tube (Fig. 27) to promote rapid, complete mixing of the fuel with the premixed nitrogen/oxidizer stream.

Diluent nitrogen gas (Extra Dry Grade, Matheson Co. Inc.) was flowmetered at 9. 8 psig and 25°C in a Fischer-Porter FP-1/2-27-G10/80 flowmeter with an SVT-44 float. After expansion to low pressure, the nitrogen was heated to the desired initial temperature by flowing the gas through copper coils in a large constant temperature water bath.

The pyrex flow tube, 1. 93 in. diameter x 48 in. long, has six fine-wire thermocouples located along the length of the tube with the beads positioned at the tube's centerline. The thermocouples were made from Pt-10% Rh and Pt wires 0. 002 in. in diameter. Uncoated thermocouple beads were used, based on experience gained in the previous program. In that program, temperature measurements were made in undiluted, low pressure streams of N_2O_4/MMH with coated and uncoated

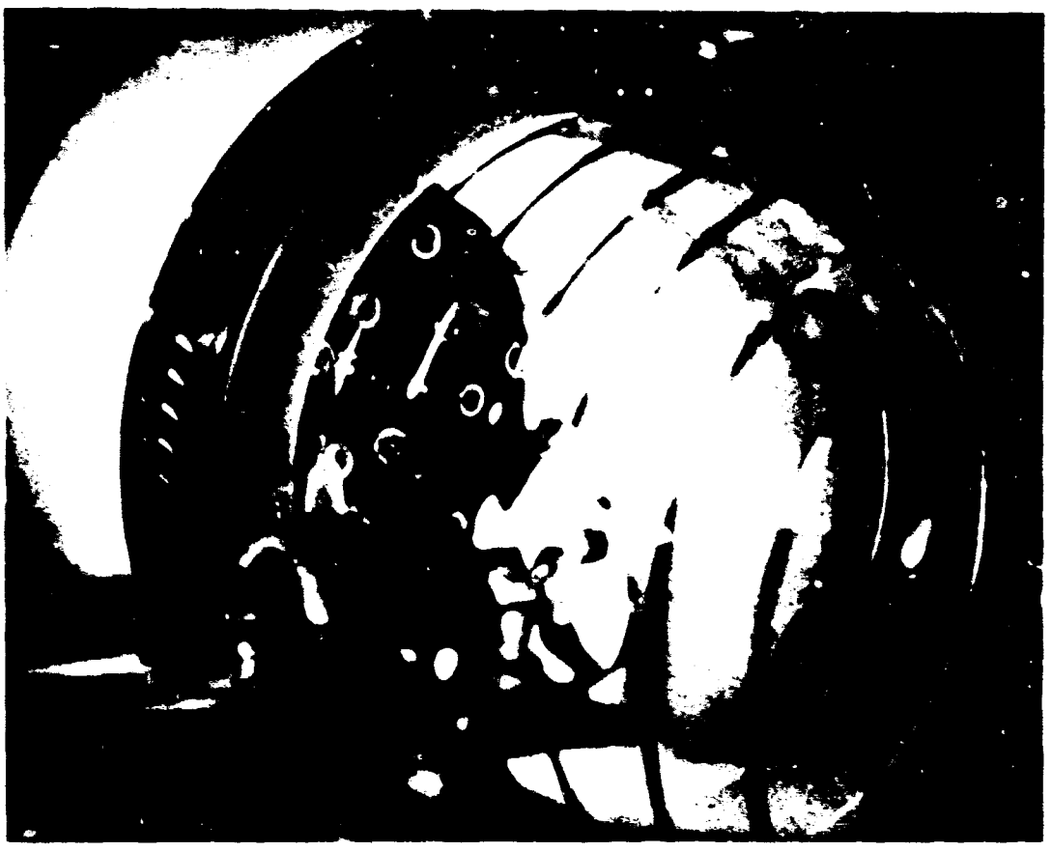

(5809-7)

Figure 27. Fuel Vapor Distribution Tubes at Entrance to Flow Tube

Pt-10% Rh/Pt thermocouples. No catalytic effects were found (1). The cold junctions of the thermocouples in the flow tube were immersed in a single ice bath. The signals of any four of the thermocouples were amplified by CEC DC Amplifiers and recorded simultaneously by a CEC oscillograph. The system provided a sensitivity of 12C° per inch deflection.

The flow tube was wire wound (Fig. 25) and insulated for runs at elevated initial temperatures. The flow tube exhausted into the low pressure housing and vacuum system discussed in Sec. IV. A. 4 (Fig. 25).

A summary of the experimental parameters and their ranges is given in Table XVI.

TABLE XVI

SUMMARY OF EXPERIMENTAL PARAMETERS AND THEIR RANGES IN THE KINETICS STUDY

Total pressure, mmHg	20 - 60
Total flowrate, gr/sec	1.73 - 3.26
Reactants to total flow ratio, wt.	0.05 - 0.13
Reactant mixture ratio, O/F by wt.	0.58 - 5.1
Initial temperature, °C	23 - 75
Flow tube diameter, in.	1.93
Flow tube length, in.	48
Flow velocity, ft/sec	35 - 170
Flow Mach number	less than 0.15
Reynolds number (diameter)	2500 - 4800

Under the conditions of the experiments, the minimum equilibrium percent dissociation of the oxidizer is 95% according to data reported in (11). Because the dissociation and association reactions are extremely fast, the equilibrium mixture is attained prior to oxidizer entry into the flow tube Further dissociation into nitric oxide does not occur at the

temperatures encountered in the experiments (80°C maximum). In view of the above, the oxidizer is taken as being NO_2 only.

The general procedure for making the kinetic measurements at room temperature was as follows. After evacuating the apparatus, the desired nitrogen diluent flow was established. The pressure in the flow tube was then adjusted to the desired level using the throttle valve in the vacuum line downstream from the low pressure housing (Sec. IV.A.4). Then, the signals from the thermocouples were recorded to check for temperature uniformity along the flow tube. Next, the desired oxidizer flow was established and the pressure in the flow tube readjusted if necessary. The temperature profile along the tube was again recorded to check for uniformity. Then, utilizing the bypass line, the desired fuel flow was established. With the fuel flow set and the recorder on, the fuel flow was shifted to the flow tube by quickly rotating the two-way stopcock in the fuel feed system.

From the continuously recorded thermocouple signals, it was found that steady state conditions were attained within a few seconds after shifting the fuel flow into the flow tube. The short time to steady state conditions is due to the low temperature rise (generally 5 to 10C°) from the reactions in the diluted system.

For runs at elevated initial temperatures, the procedure was the same although pre-heating of the flow tube and the three gaseous streams and their lines was of course necessary. Considerable care was required to obtain Variac and heater settings which would provide uniform inlet temperatures for the three streams and also a uriform temperature profile along the tube axis when the diluent and either reactant were flowed.

2. Experimental Results

A total of 68 runs were made in the flow tube apparatus, including the initial check-out tests. The ranges of experimental parameters covered in the tests are given in Table XVI.

The output data was recorded in the form of thermocouple signals versus real time. The thermocouple signals were converted to temperature by manually measuring the deflection of the traces. As a rule, temperature values were obtained from the records when (1) nitrogen alone was flowing, (2) nitrogen plus oxidizer were flowing, and (3) nitrogen plus oxidizer plus fuel were flowing at a point in time following attainment of steady state condition (usually 2 seconds).

For the cases of nitrogen and nitrogen plus oxidizer, temperatures were reduced to check for uniformity of the axial temperature profile without reaction.

From the known flowrates, temperature, pressure and flow tube diameter, gas velocities were computed for each run. Then, using the computed velocities and the known thermocouple positions relative to the final mixing point of the reactants (Fig. 27), the time from mixing to the thermocouple stations was computed. The data is presented below in the form of temperature rise due to reaction versus time from mixing.

Figures 28 and 29 present results of similar runs at room temperature and elevated temperature for two reactant mixture ratios. In terms of complete reaction to CO_2, H_2O and N_2, Fig. 28 is for a fuel-rich mixture and Fig. 29 is for an oxidizer-rich mixture.

The most striking feature of the two figures is the small temperature rise of the high temperature runs as compared to the large temperature rise of the room temperature runs. The significance of this is discussed in detail in the following sub-section, Discussion of Results. In short, the large temperature rise of the room temperature runs includes condensation phenomena which do not occur in the high temperature runs.

It should be noted in the two figures, particularly the high temperature runs, that the temperature rises immediately from the mixing point and that the temperature rise increases linearly with time during most of the staytime of the reactants in the flow tube. The implications of this behavior are three-fold. First, mixing is accomplished very quickly. Second, reaction starts immediately without any induction period. This point is important with regard to the mechanism of reaction as it indicates a pure thermal mechanism, without chain branching. Thirdly, the linear temperature rise indicates that only small amounts of reactants are consumed. The local reactant concentrations, then, are very nearly the initial reactant concentrations. Advantage of this point is taken in interpreting the data in the next section.

In all of the high temperature runs and in some room temperature runs (those at the lower pressures), the temperature rises do not exceed 5C°. Thus, the temperature difference between the gases and the flow tube wall is everywhere small in these cases, making the system very nearly adiabatic. For the room temperature runs at the higher pressures, the excessive temperature rises lead

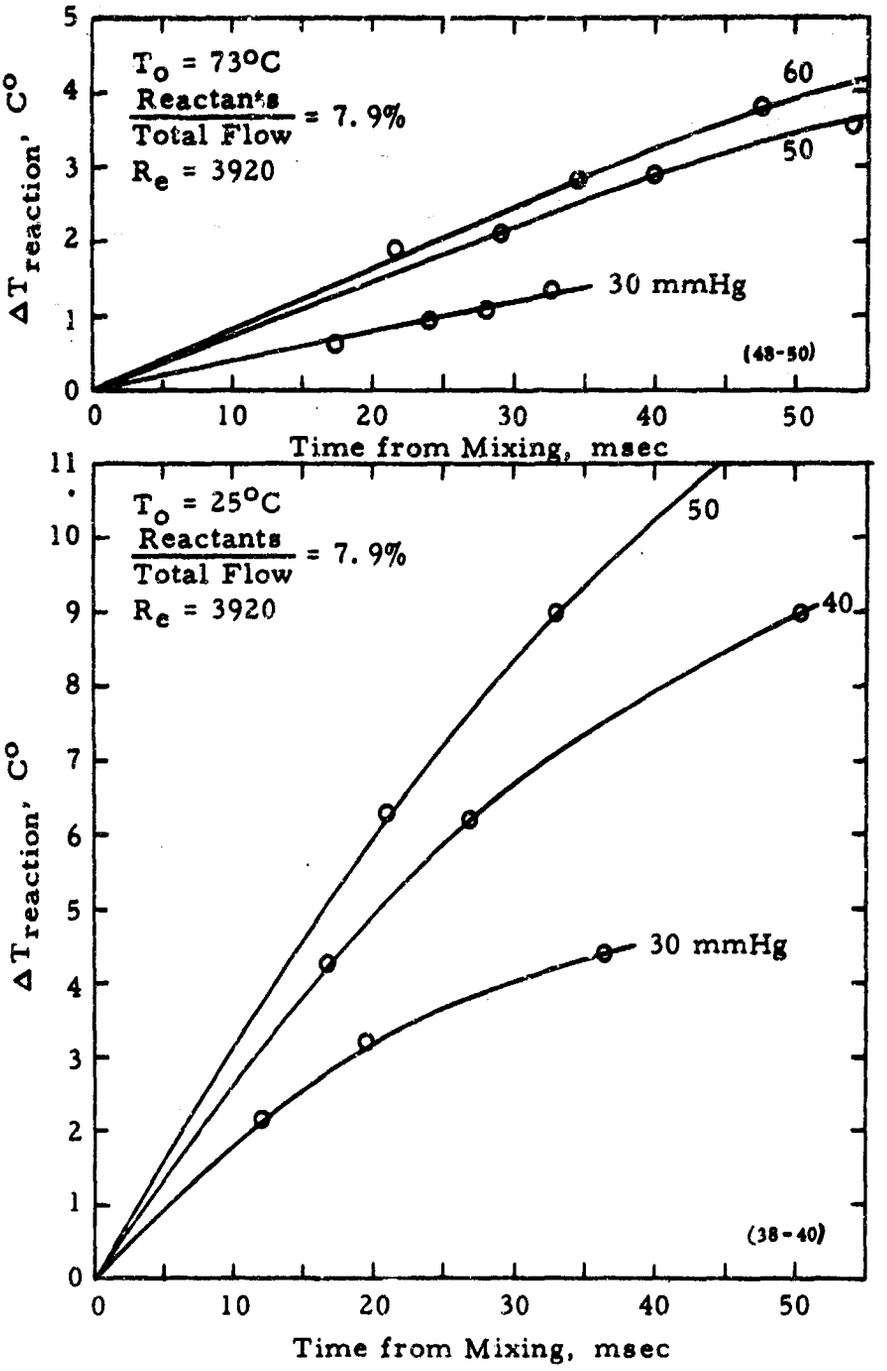

Figure 28. Effect of Pressure and Initial Temperature on Temperature Rise due to Reaction of NO_2/MMH (O/F = 1.2) in Flow Tube with Diluent Nitrogen.

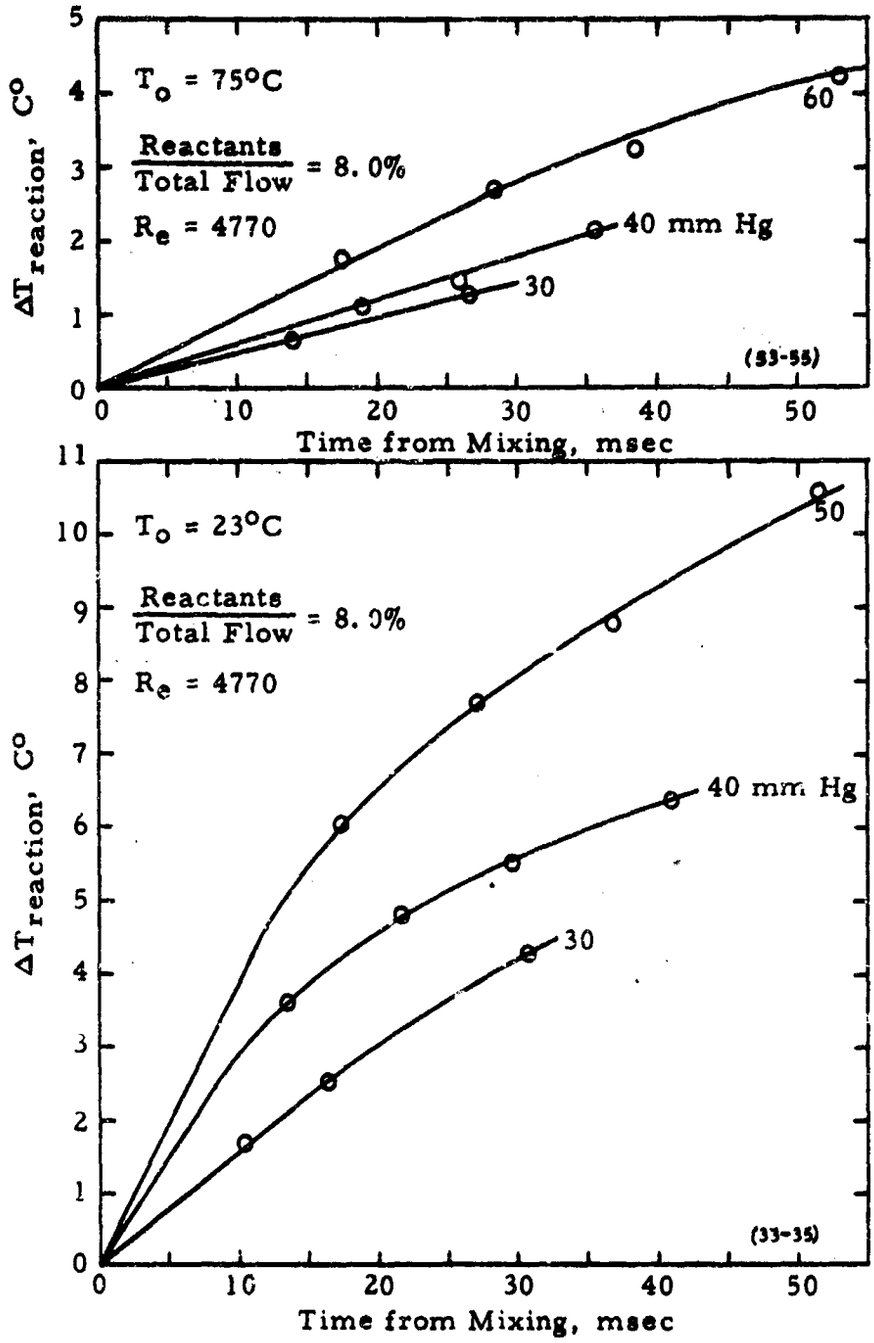

Figure 29. Effect of Pressure and Initial Temperature on Temperature Rise due to Reaction of NO_2/MMH (O/F = 3.5) in Flow Tube with Diluent Nitrogen.

to non-adiabaticity which tends to cause a downward bending of the Δ T-time curves.

The results of room temperature runs at four reactant mixture ratios are given in Figs. 30 through 33. The concentration of the reactant not in excess (in terms of complete combustion) is constant for all runs at the same pressure. The interrelationship of the reactant concentrations in these tests is given below, where X is the concentration of the propellant not in excess:

Figure No.	$\left(\frac{NO_2}{MMH}\right)_{wt.}$	Concentration	
		MMH	NO_2
30	0.58	1.7 X	X
31	1.0	X	X
32	2.5	X	2.5 X
33	3.5	X	3.5 X

3. Discussion of Results

A comparison of the runs at elevated initial temperatures with similar runs at room temperature (Figs. 28 and 29) suggests on the surface a negative temperature coefficient. This is not the case, however, since an additional process was operative in the low temperature runs only. Visual observations of the flow tube revealed that condensation occurred in the room temperature runs but not in the runs at elevated initial temperature. Condensation, when it occurred, was readily apparent as the flow tube became quickly clouded. This was the case in all room temperature runs but in none of the elevated initial temperature runs. The temperature rise of the lower temperature runs includes, then, the heat of condensation of the reaction intermediate.

Considering first the runs at elevated initial temperatures where condensation effects are absent, the overall order of reaction for formation of vapor phase reaction intermediate can be determined from the effect of pressure on temperature rise due to reaction.

For a volume element of reactants in an adiabatic system, the heat equation is:

$$\bar{\rho} \bar{c}_p \frac{dT}{dt} = QW \qquad (25)$$

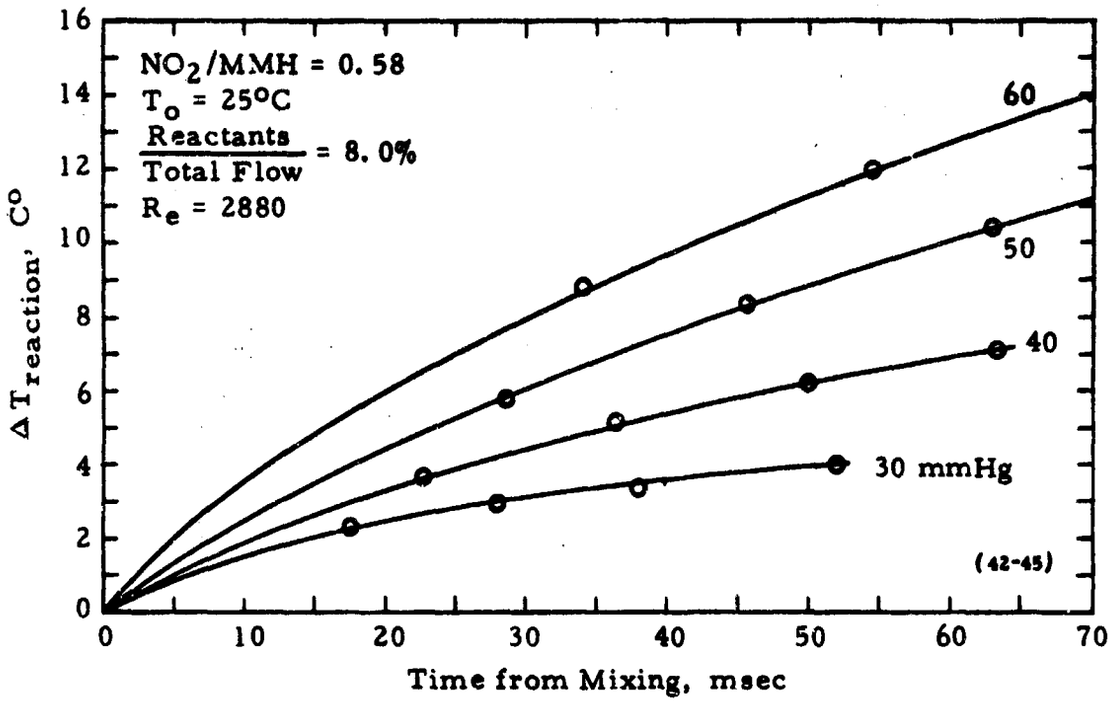

Figure 30. Effect of Pressure on Temperature Rise due to Reaction of NO_2/MMH (O/F = 0.58) in Flow Tube with Diluent Nitrogen.

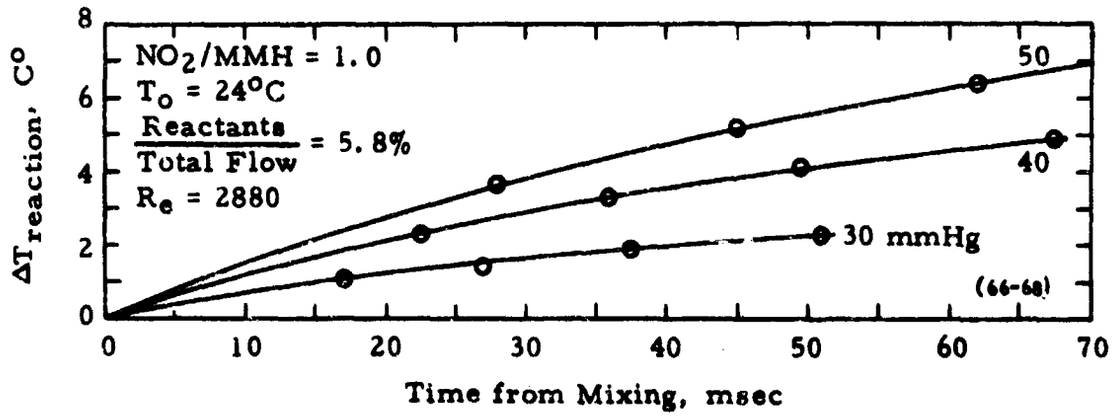

Figure 31. Effect of Pressure on Temperature Rise due to Reaction of NO_2/MMH (O/F = 1.0) in Flow Tube with Diluent Nitrogen.

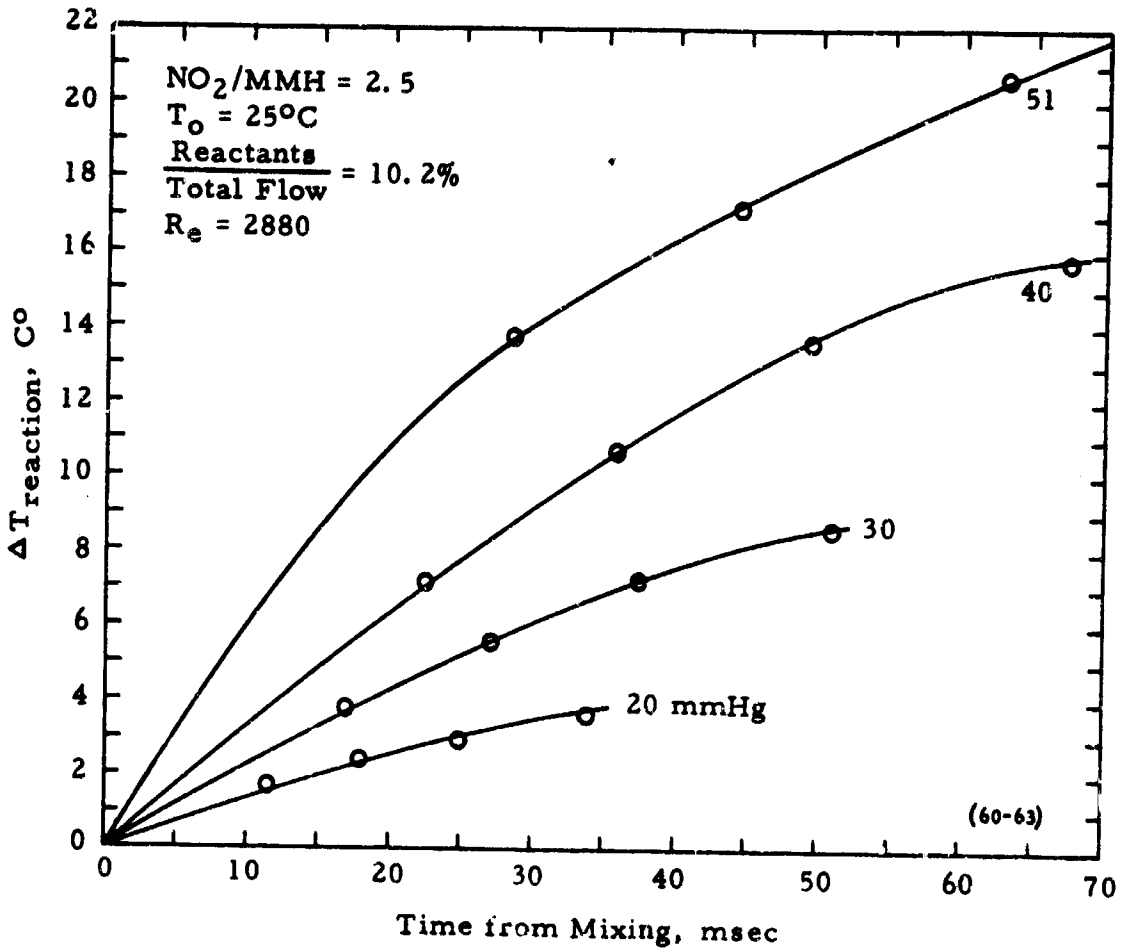

Figure 32. Effect of Pressure on Temperature Rise due to Reaction of NO_2/MMH (O/F = 2.5) in Flow Tube with Diluent Nitrogen.

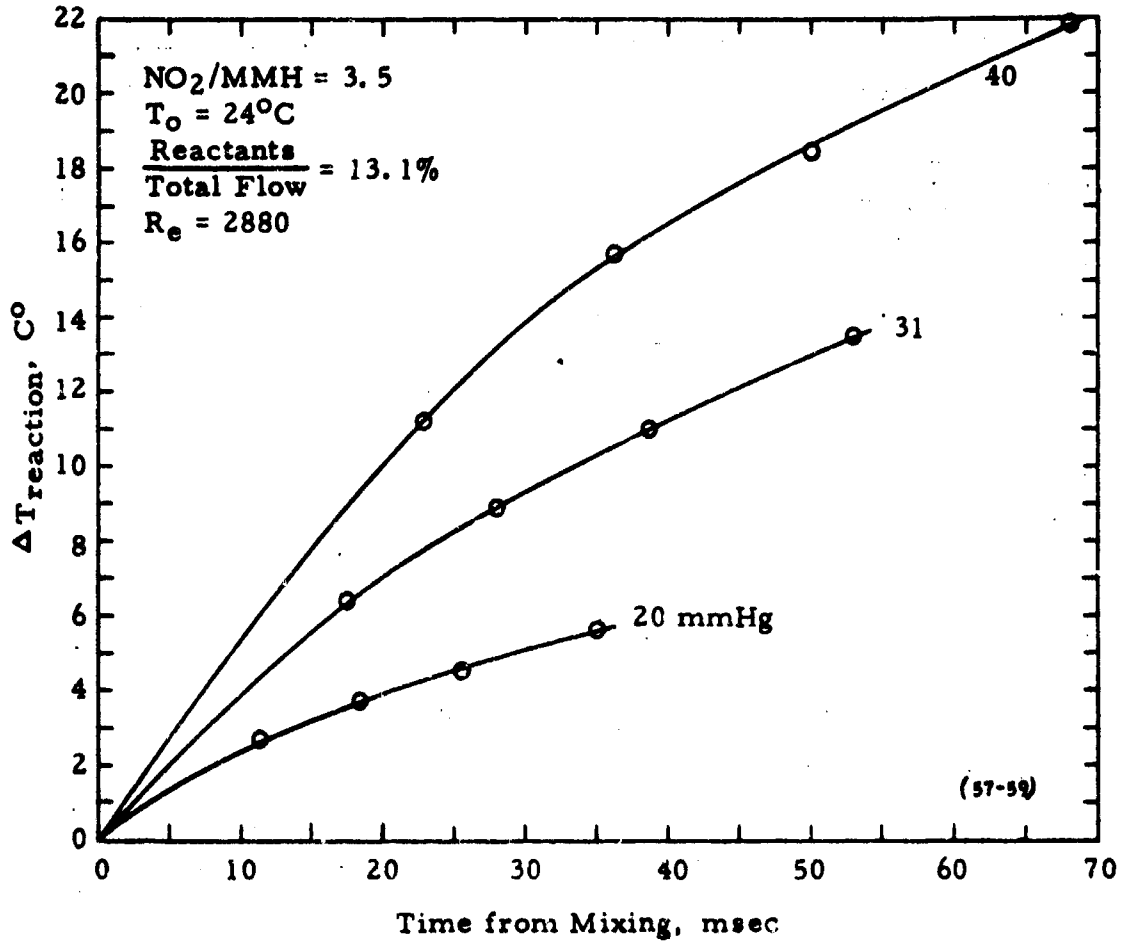

Figure 33. Effect of Pressure on Temperature Rise due to Reaction of NO_2/MMH (O/F = 3.5) in Flow Tube with Diluent Nitrogen.

For a perfect gas, Eq. 25 may be written

$$\frac{P\bar{M}\bar{c}_p}{RT}\frac{dT}{dt} = QW \tag{26}$$

For a first order reaction, Eq. 26 becomes

$$\frac{P\bar{M}\bar{c}_p}{RT}\frac{dT}{dt} = k_1 c_1 Q \tag{27}$$

and for a second order reaction, Eq. 26 becomes

$$\frac{P\bar{M}\bar{c}_p}{RT}\frac{dT}{dt} = k_2 c_1 c_2 Q \tag{28}$$

Since consumption of the reactants is very small as discussed in the preceding section, the concentrations of reactants can be considered constant. Then, expressing concentrations in terms of initial pressure, temperature and mole fractions, Eq. 27 for a first order reaction becomes:

$$\frac{dT}{T} = \frac{Qk_1 x_1}{\bar{M}\bar{c}_p T_o}\,dt \tag{29}$$

where x_1 is the mole fraction of specie 1 and P is the initial pressure which remains constant in the run. Equation 29 can be readily integrated if k_1, the first order rate constant, can be considered constant. By definition, $k = A\exp\left(-\frac{E}{RT}\right)$. The pre-exponential factor A is considered a constant.* For the high temperature runs now under consideration, T varies by no more than 5 C^o during the runs (Figs. 28 and 29). Also, a low activation energy E is indicated by the fact that the reaction proceeds, and rather rapidly, at room temperature. Under these conditions of a small temperature change and a low activation energy, say 4.5 kcal/mole which is close to the activation energy (5.2 kcal/mole) of gas phase ignition reactions of NO_2/MMH(1), the rate constant k varies by less than 10%.

- -

* Strictly speaking A is only constant in the case of a reaction of the first order. When the order of reaction is greater than one, A is a weak function of temperature.

Taking k as constant and noting that $T = T_o$ when $t = 0$, Eq. 29 can be integrated, giving:

$$\ln \frac{T}{T_o} = \frac{Qk_1x_1}{M\bar{c}_pT_o} t \tag{30}$$

Expanding $\ln(T/T_o)$ and neglecting terms other than the first since T/T_o is close to unity, Eq. 30 becomes:

$$T-T_o = \Delta T_{reaction} = \frac{Qk_1x_1}{M\bar{c}_p} t \tag{31}$$

It is seen therefore that, in the case of a first order reaction, the temperature rise as a function of time is independent of pressure. Since the high temperature runs of Figs. 28 and 29 indicate a significant effect of pressure, it is concluded that the overall order of reaction for formation of vapor-phase reaction intermediate is not one.

Again expressing concentrations in terms of initial pressure, temperature and mole fractions, Eq. 28 for a second order reaction becomes:

$$\frac{dT}{T} = \frac{Qk_2x_1x_2}{M\bar{c}_pRT_o^2} Pdt \tag{32}$$

Equation 32 can also be integrated under the above conditions giving, after expansion:

$$T-T_o = \Delta T_{reaction} = \frac{Qk_2x_1x_2}{M\bar{c}_pRT_o} Pt \tag{33}$$

In this case, for a second order reaction, the temperature rise depends directly on pressure. Also, the second order rate constant k_2 can in principle be calculated from the slope of the ΔT-t curves if the heat of reaction Q is known for the vapor-phase formation of the reaction intermediate.

Analogously, it can be shown that for a third order reaction, the temperature rise under the above conditions depends on the square of pressure.

As a consequence of the above, the present experimental system provides a rather sensitive method for determining the overall order of reaction if condensation effects are absent. The latter condition was found to be met only in the runs at elevated initial temperature. From these runs, it is found that, since the temperature rise increases directly with

pressure, the reactions for formation of gas-phase reaction intermediate have an overall order of approximately two. As stated above, in principle the second order rate constant can be calculated. However, in the present case, the required value of Q for the gas phase reaction, without condensation, is unknown.

Activation energy is conventionally determined from measurements at various initial temperatures. The same reactions must of course occur at the various temperature levels. In the present case, an additional process, namely condensation, occurred in the room temperature runs only. Since the condensation effects cannot be adequately separated in the present limited data, activation energy cannot be extracted.

G. EFFECTS OF FORMATION OF REACTION INTERMEDIATE ON PRE-IGNITION CHAMBER PRESSURIZATION

Formation of the reaction intermediate during an ignition delay period affects ignition delay time in two principal ways. Formation of the intermediate liberates heat which tends to increase the rate of pre-ignition pressure rise and to shorten the ignition delay time. Also, formation of the intermediate consumes reactants. If the reactants are vapors, which is taken to be the case here, then pre-ignition chamber pressure tends to rise more slowly and the ignition delay time tends to increase. Thus the two effects are in opposition, the heat evolved tending to increase pre-ignition pressure rise and the vapor mass consumed tending to slow pre-ignition pressure rise. Figures 11 and 12 indicate that the dominant effect is that of heat evolution. However, both effects are analytically treated.

1. Mass Sink

Because of its low vapor pressure (less than 1 mmHg) at the temperatures encountered during an ignition delay period (Sec. III. D), the reaction intermediate is treated as existing wholly in the condensed phase. That is, the reaction intermediate is treated as forming in the vapor phase from vapor phase reactants but then immediately condensing. The controlling process, then, is formation of vapor phase reaction intermediate. Surface catalyzed reactions on the droplets formed are assumed to be negligible.

For a second order reaction (Sec. IV. F. 3) with partial orders with respect to fuel and oxidizer of unity, the rate equation is

$$-\frac{dc_f}{dt} = W = Ac_f c_{ox} \exp\left(-\frac{E}{Rt}\right) \quad 4)$$

For a small but finite time interval, Δt_N, Eq. 34 becomes

$$-\Delta c_f = Ac_f c_{ox}\ \Delta t_N \exp\left(-\frac{E}{RT}\right) \quad (35)$$

Expressing concentrations in terms of mass of vapor phase reactants in a thrust chamber, m_c, for compatibility with the equations of Sec. III, and relating the amount of fuel consumed to the amount of reaction intermediate formed utilizing the stoichiometry given in Sec. IV. E. 3, Eq. 35 becomes:

$$m_{int} = \frac{A}{V_c}\left(\frac{m_c}{\theta}\right)_f \left(\frac{m_c}{M}\right)_{ox} \Delta t_N \exp\left(-\frac{E}{RT}\right) \quad (36)$$

Equation 36 is used to calculate the mass of reaction intermediate formed in each time interval Δt_N during the ignition delay time calculation.

Since the reaction intermediate is formed from vapor phase reactants, the mass of vapors of each reactant are correspondingly reduced in each time interval. Equation 6, in Sec. III. A., is therefore replaced by

$$(m_c)_N = \frac{V_c M}{R}\left(\frac{P_g}{T_g}\right) - \theta\,(m_{int})_N \quad (37)$$

where θ = 0.571 and 0.429 for fuel and oxidizer, respectively, as given by the stoichiometry of the formation reaction derived in Sec. IV. E. 3.

For the temperature T in Eq. 36, the average temperature of the reactant vapors in each time interval is used:

$$T = T_{g_{av}} = \frac{(m_c c_{pg} T_g)_f + (m_c c_{pg} T_g)_{ox}}{(m_c c_{pg})_f + (m_c c_{pg})_{ox}} \quad (38)$$

T_g for each reactant is obtained from Eq. 7 but modified, as shown below, to reflect warming of the vapors by the heat evolved from formation of the reaction intermediate.

2. Heat Source

Formation of the reaction intermediate evolves heat which raises the temperature and pressure of the reactants in a thrust chamber and thereby tends to decrease the ignition delay time. Since the reaction intermediate is considered to exist in the condensed phase due to its low vapor pressure, the heat evolved is both the heat of reaction for formation of the gas phase reaction intermediate and the heat of condensation combined. The overall reaction is taken to be the one given in Sec. IV. E. 3, namely:

$$3NO_2(g) + 4CH_3N_2H_3(g) \longrightarrow C_4H_{24}N_9O_6(l) + N_2(g)$$

The heat of this reaction was calculated to be $\Delta H_r = -66.2$ kcal per mole of MMH, using the experimentally determined value of the heat of formation of the liquid reaction intermediate (Sec. IV. E. 2).

Neglecting sensible heats, the heat evolved in each time interval due to formation of liquid reaction intermediate, Q_r, is therefore:

$$Q_r = -(m_{int})_N \quad \Delta H_r \tag{39}$$

where ΔH_r is the heat of reaction per unit mass of reaction intermediate, -0.900 kcal/gr, and $(m_{int})N$ is given by Eq. 36.

The heat evolved in each time interval, Q_r, is apportioned to each reactant in relation to their vapor phase masses in the thrust chamber during the interval. The energy which raises the temperature of the oxidizer vapors, for example, is:

$$Q_{r\,ox} = \left(\frac{m_{c\,ox}}{m_{c\,ox} + m_{cf}}\right) Q_r \tag{40}$$

Equation 7 for the temperature of the vapors of one reactant at the end of the N^{th} time interval is modified, giving (for the oxidizer):

$$T_{gN} = \frac{\sum_{j=1}^{N} \sum_{i=1}^{3} G_{ij}(T_{dij})_{N-1} + (T_g)_{N-1}\left[(m_c)_{N-1} - (G_W)_N - (m_{noz})_N\right] + \dfrac{Q_{rox} - Q_N}{c_{pg}}}{\sum_{j=1}^{N} \sum_{i=1}^{3} G_{ij} + (m_c)_{N-1} - (G_W)_N - (m_{noz})_N} \tag{41}$$

The effect on ignition delay time of formation of reaction intermediate is given in Sec. V. which follows.

SECTION V

PHASE III - REFINEMENT AND VERIFICATION OF MATHEMATICAL IGNITION DELAY MODEL

In this section of the report, the total model is descriptively summarized and the general method for obtaining solutions is outlined. Then, computed results are compared to experimental results. Finally, some considerations concerning the role of the reaction intermediate in ignition pressure spikes are given.

A. INCORPORATED REFINEMENTS

In the present program, the hypergolic ignition delay model developed under the preceding program has been refined in three areas. Firstly, the initial build-up of propellant flowrate in a thrust chamber following valve opening has been incorporated into the model in the manner given in Section III. C. Secondly, heat transfer between thrust chamber walls and the vaporizing vapor/drop system has been incorporated as given in Section III. D. These first two refinements affect pre-ignition pressure rise due to vaporization of each propellant independent of the other. The third area concerns reactions between the two propellants to form a reaction intermediate which also affects the pre-ignition pressure rise in a thrust chamber. Formation of the reaction intermediate during an ignition delay period is accounted for in the manner given in Section IV. G.

B. GENERAL METHOD OF SOLUTION

The analytical pressure-time curves given in Sec. III were calculated for the single propellant under consideration using the propellant vaporization model of Sec. III. A., modified as described in Sec. III. C and D. For calculating ignition delays, the vaporization model is used twice, once for each propellant, and the calculations of each are performed simultaneously. That is, the calculations are performed for one time interval for MMH (Δt_N = 50 μ sec) and then for two time intervals for N_2O_4 (Δt_N = 25 μ sec). This pattern is repeated throughout the solution. The shorter time intervals in the case of N_2O_4 are required due to the oxidizer's high volatility.

At the end of each 50 microsecond time interval, the amount of reaction intermediate formed and the heat evolved during that interval are computed. As discussed in Sec. IV. G., the evolved heat is applied to the reactant vapor masses in the chamber. The mass of reactants which are consumed in the formation of the reaction intermediate are also determined and deducted from the vapor masses remaining in the thrust chamber.

Also calculated at the end of each 50 microsecond interval is the fractional degree of ignition which occurred during that interval. The fractional degree of ignition is simply the length of the time interval (50 microseconds) divided by the ignition delay time $(\tau_{ig})_N$ calculated for the conditions of pressure, temperature and composition of the reactant vapors prevailing at that time. The fractional degrees of ignition are summed over succeeding time intervals until the fraction becomes unity, indicating ignition.

The analytical expression used to calculate $(\tau_{ig})_N$ for each time interval is:

$$(\tau_{ig})_N = \frac{R^2 T_{g_{av}}^3}{P_g E_{ign} (AQ)_{ign}} \left(1 + \frac{1}{\beta}\right) (C_{pf} + \beta C_{p_{ox}}) \exp\left(\frac{E_{ign}}{R T_{g_{av}}}\right) \qquad (42)$$

where $P_g = p_f + p_{ox}$, $\beta = p_{ox}/p_f$ and C_{pf} and C_{pox} are molar heat capacities. $T_{g_{av}}$ is obtained by Eq. 38.

Equation 42 is derived in (1) from the heat equation for an adiabatic volume element of vapor phase reactants undergoing thermal bimolecular ignition reactions. The derivation involves the Todes approximation (12) for solution of the differential equation. Although the approximation applies to values of $E_{ign}/RT > 17$, we use the resulting equation 42 in the present case, for which $E_{ign}/RT \simeq 9$, in the absence of a better criterion of ignition.

The values of E_{ign} and $(AQ)_{ign}$ required by Eq. 42 were determined experimentally during the previous program (1). The values appropriate to the present propellant combination are E_{ign} = 5.2 kcal/mole and $(AQ)_{ign} = 3.4 \times 10^{14}$ cal-cc/mole^2-sec.

The fractional degree of ignition for each time interval is simply $\Delta t_N/(\tau_{ig})_N$ where $(\tau_{ig})_N$ is calculated by Eq. 42 at the end of each 50 microsecond interval. The ignition fractions are summed over successive intervals. The ignition delay time in an engine, then, is that time in the computer solution at which $\Sigma\left[\Delta t_N/(\tau_{ig})_N\right]$ becomes unity.

C. COMPUTED RESULTS AND COMPARISONS WITH EXPERIMENTAL RESULTS

1. Ignition Delay Times

Ignition delay times were calculated for N_2O_4/MMH in

space-ambient engines in the manner outlined above. The actual computer program listing is reproduced in Appendix A.

The value of activation energy for formation of reaction intermediate used in the calculations is 4.5 kcal/mole. Although the activation energy could not be determined from the flow tube temperature rise measurements because of condensation effects (Sec. IV. F. 3), the activation energy is known to be low since the reaction intermediate forms at room temperature. Furthermore, since reaction intermediate forms at conditions where ignition does not occur (in the flow tube experiments, for instance), the activation energy of the former must be lower than that of the ignition reactions (5.2 kcal/mole). A value of 4.5 kcal/mole was therefore chosen for E_{int}, the activation energy for formation of the reaction intermediate.

With E_{int} = 4.5 kcal/mole, a series of calculations was run in which A_{int}, the pre-exponential factor of the Arrhenius equation, was varied in order to obtain for Engine Configuration No. 1 the best fit between (1) calculated and experimental pre-ignition chamber pressure-time histories and (2) ignition delay times. As shown in Fig. 34, a good fit was obtained for $A_{int} = 1.7 \times 10^{11}$ cal-cc/mole ^{2}-sec. This value was then used in a computer run for Engine Configuration No. 2 and, again, as shown in Fig. 35, good agreement resulted. The calculated and experimental ignition delay times (from valve signal to ignition) for the two engines are:

	Ignition Delay Time	
	Calculated	Measured
	msec	msec
Engine Configuration No. 1	5.9	5.9
Engine Configuration No. 2	6.55	6.6

The computer input data used in the calculations for Engine Configuration No. 1 are given in Appendix B. The conditions for the corresponding experimental test (Run No. 37) are given in Table IV.

Also plotted in Figs. 34 and 35 are chamber pressurization curves calculated without permitting formation of reaction intermediate during the ignition delay periods, i.e. with $A_{int} = E_{int} = 0$. The

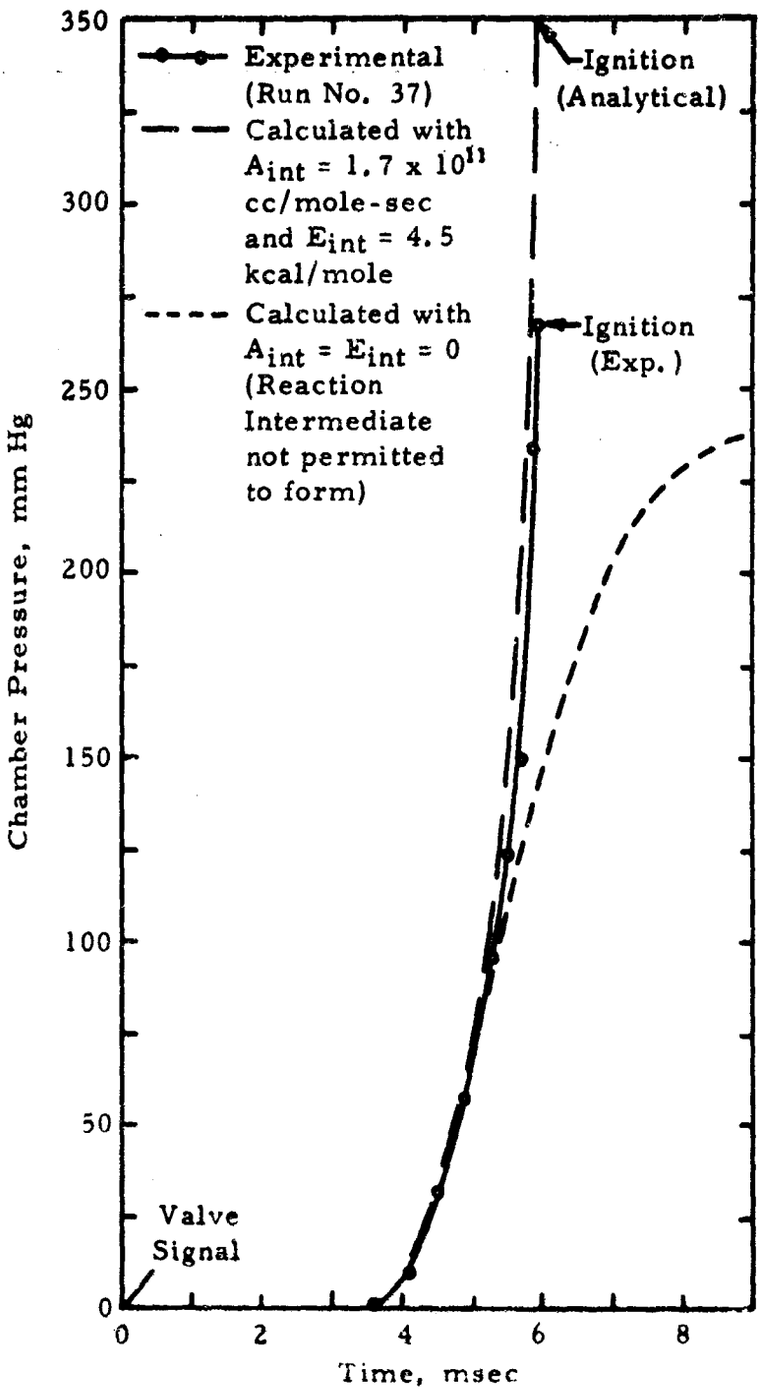

Figure 34. Calculated and Experimental Pre-Ignition Chamber Pressure Histories for N_2O_4/MMH in Engine Configuration No. 1

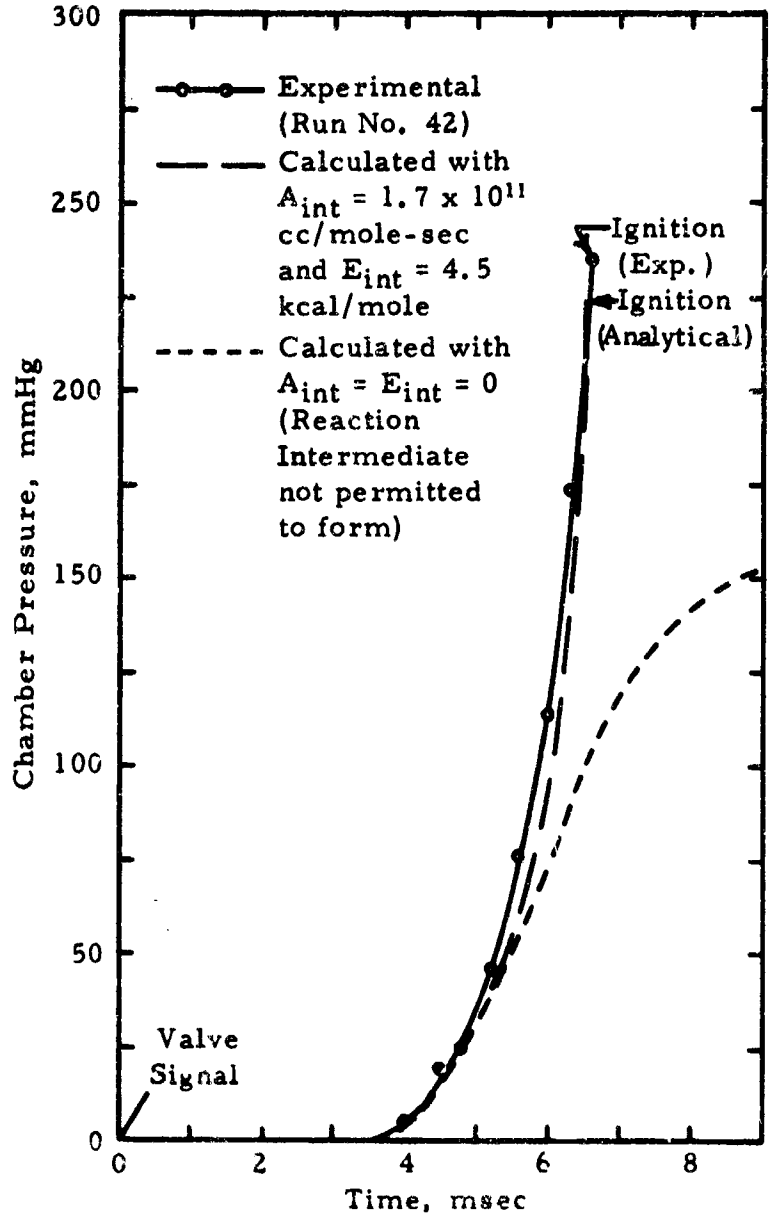

Figure 35. Calculated and Experimental Pre-Ignition Chamber Pressure Histories for N_2O_4/MMH in Engine Configuration No. 2

difference between these curves and the other calculated curves of the figures indicates the significance of formation of the reaction intermediate on ignition delay time. Although formation of the reaction intermediate removes mass from the vapor phase, the heat which is evolved more than compensates for the vapor mass removal and finally results in markedly shorter ignition delay times. In both cases in which $A_{int} = E_{int} = 0$, the calculated ignition delay times were greater than 10 msec.

The heat evolved when the reaction intermediate forms raises the vapor-phase reactant temperatures substantially, as shown in Appendix C, Printout of Computed Results for Engine Configuration No. 1. In the case given in Appendix C, the average gas temperature TGAV reaches 800°F as computed by the present model. Even at temperatures well below this level (i.e. above approximately 150°F), condensation of the reaction intermediate does not occur. Consequently, it is improper to use the heat of reaction for formation of liquid phase reaction intermediate (ΔH_r = -66.2 kcal/mole MMH, Sec. IV.G.2.) throughout the entire ignition delay period. A further consequence of the indicated high temperatures during the latter part of the ignition delay time is that the reaction intermediate which formed in the earlier part of the ignition delay period will decompose, as indicated by the heating curves of Fig. 22, or possibly undergo reaction with the warmed oxidizer present in the chamber. In summary, the good agreement shown in Figs. 34 and 35 between calculated and experimental ignition delays and also pre-igrition chamber pressure histories is misleading. Our understanding of events occurring throughout the entire ignition delay period is not complete and further study of the latter part of the ignition delay time is needed.

2. Fuel Vapor Condensation onto Oxidizer Drops

In accordance with Eq. 4 (in Sec. III.A.), propellant vapor will condense onto a surface if the partial pressure of the propellant vapor exceeds its vapor pressure corresponding to the temperature of the surface. The computer program predicts that many N_2O_4 drops evaporatively cool to a level such that MMH vapor will tend to condense on these cold N_2O_4 drops. Expressed in another way, the partial pressure of MMH vapor exceeds the vapor pressure of MMH corresponding to the temperature of many of the N_2O_4 drops. Thus, MMH vapor will tend to condense onto the colder oxidizer drops. The reverse situation was not found to apply, i.e. the fuel drops do not cool enough to cause condensation thereon of oxidizer vapors.

The computer program as it presently exists does not allow for fuel vapor condensation onto oxidizer drops but the computed results do predict that this phenomenon will tend to occur. A question is therefore raised as to what chemical reaction will occur if fuel vapor does penetrate the evolving oxidizer vapor surrounding the cold N_2O_4 drops. The reaction can lead to formation of additional reaction intermediate or to complete oxidation of the condensed fuel. Studies of the reactions of a fuel droplet (N_2H_4) in an oxidizer atmosphere (NO_2) are presently underway (13); however, the reverse situation of a (cold) oxidizer drop in a fuel vapor atmosphere has not been investigated to the authors' knowledge.

D. IGNITION PRESSURE SPIKING CONSIDERATIONS

Some qualitative insight into the possible role of the reaction intermediate in ignition pressure spiking can be gleaned from the sensitivity tests discussed in Sec. IV.B. To obtain further insight, the energy release upon sudden decomposition of the reaction intermediate has been calculated as well as the energy release upon reaction with additional oxidizer.

Using the empirical formula deduced in Sec. IV.F.3 for the reaction intermediate, an equation for self-decomposition to H_2O, CO_2, N_2 and excess MMH may be written:

$$5\ C_4H_{24}N_9O_6\ (l) \longrightarrow 6\ CO_2(g) + 18\ H_2O(g) + 8\ 1/2\ N_2(g) + 14\ CH_3N_2H_3(g)$$

Using a heat of formation of the reaction intermediate of $\Delta H_f = -0.509$ kcal/gr (Sec. IV.F.2), the heat of reaction for the above decomposition is computed to be $\Delta H_r = -0.365$ kcal/gr of reaction intermediate, indicating a relatively unenergetic reaction.

For reaction with additional oxidizer, the following equation can be written:

$$C_4H_{24}N_9O_6\ (l) + 7NO_2(g) \longrightarrow 4\ CO_2(g) + 12\ H_2O(g) + 8\ N_2(g)$$

The heat of this reaction is computed to be $\Delta H_r = -3.32$ kcal/gr of reaction intermediate which is similar to the heat of combustion of TNT with oxygen (10). Thus, the reaction of the reaction intermediate with additional oxidizer possesses considerable energy but the rate at which the energy is released is not known at present. This parameter is of course all important for ignition pressure spiking and for ZOT's (oxidizer manifold explosions) too.

The total quantity of reaction intermediate formed during the ignition delay period of Engine Configuration No. 1, according to the present computer model, is given in Appendix C under the column labelled TMINT, LB. If this quantity, $2.33 \times 10^{-5} lb_m$, does react with additional oxidizer in accordance with the preceding equation, 2.55×10^{-5} lb_m of oxidizer are required. As given in Appendix C, the amount of oxidizer in the vapor state in the chamber at ignition is $2.84 \times 10^{-5} lb_m$, which exceeds slightly the required amount for complete reaction of all of the reaction intermediate formed. Because the reaction possesses sufficient energy and because sufficient oxidizer is present to permit the reaction to proceed, it is strongly suspected that the reaction intermediate plays a critical role in severe ignition pressure spikes. Further work is required in this area.

SECTION VI

CONCLUSIONS

A workable, fundamental model of hypergolic ignition in space ambient engines has been developed and verified. The computer model satisfactorily predicted the pre-ignition chamber pressure histories and ignition delay times of two different engine configurations.

In developing the model, considerable insight has been gained into the physical and chemical processes operative during the ignition delay time. Both theoretical and experimental evidence has established that a reaction intermediate of N_2O_4/MMH forms during the ignition delay period and markedly affects (shortens) the delay time.

The composition of the N_2O_4/MMH reaction intermediate is very complex. It appears to be a mixture consisting of at least four compounds, the principle ones of which are MMH· H_2O and MMH· HNO_3. The material is more sensitive, both thermally and to impact, than MMH· HNO_3 prepared in the laboratory.

Based on its fuel content, the liquid reaction intermediate still contains approximately 79% of the energy of complete combustion. The reaction of the material with additional oxidizer which is present in a thrust chamber in sufficient amounts at ignition is very energetic, being similar to that of TNT burning with oxygen. By comparison, self-decomposition of the material is relatively unenergetic.

Due to gradual decomposition and its hygroscopic tendency, careful sampling techniques and prompt chemical analyses are required to obtain meaningful composition data.

The computer model predicts that during the ignition delay period MMH vapor tends to condense onto the colder N_2O_4 drops. The kind of reactions which occur (formation of reaction intermediate or complete oxidation) if the fuel vapor does penetrate the evolving vapor from the cold oxidizer drops has not been determined. The model predicts that the reverse situation, condensation of oxidizer vapor onto cold fuel drops, does not occur.

SECTION VII

RECOMMENDATIONS

Several factors pertinent to hypergolic ignition of N_2O_4/hydrazine-type fuels in space-ambient engines that were either outside the scope of the present program or require further study beyond that which was permitted during this six-months effort are enumerated below:

1. Specie analyses of the N_2O_4/MMH reaction intermediate identified approximately 85% of the material. Further work is required not only to identify the remaining 15% but also to eliminate anomalies that exist between the present deduced composition of the material and its measured thermal stability, impact sensitivity and vapor pressure.

2. Because the reaction intermediate is a mixture of compounds, the effects of initial reactant mixture ratio, pressure and temperature on its composition, properties and sensitivity should be investigated.

3. Further work is required to determine formation and condensation rates of the reaction intermediate over the temperature range encountered during ignition delay periods in space-ambient engines. It should be noted that the composition of the reaction intermediate undoubtedly varies from the start of an ignition delay period to ignition.

4. To further define the role of the reaction intermediate in ignition pressure spiking, reaction rates of the reaction intermediate with additional oxidizer need to be determined.

5. To obtain a basis from which to develop preventive/corrective measures to eliminate ZOT's (oxidizer manifold explosions), it is necessary to determine the mechanism by which fuel enters the oxidizer manifold and to determine the state of the fuel (unreacted or partially reacted in the form of reaction intermediate) just prior to entry of the oxidizer.

6. Considerable progress has been made in identifying the N_2O_4/MMH reaction intermediate and in determining its physical and chemical properties. Similar characterizations of the reaction intermediate formed by N_2O_4 with UDMH, N_2H_4 and 50-50 need also be determined.

7. The effects of NO-inhibited N_2O_4 on the formation and properties of the reaction intermediates remain to be determined. It has already been determined that as little as 1% NO in N_2O_4 at least doubles the ignition delay time of N_2O_4/UDMH in an unconfined impinging stream apparatus (2).

8. A mathematical model of ignition pressure spiking during start transients should be developed to permit evaluation of chamber geometry and ignition hydraulics from a pressure spiking viewpoint. The present hypergolic ignition delay model becomes a major part of such a pressure spiking model since the ignition delay model gives the conditions in a thrust chamber at ignition, that is, the conditions from which ignition pressure spikes result.

9. The present hypergolic ignition delay model should be exploited to develop design information by first isolating the main parameters and then determining the rate of change of ignition delay time, mass of intermediate formed, etc. Parameters such as propellant lead and lag, transient flow increase from time zero (feed system/injector effect), initial propellant temperature, initial hardware temperature, etc. can be investigated analytically using the present model to economically assist engine development programs.

APPENDIX A. COMPUTER PROGRAM LISTING

```
C       HYPERGOLIC IGNITION SIMULATION
        DIMENSION R(3,201),TD(3,201),X(3,201)
        DOUBLE PRECISION DELTN,
       1 TGO,WDOT,VC,ASTAR,AC,V,LC,PVW,M,ALPHA,RHOL,LMBDAE,LMBDAS,LMBDAF,
       2 CPL,CPG,TDFP,K,MEWG,KG,D1,D2,D3,D4,D5,D6,D7,D8,D9,D10,D11,
       3 D12,TIME,PG,TG,TEMP,GN,HN,ON,C(3),PV,GAM,Q,Z,OMEGA,SIGMA,
       4 CHI,F,MC,GW,MNOZ,TGPRM,PGPRM,SQRTRE,MINT
        DIMENSION OR(3,401),OTD(3,401),OX(3,401)
        DOUBLE PRECISION ODELTN,
       1 OTGO,OWDOT,OVC,OASTAR,OAC,OV,OLC,OPVW,OM,OALPHA,ORHOL,OLMBDE,
       2 OLMBDS,OLMBDF,OCPL,OCPG,OTDFP,OK,OMEWG,OKG,OD1,OD2,OD3,OD4,OD5,
       3 OD6,OD7,OD8,OD9,OD10,OD11,OD12,OPG,OTG,OTEMP,OGN,OHN,OQN,OPV,
       4 OGAM,OQ,OZ,OOMEGA,OSIGMA,OCHI,OF,OMC,OGW,OMNOZ,OTGPRM,OPGPRM,
       5 OSQRT
  100 FORMAT(10F8.4)
  101 FORMAT(10F8.4/2F16.4)
  102 FORMAT(I5,OPF10.3,F12.3,F14.3,2X,1P4E15.5,0PF8.2,F10.2,F9.4/)
  103 FORMAT(I15,1P3E15.5,3(0PF13.3,2X),1PE15.5)
  104 FORMAT(//1X,'TIG=',F7.4,1X,'MS'/1H1)
  105 FORMAT(1H1,6X,'INPUT DATA'//)
  106 FORMAT(6X,'INITIAL CONDITIONS - FUEL'//)
 1106 FORMAT(/6X,'INITIAL CONDITIONS - OX'//)
  107 FORMAT(6X,'DELTA-T',9X,'TGO',9X,'R(1,1)',8X,'R(2,1)',8X,'R(3,1)',
     1 8X,'TD(1,1)',7X,'TD(2,1)',7X,'TD(3,1)'//)
  108 FORMAT(1P9E14.5)
  109 FORMAT(//6X,'CHAMBER DATA')
  110 FORMAT(//7X,'WDOT',11X,'VC',12X,'A*',12X,'AC',13X,'V',13X,'LC',
     1 12X,'PVW',8X,'SSFLT',9X,'FRCTH')
  111 FORMAT(//6X,'PROPELLANT DATA')
  112 FORMAT(//9X,'M',11X,'ALPHA',9X,'RHOL',8X,'LAMBDA-E',6X,'LAMBDA-S',
     1 6X,'LAMBDA-F',9X,'CPL',11X,'CPG',11X,'TDFP')
  113 FORMAT(//8X,'K',12X,'MEWG',11X,'KG',11X,'D1',12X,
     1 'D2',12X,'D3',12X,'D4',12X,'D5')
  114 FORMAT(///9X,'N',4X,'TIME,MS',5X,'PG,MMHG',5X,'TG,DEG.R',8X,
     1 'MNOZ,LB',8X,'MC,LB',10X,'GN,LB')
  115 FORMAT(///14X,'J',5X,'R(J,1),FT',5X,'R(J,2),FT',6X,'R(J,3),FT',7X,
     1 'TD(J,1)',8X,'TD(J,2)',8X,'TD(J,3)',8X,'X(J,1)'//)
  116 FORMAT(1H1,3X,'N',4X,'TIME,MS',5X,'PG,MMHG',5X,'TG,DEG.R',8X,
     1 'MNOZ,LB',8X,'MC,LB',10X,'GN,LB',8X,'TMINT,LB',3X,'TIGN,MS',
     2 5X,'TGAV,R',3X,'SMIGER'//)
  117 FORMAT(//7X,'D6',12X,'D7',12X,'D8',12X,'D9',12X,'D10',11X,
     1 'D11',11X,'D12',11X,'D13')
  118 FORMAT(//7X,'DIM',9X,'FRCTL',9X,'TDHT')
  119 FORMAT(1E7.2,1X,1E7.2)
  120 FORMAT(1PE9.2,1X,1PE9.2/)
      READ(5,119) AQIGN,AEINT
      WRITE(6,120) AQIGN,AEINT
      READ(5,100) RCAL,THETA,OTHETA,DELHR,EAIGN,EAINT
      WRITE(6,108) RCAL,THETA,OTHETA,DELHR,EAIGN,EAINT
C       READ CHAMBER DATA
    1 READ(5,100) DELTN,TGO,WDOT,VC,ASTAR,AC,V,LC,PVW,SSFLT,FRCTH,
     1 DIM,FRCTL,TDHT
C       READ PROPELLANT DATA
```

```
      READ(5,101) M,ALPHA,RHOL,LMBDAE,LMBDAS,LMBDAF,CPL,CPG,TDFP,K,
     1 MEWG,KG
C     SET INITIAL CONDITIONS
      READ(5,100) (R(J,1),J=1,3),(TD(J,1),J=1,3)
      D1=1546.0
      D2=32.2
      D3=DSQRT(M*D2/(6.2831853*D1))
      D4=ALPHA*AC*DELTN*D3
      D6=DSQRT(K*(2.0/(K+1.0))**((K+1.0)/(K-1.0)))
      D7=ASTAR*DELTN*D6*DSQRT(M*D2/D1)
      D8=VC*M/D1
      D9=2.0*V*M/(MEWG*D1)
      D10=(CPG*MEWG/KG)**(1.0/3.0)
      D11=LC/(V*DELTN)
      D12=2.0*RHOL*CPG/(3.0*KG*DELTN)
      D13=DIW*V/DELTN
C     READ CHAMBER DATA N204
 1001 READ(5,100) ODELTN,OTG0,OWDOT,OVC,OASTAR,OAC,OV,OLC,OPVW,
     1 OSSFLT,OFRCTH,ODIW,OFRCTL,OTDHT
C     READ PROPELLANT DATA N204
      READ(5,101) OM,OALPHA,ORHOL,OLMBDE,OLMBDS,OLMBDF,OCPL,OCPG,OTDFP,
     2 OK,OMEWG,OKG
C     SET INITIAL CONDITIONS N204
      READ(5,100) (OR(J,1),J=1,3),(OTD(J,1),J=1,3)
      OD3=DSQRT(OM*D2/(6.2831853*D1))
      OD4=OALPHA*OAC*ODELTN*OD3
      OD6=DSQRT(OK*(2.0/(OK+1.0))**((OK+1.0)/(OK-1.0)))
      OD7=OASTAR*ODELTN*OD6*DSQRT(OM*D2/D1)
      OD8=OVC*OM/D1
      OD9=2.0*OV*OM/(OMEWG*D1)
      OD10=(OCPG*OMEWG/OKG)**(1.0/3.0)
      OD11=OLC/(OV*ODELTN)
      OD12=2.0*ORHOL*OCPG/(3.0*OKG*ODELTN)
      OD13=OIW*V/ODELTN
      N=1
      NN=1
      TIME=0.0
      PG=0.0
      TG=TG0
      OPG=0.0
      OTG=OTG0
      MINT=0.0
      TMIMI=0.0
      SMIGFR=0.0
      FOR=0.0
      OOR=0.0
      DO 50 I1=1,3
      DO 50 I2=1,201
      OX(I1,I2)=0.0
      OX(I1,I2+201)=0.0
   50 X(I1,I2)=0.0
      C(1)=0.33
      C(2)=0.34
      C(3)=0.33
      WRITE(6,1005)
```

```
      WRITE(6,106)
      WRITE(6,107)
      WRITE(6,108)DELTN,TGO,R(1,1),R(2,1),R(3,1),TD(1,1),TD(2,1),TD(3,1)
      WRITE(6,109)
      WRITE(6,110)
      WRITE(6,108) WDOT,VC,ASTAR,AC,V,LC,PVW,SSFLT,FRCTH
      WRITE(6,118)
      WRITE(6,108) DIW,FRCTL,TDHT
      WRITE(6,111)
      WRITE(6,112)
      WRITE(6,108) M,ALPHA,RHOL,LMBDAE,LMBDAS,LMBDAF,CPL,CPG,TDFP
      WRITE(6,113)
      WRITE(6,108) K,MEWG,KG,D1,D2,D3,D4,D5
      WRITE(6,117)
      WRITE(6,108) D6,D7,D8,D9,D10,D11,D12,D13
      WRITE(6,1106)
      WRITE(6,107)
      WRITE(6,108) ODELTN,OTGO,OR(1,1),OR(2,1),OR(3,1),OTD(1,1),
     1 OTD(2,1),OTD(3,1)
      WRITE(6,109)
      WRITE(6,110)
      WRITE(6,108) OWDOT,OVC,OASTAR,OAC,OV,OLC,OPVW,OSSFLT,OFRCTH
      WRITE(6,118)
      WRITE(6,108) ODIW,OFRCTL,OTDHT
      WRITE(6,111)
      WRITE(6,112)
      WRITE(6,108) OM,OALPHA,ORHOL,OLMBDE,OLMBDS,OLMBDF,OCPL,OCPG,OTDFP
      WRITE(6,113)
      WRITE(6,108) OK,OMEWG,OKG,D1,D2,OD3,OD4,OD5
      WRITE(6,117)
      WRITE(6,108) OD6,OD7,OD8,OD9,OD10,OD11,OD12,OD13
      WRITE(6,116)
    2 GN=0.0
      HN=0.0
      QN=0.0
      J=N+1
  310 IF (J-D11-21) 3,3,55
   55 J=D11+21
    3 J=J-1
      I=0
      D5=WDOT*DELTN
      IF (N-(SSFLT/DELTN+D11)) 300,4,4
  300 IF (J-N+SSFLT/DELTN) 4,4,305
  305 D5=D5*(N-J+0.5)*DELTN/SSFLT
    4 I=I+1
      GAM=K(I,J)
      TEMP=TD(I,J)
      IF (TEMP-TDFP) 60,65,65
   60 TEMP=TDFP
   65 PV=PFUNCT(TEMP)
      Q=0.0
      IF (J-D11) 70,70,5
   70 IF (TEMP-TDFP) 75,75,80
   75 IF (X(I,J)-1.0) 80,5,5
   80 Q=3.0*(PV-PG)*ALPHA*DELTN/(RHOL*GAM)*D3*DSQRT(1.0/TEMP)
```

```
   85 IF (PG) 5,5,90
   90 SQRTRE=DSQRT(D9*GAM*PG/TG)
      Z=D12*GAM**2*Q/(2.C+).6*D1C*SQRTRE)
      IF (Z-30.C) 205,205,200
  200 Z=30.0
  205 OMEGA=CPG*(TG-TEMP)/(DEXP(Z)-1.0)
      SIGMA=OMEGA*D5*C(I)*Q
      QN=QN+SIGMA
    5 R(I,J+1)=GAM*(1.0-Q)**(1.0/3.0)
      TDP(I,J+1)=TEMP-LMBDAE/CPL*Q
      IF (X(I,J)) 210,210,207
  207 TD(I,J+1)=TDFP
      IF (0.60-X(I,J)) 225,225,400
  210 IF (Q) 215,225,215
  215 IF (PG) 225,225,220
  220 TD(I,J+1)=TEMP+Q/CPL*(OMEGA-LMBDAE)
  400 IF (J-D13) 225,401,401
  401 IF (X(I,J)) 405,405,236
  405 IF (N-(D13+TDHT/DELTN)) 410,415,415
  410 FRCT=(FRCTH-FRCTL)*(1-(N-D13)*DELTN/TDHT)+FRCTL
      GO TO 420
  415 FRCT=FRCTL
  420 TD(I,J+1)=TD(I,J+1)+FRCT*(TGC-TD(I,J+1))
  225 CHI=0.0
      IF (TD(I,J+1)-TDFP) 230,230,235
  230 CHI=Q/LMBDAF*(LMBDAS-OMEGA)
  235 X(I,J+1)=X(I,J)+CHI
      IF (X(I,J+1)) 236,237,237
  236 X(I,J+1)=0.0
  237 IF (X(I,J+1)-1.0) 239,239,238
  238 X(I,J+1)=1.0
  239 F=C(I)*D5*Q
      GN=GN+F
      HN=HN+F*TEMP
        (I-3) 4,240,240
      IF (J-1) 245,245,3
  245 MC=D8*PG/TG-THETA*MINT
      GW=0.0
      IF (PG-PVW) 252,252,250
  250 GW=D4*(PG-PVW)/DSQRT(TG)
  252 MNOZ=D7*PG/DSQRT(TG)
      TGPRM=(HN+TG*(MC-GW-MNOZ)+(EQR-QN)/CPG)/(GN+MC-GW-MNOZ)
      PGPRM=TGPRM*((GN-GW-MNOZ)/D8+PG/TG)
 1002 DGN=0.0
      DHN=0.0
      DQN=0.0
      JJ=NN+1
 1310 IF (JJ-DD11-21) 1003,1003,1055
 1055 JJ=DD11+21
 1003 JJ=JJ-1
      II=0
      DD5=DWDGT*DDELTN
      IF (NN-(DSSFLT/DDELTN+DD11)) 1300,1004,1004
 1300 IF (JJ-NN+DSSFLT/DDELTN) 1004,1004,1305
 1305 DD5=DD5*(NN-JJ+0.5)*DDELTN/DSSFLT
```

```
 1004 II=II+1
      OGAM=OR(II,JJ)
      OTEMP=OTD(II,JJ)
      IF (OTEMP-OTDFP) 1060,1065,1065
 1060 OTEMP=OTDFP
 1065 OPV=VAP(OTEMP)
      OQ=0.0
      IF (JJ-DD11) 1070,1070,1095
 1070 IF (OTEMP-OTDFP) 1075,1075,1080
 1075 IF (OX(II,JJ)-1.0) 1080,1085,1085
 1080 OQ=3.0*(OPV-OPG)*OALPHA*ODELTN/(ORHOL*OGAM)*DD3*DSQRT(1.0/OTEMP)
 1085 IF (OPG) 1095,1095,1090
 1090 OSQRT=DSQRT(DD9*OGAM*OPG/OTG)
      OZ=DD12*OGAM**2*OQ/(2.0+3.6*DD1*OSQRT)
      IF (OZ-30.0) 1205,1205,1200
 1200 OZ=30.0
 1205 OOMEGA=OOPG*(OTG-OTEMP)/(DEXP(OZ)-1.0)
      OSIGMA=OOMEGA*DD5*C(II)*OQ
      OQN=OQN+OSIGMA
 1085 OR(II,JJ+1)=OGAM*(1.0-OQ)**(1.0/3.0)
      OTD(II,JJ+1)=OTEMP-OLMBDE/OCPL*OQ
      IF (OX(II,JJ)) 1210,1210,1207
 1207 OTD(II,JJ+1)=OTDFP
      IF (0.60-OX(II,JJ)) 1225,1225,1400
 1210 IF (OQ) 1215,1225,1215
 1215 IF (OPG) 1225,1225,1220
 1220 OTD(II,JJ+1)=OTEMP+OQ/OCPL*(OOMEGA-OLMBDE)
 1400 IF (JJ-DD13) 1225,1401,1401
 1401 IF (OX(II,JJ)) 1405,1405,1236
 1405 IF (NN-(DD13+OTDHT/ODELTN)) 1410,1415,1415
 1410 OFRCT=(OFRCTH-OFRCTL)*(1-(NN-DD13)**ODELTN/OTDHT)+OFRCTL
      GO TO 1420
 1415 OFRCT=OFRCTL
 1420 OTD(II,JJ+1)=OTD(II,JJ+1)+OFRCT*(OTDO-OTD(II,JJ+1))
 1225 OCHI=0.0
      IF (OTD(II,JJ+1)-OTDFP) 1230,1230,1235
 1230 OCHI=OQ/OLMBDE*(OLMBDS-OOMEGA)
 1235 OX(II,JJ+1)=OX(II,JJ)+OCHI
      IF (OX(II,JJ+1)) 1236,1237,1237
 1236 OX(II,JJ+1)=0.0
 1237 IF (OX(II,JJ+1)-1.0) 1239,1239,1238
 1238 OX(II,JJ+1)=1.0
 1239 OF=C(II)*DD5*OQ
      OGN=OGN+OF
      OHN=OHN+OF*OTEMP
      IF (II-3) 1004,1240,1240
 1240 IF (JJ-1) 1245,1245,1003
 1245 OMC=DD8*OPG/OTG-OTHETA*MINT
      OGW=0.0
      IF (OPG-OPVW) 1252,1252,1250
 1250 OGW=DD4*(OPG-OPVW)/DSQRT(OTG)
 1252 OMNOZ=DD7*OPG/DSQRT(OTG)
      OTGPRM=(OHN+OTG*(OMC-OGW-OMNOZ)+(OQR-OQN)/OCPG)/(OGN+OMC-OGW-
     1 OMNOZ)
      OPGPRM=OTGPRM*((OGN-OGW-OMNOZ)/DD8+OPG/OTG)
```

```
      TIME=TIME+ODELTN
      TIMEMS=1000.0*TIME
      PGMMHG=0.359131*OPGPRM
      WRITE(6,102) NN,TIMEMS,PGMMHG,OTGPRM,OMNOZ,OMC,OGN
      NN=NN+1
      OPG=OPGPRM
      OTG=OTGPRM
      IF (NN-1-2*N) 1002,3000,1002
 3000 PGMMHG=0.359131*PGPRM
      TGAV=(OMC*OCPG*OTG+MC*CPG*TGPRM)/(OMC*OCPG+MC*CPG)
      MINT=0.03206*OMC*MC*AEINT*DELTN*EXP(-1.8*EAINT/RCAL/TGAV)/(OM*
     1 THETA*VC)
      TMINT=TMINT+MINT
      OR=-MINT*DELHR
      OOR=OMC/(OMC+MC)*OR
      FOR=MC/(OMC+MC)*OR
      TIGN=19.24*RCAL*01*TGAV**3/((OPG+PGPRM)*AOIGN*EAIGN)*(1.0+PGPRM/
     1 OPG)*(M*CPG+OM/2*OCPG/10*(OPG/PGPRM)*EXP(1.8*EAIGN/RCAL/TGAV)*
     2 1000.0
      FRCTIG=1000*DELTN/TIGN
      SMIGFR=SMIGFR+FRCTIG
      WRITE(6,102) N,TIMEMS,PGMMHG,TGPRM,MNOZ,MC,GN,TMINT,TIGN,TGAV,
     1 SMIGFR
      IF (SMIGFR-1.0) 264,280,280
  264 N=N+1
  265 IF (N-101) 270,280,280
  270 PG=PGPRM
      TG=TGPRM
      GO TO 2
  280 WRITE(6,104) TIMEMS
      GO TO 1
      END
```

APPENDIX B. COMPUTER PROGRAM INPUT DATA FOR CALCULATION OF IGNITION DELAY IN ENGINE CONFIGURATION NO. 1 (Calc. N_2O_4/MMH #5809-1-17)

Initial Conditions - Fuel

Δt_N	=	5×10^{-5} sec	
T_o	=	538 °R	
r (1, 1)	=	5.83×10^{-5} ft	Calculated from mass median drop size of 50 microns as discussed in Sec. III. A.
r (2, 1)	=	1.71×10^{-4} ft	
r (3, 1)	=	3.84×10^{-4} ft	
T_d (1, 1) - T_d (2, 1) - T_d (3, 1)	=	538 °R	

Chamber Data - Fuel

$\dot{w}$	=	0.075 lb_m/sec	P_{vw}	=	143 PSF
V_c	=	8.16×10^{-4} cu. ft.	t_{ss}	=	8.0×10^{-4} sec
A*	=	9.51×10^{-4} sq. ft.	f_{max}	=	0.15
A_c	=	4.60×10^{-2} sq. ft.	f_{min}	=	0.02
V_d	=	71.5 ft./sec	D_{iw}	=	0.0852 ft.
L_c	=	0.167 ft	t_{dh}	=	2.5×10^{-3} sec

APPENDIX B - cont'd

Propellant Data - Fuel

M =	46 lb_m/lb-mole	c_{pl} =	0.694 Btu/lb_m-^oR
α =	0.5	c_{pg} =	0.34 Btu/lb_m-^oR
ρ_l =	55.65 lb_m/cu. ft.	T_{dFP} =	397.7 ^oR
λ_e =	389 Btu/lb_m	k =	1.13
λ_s =	486 Btu/lb_m	μ_g =	4.91 x 10^{-6} lb_m/ft-sec
λ_F =	97.5 Btu/lb_m	K_g =	1.9 x 10^{-6} Btu/sec-ft^2-(^oR/ft)

Initial Conditions - Ox

ΔtN	=	2.5 x 10^{-5} sec	
T_c	=	537 ^oR	
$r(1,1)$	=	5.83 x 10^{-5} ft	Calculated from mass-median drop size of 50 microns as discussed in Sec. III. A.
$r(2,1)$	=	1 . . x 10^{-4} ft	
$r(3,1)$	=	3.84 x 10^{-4} ft	
$T_d(1,1) = T_d(2,1) = T_d(3,1)$	=	537 ^oR	

Chamber Data - Ox

$\dot{w}$ =	0.120 lb_m/sec	P_{vw} =	2558 PSF
V_c =	8.16 x 10^{-4} cu. ft.	t_{ss} =	1.6 x 10^{-3} sec
A^* =	9.51 x 10^{-4} sq. ft.	f_{max} =	0.15
A_c =	4.60 x 10^{-2} sq. ft.	f_{min} =	0.02
V_d =	69.0 ft/sec	D_{iw} =	0.0852 ft
L_c =	0.167 ft	t_{dh} =	2.5 x 10^{-3} sec

APPENDIX B - cont'd

Propellant Data - Ox

M	=	92 lb_m/lb-mole	c_{pl}	=	0.36 Btu/lb_m-^oR
α	=	0.1	c_{pg}	=	2.0 Btu/lb_m-^oR
ρ_l	=	92.5 lb_m/cu.ft	T_{dFP}	=	471.8 ^oR
λ_e	=	173 Btu/lb_m	k	=	1.08
λ_s	=	237 Btu/lb_m	μ_g	=	7.9 x 10^{-6} lb_m/ft-sec
λ_F	=	68.5 Btu/lb_m	K_g	=	2.4 x 10^{-5} Btu/sec-ft^2-(^oR/ft)

Reaction Intermediate Data

θ_f	=	0.571
θ_{ox}	=	0.429
ΔH_r	=	-1619 Btu/lb_m
A_{int}	=	1.7 x 10^{11} cc/mole-sec
E_{int}	=	4500 cal/g-mole

Ignition Data

$(A\Omega)_{ign}$	=	3.4 x 10^{14} cal-cc/$mole^2$-sec
E_{ign}	=	5200 cal/g-mole
R_{cal}	=	1.987 cal/mole-^oK

APPENDIX C. PRINTOUT OF COMPUTED RESULTS FOR ENGINE CONFIGURATION NO. 1

The first column of the printout which follows gives the number N of time intervals through which the solution has proceeded. At any given time into the calculation, second column, the N for the oxidizer is twice the N for the fuel since the time interval step used for the oxidizer is one-half that of the fuel. The times given in the second column do not include the time from valve signal to initial emergence of propellant from the injector into the thrust chamber. This time was determined from schlieren movies and oscillogram traces to be 3.5 msec for the feed system/propellant valve/1-on-1 doublet injector assembly used in the program. Thus, 3.5 msec must be added to the times given in the second column of the printout to give the total time from valve signal.

The third column of the printout gives the partial pressure of the appropriate reactant and the fourth column gives analogously the temperature of the reactant vapor in the chamber. The fifth, sixth and seventh columns give respectively: the mass efflux of vapor phase reactant through the nozzle during the time interval in question, the mass of reactant vapor present in the chamber at the end of the time interval, and the net mass vaporized during the time interval.

The calculated results are given in the printout in groups consisting of three rows. The first two rows in each three-row group pertain to the oxidizer for which smaller time intervals are required as a consequence of its high volatility. The third row of each three-row group pertains to the fuel, MMH. This row also gives: (a) the total mass of reaction intermediate TMINT formed from the start of the calculation to the time interval N in question, (b) the ignition delay time TIGN calculated for the pressure, temperature and vapor composition prevailing at the end of the time interval in question, (c) the average gas temperature TGAV for the fuel and oxidizer vapors in the chamber at the end of the time interval in question, and (d) the sum of ignition fractions SMIGFR from the first time interval of the calculation to the time interval in question.

Additional calculated quantities which have been printed out in other computer runs (and which made the printout voluminous) include: the radius, temperature and frozen fraction of each drop class (3) in each ensemble (1, 2. . . . . N) in each, or every tenth, time interval.

APPENDIX C - cont'd.

The computer printout for the ignition delay calculations for Engine Configuration No. 1 is reproduced on the following pages.

APPENDIX C - cont'd.

N	TIME,MS	PG,MMHG	TG,DEG.R	MNOZ,LB	MC,LB	GN,LB	TMINT,LB	TIGN,MS	TGAV,R	SMISFR
1	0.025	0.004	537.000	0.0	0.0	2.582350-10				
[illegible]	0.050	0.017	534.274	9.393050-12	9.582350-10	3.356250-09				
1	0.050	0.025	538.000	0.0	0.0	3.111260-09	0.0	15947.91	534.27	0.0000
3	0.075	0.043	531.576	4.209330-11	4.305100-09	6.593860-09				
[illegible]	0.100	0.083	529.235	1.058850-10	1.085690-08	1.047750-08				
2	0.100	0.111	535.754	8.778580-11	3.[illegible]126D-09	1.098240-08	9.73447E-14	3528.48	529.54	0.0000
5	0.125	0.140	527.[illegible]91	2.065810-10	2.122850-08	1.491030-08				
6	0.150	0.215	525.369	3.489920-10	3.593220-08	1.984620-08				
3	0.150	0.279	533.515	9.943560-10	1.400580-0[illegible]	2.170330-08	1.47195E-12	1432.44	525.88	0.0001
7	0.175	0.310	523.730	5.374280-10	5.542480-08	2.525090-08				
8	0.200	0.427	522.227	7.758300-10	8.014230-08	3.109670-08				
4	0.200	0.541	531.572	9.922630-10	3.531400-[illegible]	3.[illegible]99[illegible]0-08	8.86625E-12	752.90	522.88	0.0001
9	0.225	0.565	520.861	1.067820-08	1.104610-07	3.736160-08				
10	0.250	0.729	519.583	1.418800-09	1.467550-07	4.402550-08				
5	0.250	0.908	529.933	1.931070-09	6.884820-08	4.890470-0[illegible]	3.42823E-11	456.97	520.35	0.0002
11	0.275	0.915	518.427	1.825010-09	1.893570-07	5.107190-08				
12	0.300	1.128	517.326	2.298130-09	2.386020-07	5.[illegible]48590-08				
6	0.300	1.383	528.599	3.243640-09	1.[illegible]30170-07	6.436740-08	1.01559E-10	304.05	518.18	0.0004
13	0.325	1.368	516.242	2.836330-09	2.947710-07	6.625[illegible]70-0[illegible]				
14	0.350	1.636	515.389	3.443230-09	3.581900-07	7.437400-08				
7	0.350	1.969	527.595	4.948500-09	1.766960-07	8.[illegible]95780-0[illegible]	2.[illegible]931E-10	215.59	516.33	0.0006
15	0.375	1.933	514.558	4.121210-09	4.290860-07	8.283480-08				
16	0.400	2.259	513.736	4.873180-09	5.078000-07	9.163200-08				
8	0.400	2.664	526.921	7.050770-09	2.522580-07	9.645127-08	5.47498[illegible]-10	160.14	514.76	0.0009
17	0.425	2.617	513.044	5.701100-09	5.944960-07	1.[illegible]07590-07				
18	0.450	3.006	512.342	6.608040-09	6.895540-07	1.107[illegible]90-07				
9	0.450	3.461	526.643	9.542700-09	3.415750-07	1.121360-07	[illegible].000[illegible]c-09	123.24	513.45	0.0013
19	0.475	3.428	511.782	7.595480-09	7.930540-07	1.199760-07				
20	0.500	3.883	511.194	8.666760-09	9.054340-07	1.300510-0[illegible]				
10	0.500	4.355	526.799	1.240420-08	4.440330-07	1.269300-07	1.97636E-09	97.50	512.39	0.0019
21	0.525	4.373	510.763	9.822700-09	1.026660-06	1.404270-07				
22	0.550	4.897	510.288	1.106710-08	1.157270-06	1.510940-07				
11	0.550	5.333	527.415	1.560350-08	5.583510-07	1.403860-07	3.39770E-09	78.87	511.59	0.0025
23	0.575	5.459	509.985	1.240000-08	1.297070-06	1.620450-07				
24	0.600	6.056	509.624	1.382580-08	1.446710-06	1.731600-07				
12	0.600	6.385	528.555	1.909870-08	6.828340-07	1.521160-07	5.55191E-09	64.96	511.03	0.0033
25	0.625	6.690	509.458	1.534250-08	1.605730-06	1.843210-07				
26	0.650	7.360	509.226	1.695340-08	1.774710-06	1.955200-07				
13	0.650	7.495	530.258	2.283940-08	8.154320-07	1.618160-07	8.69387E-09	54.31	510.75	0.0042
27	0.675	8.068	509.208	1.865400-08	1.952860-06	2.067500-07				
28	0.700	8.810	509.112	2.044920-08	2.140950-06	2.179990-07				
14	0.700	8.651	532.569	2.678920-08	9.538440-07	1.692940-07	1.31288E-08	45.98	510.76	0.0053
29	0.725	9.592	509.248	2.233270-08	2.337950-06	2.292650-07				
30	0.750	10.407	509.291	2.431110-08	2.544880-06	2.405330-07				
15	0.750	9.837	530.528	3.082850-08	1.095630-06	1.744880-07	1.92136E-08	39.33	511.08	0.0065

APPENDIX C - cont'd.

31	0.775	11.263	509.584	2.633620-08	2.760400-06	2.518020-07	2.73619E-08	33.95	511.71	0.0080		
32	0.800	12.151	509.769	2.453630-08	2.985820-06	2.630580-07						
33	0.825	13.091	510.219	3.078140-08	3.219440-06	2.742990-07						
34	0.850	14.042	510.549	3.312180-08	3.462980-06	2.855580-07	3.80453E-08	29.54	512.64	0.0097		
35	0.875	15.054	511.136	3.554470-08	3.714280-06	2.990370-07						
36	0.900	16.098	511.589	3.808510-08	3.977770-06	3.107360-07						
37	0.925	17.186	512.341	4.072860-08	4.248710-06	3.221550-07						
38	0.950	18.304	512.946	4.342600-08	4.529590-06	3.327560-07	5.17750E-08	25.89	513.85	0.0116		
39	0.975	19.465	554.741	4.622360-08	4.817380-06	3.430670-07						
40	1.000	20.652	513.867	4.911910-08	5.115320-06	3.548760-07						
41	1.025	21.900	514.624	5.212180-08	5.432960-06	3.766040-07	6.91005E-08	22.84	515.37	0.0138		
42	1.050	21.168	516.632	5.519820-08	5.732700-06	3.766040-07						
43	1.075	24.476	517.805	5.829780-08	6.052080-06	3.900180-07						
44	1.100	25.851	518.915	6.156820-08	6.384600-06	4.014900-07	9.06073E-08	20.25	517.21	0.0163		
45	1.125	27.257	520.327	6.490610-08	6.722150-06	4.120410-07						
46	1.150	28.584	521.545	6.833390-08	7.069280-06	4.224030-07						
47	1.175	30.170	523.147	7.184420-08	7.420610-06	4.326270-07						
48	1.200	31.681	524.513	7.544500-08	7.781390-06	4.466535-07	1.16094E-07	18.02	519.38	0.0191		
49	1.225	33.263	524.283	7.913960-08	8.149690-06	4.565680-07						
50	1.250	34.860	527.838	8.293590-08	8.526040-06	4.662620-07						
51	1.275	36.515	529.827	8.678370-08	8.906490-06	4.757620-07						
52	1.300	38.183	531.589	9.073440-08	9.295460-06	4.849660-07	1.66965E-07	16.10	521.81	0.0222		
53	1.325	39.938	533.784	9.479010-08	9.689780-06	4.983980-07						
54	1.350	41.702	535.739	9.887050-08	1.008950-05	5.071730-07						
55	1.375	43.536	538.197	1.030490-07	1.049380-05	5.157720-07						
56	1.400	45.395	540.168	1.073350-07	1.090780-05	5.238110-07	1.48824E-07	14.42	524.58	0.0256		
57	1.425	47.332	542.389	1.118940-07	1.133780-05	5.336220-07						
58	1.450	49.274	544.941	1.167480-07	1.178440-05	5.440490-07						
59	1.475	51.329	548.567	1.220670-07	1.226440-05	5.576950-07						
60	1.500	53.374	551.505	1.275230-07	1.280640-05	5.693210-07	1.87065E-07	14.42	524.58	0.0256		
61	1.525	55.538	554.487	1.330160-07	1.337890-05	5.777640-07						
62	1.550	57.703	557.781	1.386750-07	1.396780-05	5.851330-07						
63	1.575	59.982	561.665	1.397440-07	1.397440-05	5.924770-07	2.32572E-07	12.94	527.68	0.0295		
64	1.600	62.270	565.077	1.457850-07	1.457850-05	6.006030-07						
65	1.625	64.649	568.958	1.519660-07	1.519660-05	6.071410-07						
							2.86428E-07	11.43	531.12	0.0338		
							3.49868E-07	10.45	534.98	0.0386		
							4.24329E-07	9.59	539.22	0.0439		
							5.11554E-07	8.83	543.94	0.0498		
							6.13714E-07	7.55	549.19	0.0565		
							7.33384E-07	6.75	555.89	0.0639		
							8.73825E-07	6.01	561.54	0.0722		
							1.03917E-06	5.35	568.93	0.0816		

APPENDIX C - cont'd.

REFERENCES

(1) Corbett, A. D., Dawson, B. E., Seamans, T. F. and Vanpee, M., Hypergolic Ignition at Reduced Pressures (U), AFRPL-TR-65-257, Air Force Systems Command, Edwards, California, February 1966 (AD 369585).

(2) Corbett, A. D., Dawson, B. E. and Seamans, T. F., Hypergolic Ignition at Reduced Pressures (U), AFRPL-TR-65-105, Air Force Systems Command, Edwards, California, July 1965 (AD 364162).

(3) Lawver, B. R., Rocket Engine Fuel Additive Evaluation Program, PR 3006-F, Contract NAS9-4299, Marquardt Corp., December 1965.

(4) Priem, R. J. and Heidman, M. F., Propellant Vaporization as a Design Criterion for Rocket Engine Combustion Chambers, NASA TR R-67, National Aeronautics and Space Administration, 1960.

(5) Agosta, V. D. and Kraus, G., An Investigation of the Impulse Bit Developed by a Pulsed Liquid Propellant Rocket Engine, Chemical Engineering Progress Symposium Series No. 52, Vol. 60, 1964.

(6) For example: Walker, W. H., et al, Principles of Chemical Engineering, 3rd Ed., Chapter IV, McGraw-Hill, 1937.

(7) Weiss, H. G., A Basic Study of the Nitrogen Tetroxide-Hydrazine Reaction, Report SN-4500, JPL Contract No. BE 4-229751, July 1965.

(8) Christos, T., Miron, Y., James, H. and Perlee, H. E., Exploratory Study of Hypergolic Ignition Spike Phenomena, First Quarter Report No. 3986, Bureau of Mines, Period: January 1 to March 31, 1966.

(9) C-1 Engine Development Program, Contract NAS8-15486.

REFERENCES - Cont'd

(10) Properties of Explosives of Military Interest, Section 1, ORDP 20-177, Ordnance Engineering Design Handbook, Explosives Series, Ordnance Corps U.S.A., May 1960.

(11) Nitrogen Tetroxide Product Bulletin, Allied Chemical Corporation, Nitrogen Division, Table 20, p. 41 (no date).

(12) Jost, W., Explosion and Combustion Processes in Gases, Chapter I, McGraw-Hill, 1946.

(13) Breen, B. P. and Lawver, B. R., Effects of Additives on the Combustion of Hydrazine, Progress Report No. AFRPL-TR-66-254, Air Force Systems Command, Edwards, California, September 1966.